

Neutral beam driven hydrogen spectroscopy in fusion plasmas

Citation for published version (APA):

Delabie, E. G. (2011). *Neutral beam driven hydrogen spectroscopy in fusion plasmas*. [Phd Thesis 1 (Research TU/e / Graduation TU/e), Applied Physics and Science Education]. Technische Universiteit Eindhoven. <https://doi.org/10.6100/IR711240>

DOI:

[10.6100/IR711240](https://doi.org/10.6100/IR711240)

Document status and date:

Published: 01/01/2011

Document Version:

Publisher's PDF, also known as Version of Record (includes final page, issue and volume numbers)

Please check the document version of this publication:

- A submitted manuscript is the version of the article upon submission and before peer-review. There can be important differences between the submitted version and the official published version of record. People interested in the research are advised to contact the author for the final version of the publication, or visit the DOI to the publisher's website.
- The final author version and the galley proof are versions of the publication after peer review.
- The final published version features the final layout of the paper including the volume, issue and page numbers.

[Link to publication](#)

General rights

Copyright and moral rights for the publications made accessible in the public portal are retained by the authors and/or other copyright owners and it is a condition of accessing publications that users recognise and abide by the legal requirements associated with these rights.

- Users may download and print one copy of any publication from the public portal for the purpose of private study or research.
- You may not further distribute the material or use it for any profit-making activity or commercial gain
- You may freely distribute the URL identifying the publication in the public portal.

If the publication is distributed under the terms of Article 25fa of the Dutch Copyright Act, indicated by the "Taverne" license above, please follow below link for the End User Agreement:

www.tue.nl/taverne

Take down policy

If you believe that this document breaches copyright please contact us at:

openaccess@tue.nl

providing details and we will investigate your claim.

Neutral beam driven hydrogen spectroscopy in fusion plasmas

PROEFSCHRIFT

ter verkrijging van de graad van doctor aan de Technische Universiteit Eindhoven, op gezag van de rector magnificus, prof.dr.ir. C.J. van Duijn, voor een commissie aangewezen door het College voor Promoties in het openbaar te verdedigen op maandag 23 mei 2011 om 16.00 uur

door

Ephrem Geert Delabie

geboren te Kortrijk, België

Dit proefschrift is goedgekeurd door de promotoren:

prof.dr. N.J. Lopes Cardozo
prof.dr.ir. G. Van Oost

Copromotor:
dr. R.J.E. Jaspers



This work is part of the research programme of the Foundation for Fundamental Research on Matter (FOM), which is part of the Netherlands Organisation for Scientific Research (NWO).

© Copyright 2011, Ephrem Delabie

All rights reserved. No part of this publication may be reproduced, stored in a retrieval system, or transmitted, in any form or by any means, electronic, mechanical, photocopying, recording or otherwise, without the prior written permission from the copyright owner.

A catalogue record is available from the Eindhoven University of Technology Library

Delabie, Ephrem

Neutral beam driven hydrogen spectroscopy in fusion plasmas

ISBN: 978-90-386-2480-8

Printed by: Universiteitsdrukkerij Technische Universiteit Eindhoven

Cover: Work in progress

Contents

1	Introduction	1
1.1	Energy demand and supply	1
1.2	Nuclear fusion	2
1.3	Active beam spectroscopy for the diagnosis of hot plasmas	3
1.4	This thesis	5
1.5	List of publications	6
2	Active beam spectroscopy	9
2.1	Introduction	10
2.2	Charge exchange spectroscopy	10
2.2.1	Overview	10
2.2.2	Isolating the active charge exchange component	11
2.2.3	The physics of charge exchange spectroscopy	12
2.2.4	Atomic physics effects on the charge exchange line shape	20
2.2.5	Fast ion charge exchange spectroscopy	29
2.3	Neutral beam attenuation	30
2.4	Beam emission and motional Stark effect spectroscopy	31
2.4.1	Overview	31
2.4.2	Fitting of the beam emission spectrum	32
2.4.3	Beam emission as a neutral beam diagnostic	35
2.4.4	The Motional Stark effect diagnostic	38
2.5	Active hydrogen beam spectroscopy on TEXTOR	42
2.5.1	Introduction	42
2.5.2	CXS periscopes and lines of sight	42
2.5.3	Spectrometers and ccd cameras	44
2.5.4	Calibration	45
2.5.5	Data acquisition and analysis	46
2.6	Outlook	46
3	Atomic data for the interpretation of beam emission	49
3.1	Abstract	49
3.2	Motivation	50
3.3	Atomic models of the neutral beam	51
3.3.1	Collisional-radiative models for the neutral beam (n-resolved)	51
3.3.2	Consistency of atomic data for NB emission	52
3.3.3	Consistency of atomic data for NB stopping	53
3.3.4	Collisional-radiative models for the neutral beam (nkm-resolved)	54
3.4	Measured vs. predicted beam emission intensity	56
3.4.1	Consistency of D_α and D_β beam emission intensities	56
3.4.2	Neutral beam power fractions from beam emission	60

3.5	Relative intensities within the MSE multiplet	62
3.6	Conclusions	64
3.7	Acknowledgement	66
4	Fast ion charge exchange	67
4.1	Principles and background of the technique	67
4.2	Test of fast ion charge exchange spectroscopy on TEXTOR	68
4.2.1	Instrumentation	68
4.2.2	Sample Data	70
4.2.3	Modelling and Interpretation	72
4.2.4	Passive charge exchange emission	74
4.3	Test of fast ion charge exchange spectroscopy on JET	75
4.4	Discussion and conclusion	78
5	Applications of beam emission and fast ion charge exchange spectroscopy	81
5.1	Introduction	81
5.2	Measuring the helium density with active beam spectroscopy	81
5.2.1	Motivation	81
5.2.2	Helium concentration measurements from combined beam emission and charge exchange spectroscopy	82
5.3	Fast ion density profiles from charge exchange spectroscopy	83
6	Prospects of thermal and fast helium CXS on ITER	89
6.1	Introduction	89
6.2	Thermal He CXS/BES concentration measurements on ITER	90
6.3	Fast helium CXS measurements on ITER	95
7	Conclusions and outlook	101
	Bibliography	105
	Summary	113
	Curriculum Vitae	115
	Acknowledgements	116

Introduction

Contents

1.1	Energy demand and supply	1
1.2	Nuclear fusion	2
1.3	Active beam spectroscopy for the diagnosis of hot plasmas	3
1.4	This thesis	5
1.5	List of publications	6

1.1 Energy demand and supply

The supply of fossil fuels is limited. Nevertheless, our society is based on an undisturbed availability of power. The world population currently consumes approximately 15TW of primary power, of which about 13TW comes from fossil fuels. The share of various sources of energy in the consumption pattern since 1965 is shown in fig. 1.1 [1, 2, 3]. Also shown on the right hand side of fig. 1.1 is how long the proven recoverable supply of each of the primary energy sources would suffice to meet the current demand. Discoveries of new reserves or advances in technology to extract difficultly accessible resources is a matter of debate, and will likely extend the given lifetimes for each of the fuels, especially uranium. It is clear however, aside from environmental constraints, that fossil fuels will not be able to cope with the prospected energy demand for the full length of the 21st century. Hydro-electric and other renewable sources suffer from either special geographic needs or low energy density, even in case of considerable technological progress. A shortage of oil and gas also implies a further shift to an electrical energy based society. Nuclear fission could help considerable in providing a stable electric grid, but shortage of fissile fuels is also to be foreseen in the medium long run unless more efficient use is made of energetic neutrons in nuclear reactors.

The fusion of light nuclei combines the advantage of a very high energy density with abundant availability of fuel, if technological barriers can be overcome to construct a fusion driven power plant.

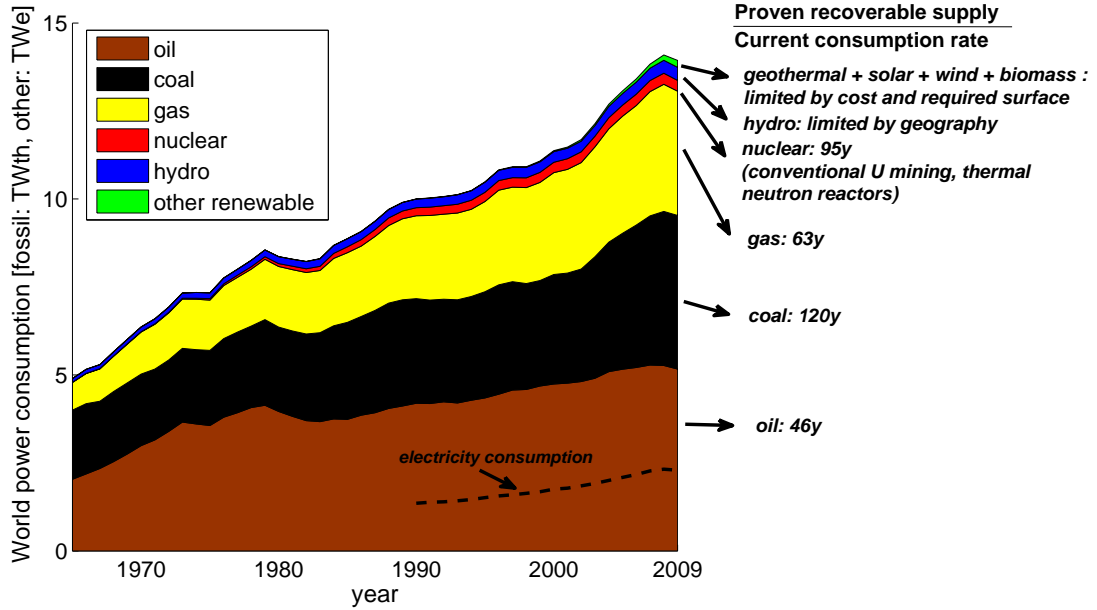
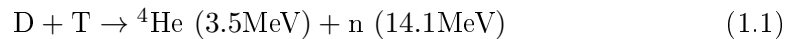


Figure 1.1: Yearly averaged world power consumption since 1965 (derived from [1, 2, 3]). The fossil fuel consumption is expressed in thermal units, while for nuclear, hydroelectric and other renewables the electric output power is shown. The dashed line shows the amount of electric power consumed.

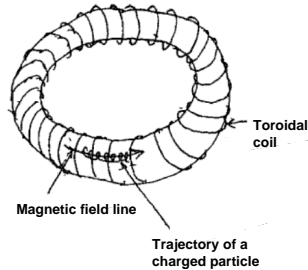
1.2 Nuclear fusion

The easiest fusion reaction, requiring the lowest collision energy between the reactants, is the one depicted in eq. 1.1 between deuterium and tritium, producing helium, a neutron and 17.6 MeV of energy.

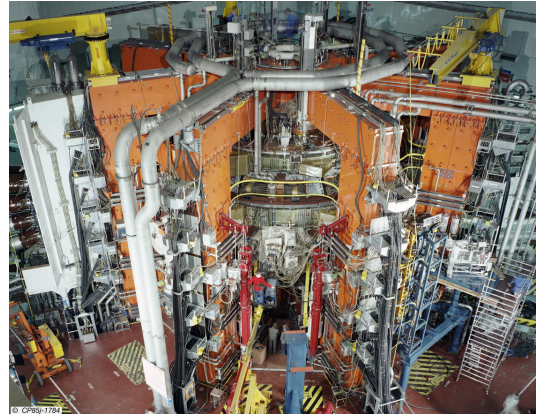


The D-T fusion reaction has its maximum likelihood at a collision energy of about 50keV. However, even at this energy, colliding particles still have a 10000 times large chance to deflect by their electric fields than to fuse. Therefore the particles need to be confined such that they experience many collisions before losing their energy. Several methods of confinement are possible: gravitational (like the sun), inertial (heating faster than fuel expansion), or using magnetic fields to lock up the ionized fuel in a closed configuration. The latter technology has the best prospects for construction of a viable power plant. The best magnetic confinement to date is achieved in a tokamak.

A tokamak is a device that generates a toroidal helical magnetic field by combining a toroidal field from coils wound around a torus and a poloidal field generated by a current flowing toroidally through an ionized gas, called a plasma. This plasma current is induced by ramping up a current through a solenoid placed in the center



(a) Early drawing of the principle of magnetic confinement in a tokamak by A. Sakharov [4]. Charged particles gyrate around the magnetic field lines to which they are bound. Not drawn is the central solenoid that generates the plasma current.



(b) The Joint European Torus (JET), the tokamak with largest plasma volume, holding the record of fusion generated power.

Figure 1.2: Drawing of the tokamak concept at the left hand side and a picture of a tokamak at the right hand side.

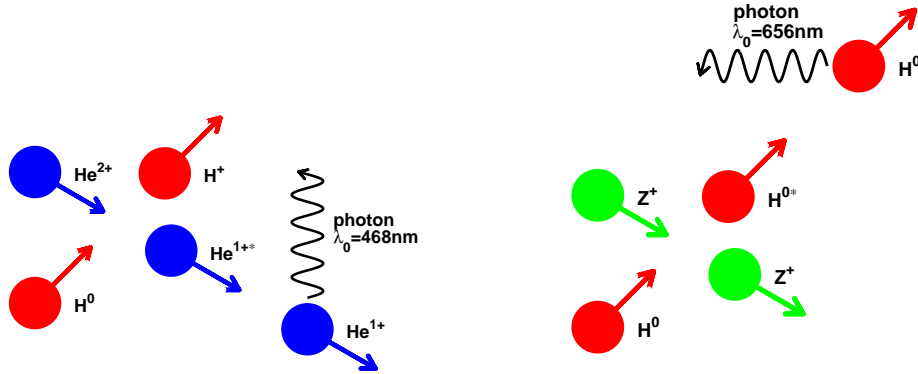
of the torus, this solenoid acts as the first winding of a transformer and the highly conductive plasma acts as the second winding. An early sketch of the tokamak concept and a picture of the JET tokamak are shown in fig. 1.2.

The record of fusion-generated power in a tokamak is 16.1MW [5], the highest ion temperature reached is 44keV [6], electron densities over 10^{20} m^{-3} and energy confinement times of more than a second are achieved in tokamaks. This has all been measured by dedicated diagnostics.

In pace with progress in tokamak operation, diagnostics have been developed to improve our understanding of plasma behavior and to control plasma discharges. The knowledge gained from diagnostics is also the motor for improved tokamak design. ITER, the next step tokamak device, is currently being built to demonstrate a steady fusion power output of 500MWth and to study plasmas heated by the fusion produced helium.

1.3 Active beam spectroscopy for the diagnosis of hot plasmas

As tokamak plasmas move towards fusion relevant conditions, diagnosing the ions in the plasma becomes increasingly important as it are the temperature and species mix of the ions that determine the generated fusion power. The ions however are more difficult to diagnose directly and with the same accuracy as the electrons. One is usually limited to spectroscopy or indirect evidence from neutrons.



(a) The principle of charge exchange spectroscopy. (b) The principle of beam emission spectroscopy.

Figure 1.3: Simplified sketches of some of the reactions on which charge exchange and beam emission spectroscopy are based.

Modern optical spectroscopy (marked by the invention of the diffraction grating in 1814) is a wide-ranging field of research. When it comes to spectroscopy of fusion plasmas a first distinction can be made between passive and active spectroscopy. Passive line spectroscopy is based on measuring the emission lines from atoms or ions that are excited by collisions. This technique is limited by the fact that in hot plasmas the light elements are all fully ionized. In order to obtain measurements of fully stripped ions, beams of atomic deuterium or hydrogen are injected in the plasma. The atoms serve as electron donors and populate excited states of the plasma ions of interest. This technique is known as charge exchange spectroscopy (CXS) and the principle is sketched in fig. 1.3(a). In contrast to passive spectroscopy, CXS has the additional benefit that the measurements are localized to the intersection volume between the neutral beam and the lines of sight. The measured charge exchange intensities can be used quantitatively if the beam densities along a line of sight are accurately determined. A spectroscopic technique to deal with this is to measure the light emitted by excited neutrals in the beam itself. This is called beam emission spectroscopy (BES) and it is schematically shown in fig. 1.3(b). Additionally, from the Doppler shifted and broadened charge exchange line, the plasma rotation velocity and the ion temperature can be determined and from the motional Stark splitting of the beam emission lines information about the plasma current profile can be obtained. Active beam spectroscopy will be essential for 8 of the 45 quantities that need to be measured on ITER [7] and will provide additional information on several other parameters.

The most important parameter to be measured with charge exchange spec-

troscopy on ITER is the thermalized helium concentration profile (10% accuracy required [7]). ITER will be the first tokamak where the plasma heating will be dominated by the fusion produced helium. When the helium ions have transferred their energy to the bulk plasma, they need to be removed from the fuel to prevent fuel dilution, otherwise the burning plasma will be suffocated by its ash. Measuring the helium concentration is needed both for understanding the α -particle heating and control of the fusion performance.

1.4 This thesis

Above, the importance of measuring the helium concentration on ITER is motivated and the diagnostic technique to do this is outlined. A detailed assessment of the physics of hydrogen beam spectroscopy is given in chapter 2, with a description of the implementation on TEXTOR which has been used in chapter 4 and 5.

Despite charge exchange spectroscopy being a well-established technique on many tokamaks, it remains difficult to obtain the absolute impurity concentration profiles directly from the observed photon fluxes. The four main reasons for this are: (1) the effective emission rates need to be reliably known; (2) the spectrum should be absolutely calibrated; (3) the attenuation of the neutral beam in the plasma must be calculated; (4) the beam and line of sight intersection path as well as the beam geometry must be accurately characterized.

Items (2) and (3) would make CXS impossible on ITER because of the impossibility to access the vessel for regular calibrations and the high attenuation of the neutral beam. To illustrate this, on the magnetic axis of ITER, merely 3% of the beam power is left. Errors on the calculated attenuation accumulate along the beam path, giving rise to anticipated errors of more than 50% on the ITER magnetic axis. Although 3% of the beam power cannot be calculated reliably anymore, it can still be measured using beam emission. When combining BES and CXS, issues (2,3,4) become trivial, however one will strongly rely on the charge exchange and beam emission rates (issue (1)) to convert the measured beam emission intensities in beam densities. Hence, the challenge of measuring the helium concentration profile with charge exchange spectroscopy on ITER, can be rephrased to:

Is beam emission a validated technique to measure the beam density?

A detailed answer to this question is formulated in chapter 3, based on an assessment of the involved atomic modelling and a comparison with beam emission data from JET.

Apart from measuring the thermalized helium population, charge exchange spectroscopy also has the potential to contribute to a better understanding of the confinement and transport of supra-thermal ions by measuring fast ion radial profiles.

Fast ion measurements with CXS have mainly been relative (changes in time) or were focused on the velocity distribution function. For obtaining information on the radial transport of the fast ions, the fast ion profiles are of capital importance. Therefore the following question was addressed:

Can charge exchange spectroscopy be used to measure fast (beam) ion profiles?

This question is addressed in chapter 4 and applied to deuterium beam ions on TEXTOR and JET.

In chapter 5 the techniques of chapters 3 and 4 are combined and applied to obtain thermal helium and fast ion density profiles on TEXTOR from a combination of charge exchange and beam emission. The helium concentration profile is compared to the expected values during a gas puff and the fast ion profiles are compared to modelled values.

Finally, in chapter 6, the expected fast and thermal helium CXS and BES spectra on ITER are simulated and the expected accuracy that could be obtained on the thermal and fast helium concentration profiles is discussed.

1.5 List of publications

During the preparation of this thesis, the author has contributed to the following peer-reviewed journal publications.

E. Delabie, M. Brix, R. J. E. Jaspers, C. Giroud, O. Marchuk, M. G. O'Mullane, Yu. Ralchenko, E. Surrey, M. G. von Hellermann, K. D. Zastrow, and JET-EFDA Contributors

Consistency of atomic data for the interpretation of beam emission spectra.

Plasma Phys. Control. Fusion, 52(12):125008, 2010.

J. Howard, R. Jaspers, O. Lischtschenko, E. Delabie, and J. Chung

Imaging charge exchange recombination spectroscopy on the TEXTOR tokamak.

Plasma Phys. Control. Fusion, 52(12):125002, 2010.

S. K. Nielsen, H. Bindslev, M. Salewski, A. Buerger, E. Delabie, V. Furtula, M. Kantor, S. B. Korsholm, F. Leipold, F. Meo, P. K. Michelsen, D. Moseev, J. W. Oosterbeek, M. Stejner, E. Westerhof, P. Woskov, and the TEXTOR team

Fast-ion redistribution due to sawtooth crash in the textor tokamak measured by collective thomson scattering.

Plasma Phys. Control. Fusion, 52(9):092001, 2010.

S. B. Korsholm, M. Stejner, S. Conroy, G. Ericsson, G. Gorini, M. Tardocchi, M. von Hellermann, R. J. E. Jaspers, O. Lischtschenko, E. Delabie, H. Bindslev, V. Furtula, F. Leipold, F. Meo, P. K. Michelsen, D. Moseev, S. K. Nielsen, and M. Salewski
Development of novel fuel ion ratio diagnostic techniques.
Rev. Sci. Instrum., 81(10):10D323, 2010.

O. Marchuk, Yu. Ralchenko, R. K. Janev, W. Biel, E. Delabie, and A. M. Urnov
Collisional excitation and emission of H-alpha Stark multiplet in fusion plasmas.
J. Phys. B: At. Mol. Opt. Phys., 43(1):011002, 2010.

M. Hoelzl, S. Guenter, I. G. J. Classen, Q. Yu, E. Delabie, and the TEXTOR Team
Determination of the heat diffusion anisotropy by comparing measured and simulated electron temperature profiles across magnetic islands.
Nucl. Fusion, 49(11):115009, 2009.

G. Telesca, E. Delabie, O. Schmitz, S. Brezinsek, K. H. Finken, M. von Hellermann, M. Jakubowski, M. Lehnen, Y. Liang, A. Pospieszczyk, U. Samm, M. Tokar, B. Unterberg, G. Van Oost, and TEXTOR Team
Carbon transport in the stochastic magnetic boundary of TEXTOR.
J. Nuc. Mat., 390-91:227–231, 2009.

E. Delabie, R. J. E. Jaspers, M. G. von Hellermann, S. K. Nielsen, and O. Marchuk
Charge exchange spectroscopy as a fast ion diagnostic on TEXTOR.
Rev. Sci. Instrum., 79(10):10E522, 2008.

R. J. E. Jaspers, M. G. von Hellermann, E. Delabie, W. Biel, O. Marchuk, and L. Yao
Validation of the ITER CXRS design by tests on TEXTOR.
Rev. Sci. Instrum., 79(10):10F526, 2008.

O. Marchuk, G. Bertschinger, W. Biel, E. Delabie, M. G. von Hellermann, R. Jaspers, and D. Reiter
Review of atomic data needs for active charge-exchange spectroscopy on ITER.
Rev. Sci. Instrum., 79(10):10F532, 2008.

G. W. Spakman, G. M. D. Hogeweyj, R. J. E. Jaspers, F. C. Schüller, E. Westerhof, J. E. Boom, I. G. J. Classen, E. Delabie, C. Domier, A. J. H. Donné, M. Yu. Kantor, A. Krämer-Flecken, Y. Liang, N. C. Luhmann, Jr., H. K. Park, M. J. van de Pol, O. Schmitz, J. W. Oosterbeek, and Textor Team
Heat pulse propagation studies around magnetic islands induced by the Dynamic Ergodic Divertor in TEXTOR.
Nucl. Fusion, 48(11):115005, 2008.

Active beam spectroscopy

Contents

2.1	Introduction	10
2.2	Charge exchange spectroscopy	10
2.2.1	Overview	10
2.2.2	Isolating the active charge exchange component	11
2.2.3	The physics of charge exchange spectroscopy	12
2.2.4	Atomic physics effects on the charge exchange line shape	20
2.2.4.1	Effect of fine structure on the line shape	20
2.2.4.2	Charge exchange cross section effects	22
2.2.4.3	Charge exchange from excited states in the neutral beam	24
2.2.4.4	Halo neutrals	26
2.2.4.5	The plume effect	27
2.2.5	Fast ion charge exchange spectroscopy	29
2.3	Neutral beam attenuation	30
2.4	Beam emission and motional Stark effect spectroscopy	31
2.4.1	Overview	31
2.4.2	Fitting of the beam emission spectrum	32
2.4.3	Beam emission as a neutral beam diagnostic	35
2.4.3.1	Beam in plasma emission	35
2.4.3.2	Beam in gas emission	35
2.4.4	The Motional Stark effect diagnostic	38
2.5	Active hydrogen beam spectroscopy on TEXTOR	42
2.5.1	Introduction	42
2.5.2	CXS periscopes and lines of sight	42
2.5.3	Spectrometers and ccd cameras	44
2.5.4	Calibration	45
2.5.5	Data acquisition and analysis	46
2.6	Outlook	46

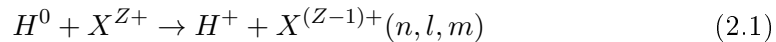
2.1 Introduction

Active beam spectroscopy has been reviewed several times [8, 9, 10] and is described in textbooks on plasma diagnostics [11]. Reports on the implementation on many machines can be found in literature. Most of these publications, however, only very partially cover the subject. So, despite a large number of publications related to the subject, the information is rather scattered. This chapter will specifically focus on the physics underpinning the diagnostic in order to better situate the work described in chapters 3 and 4 within the field of research. Section 2.2 focuses on charge exchange spectroscopy, while sections 2.3 and 2.4 deal with the attenuation and the emission of the beam itself. Section 2.5 describes the diagnostic implementation on TEXTOR.

2.2 Charge exchange spectroscopy

2.2.1 Overview

Active charge exchange spectroscopy (abbreviated CXS, CXRS or CHERS) is the study of the light emitted following the stimulated occurrence of reaction 2.1 and can be used to obtain information on the velocity distribution of the probed ions as well as on their density.



The neutral atom on the left hand side of reaction 2.1 is injected by a neutral beam, which can be a heating or a diagnostic beam, by a gas puff or by a solid pellet, and the neutral atom can either be H, D, He or Li, but we will restrict ourself to the most common case of hydrogenic beams.

Initially [12, 13], the main application of CXRS was to obtain information about impurity densities and to assess the effect of charge exchange by impurities on the neutral beam heating efficiency. Neutral beam heating was still a novel technique in the late '70s and knowledge about the beam stopping cross sections was still rather incomplete. Aside from obtaining the impurity densities, is CXS now in the first place used to measure the ion temperature (by eq. 2.2) and plasma rotation (by eq. 2.3). This is now a nearly routine task. σ and $\Delta\lambda$ represent the Doppler width and Doppler shift of the gaussian spectral line, γ is the angle between line of sight and the direction of the bulk motion, λ_0 is the natural wavelength and m is the mass of the emitting ion.

$$k_b T_i = \frac{mc^2}{2} \left(\frac{\sigma}{\lambda_0} \right)^2 \quad (2.2)$$

$$v_{rot} = \frac{\Delta\lambda c}{\lambda_0 \cos \gamma} \quad (2.3)$$

The first active CX spectroscopy was done in the ultraviolet, it was quickly realised however that several transitions with emission in the visible could be used as well. One advantage of looking at longer wavelengths is that the Doppler broadening and

Doppler shift is larger, which makes the use of CXRS to measure the ion temperature and plasma rotation [14, 15] easier (see eq. 2.2 and 2.3). A second advantage of spectroscopy in the visible is that the spectroscopic equipment can be placed outside the main experimental hall by using glass fibers to guide the light. This quickly led to the development of multi-channel CXRS diagnostics by the mid '80s on several leading tokamaks (Doublet-III [16], JET [17, 18], TFTR [19]).

The first step in the analysis of CXRS spectra is fitting to extract the information contained in the active component, this procedure is described in sect. 2.2.2. Eq. 2.2 and 2.3 are only valid in the assumption that Doppler broadening is the dominant mechanism determining the spectral line shape. Atomic physics effects can distort this simple picture and these will be discussed in section 2.2.4. But whereas the involved atomic physics will only lead to a 'correction' of the ion temperature and rotation, understanding of all involved atomic processes is crucial for relating the observed CX line intensity (I_{cx}) to the impurity density (n_i). Eq. 2.4 expresses this relationship using an effective charge exchange emission rate (Q_{cx}). The charge exchange emission rate, for a certain beam energy E , will generally depend on the set of local plasma parameters $\alpha = (n_e, T_{e,i}, \mathbf{c}_i)$, which consists of the electron density, ion and electron temperature and the impurity concentrations. Section 2.2.3 describes how Q_{cx} is calculated.

$$n_i = \frac{I_{cx}}{\sum_E \sum_m Q_{cx}^{E,m}(\alpha) n_b^{E,m}} \quad (2.4)$$

The local neutral beam density ($n_b^{E,m}$ in eq. 2.4) in quantum state m , belonging to the beam population with energy E , is needed to obtain the impurity density. The beam density can either be calculated by using eq. 2.5 or obtained via a measurement of the beam emission intensity (I_{bes}^E , eq. 2.6). $f^{E,m}$ is the relative fraction of the beam in state m , N_b^E is the initial beam density and $\sigma_{stop}^E(\alpha)$ is the effective beam stopping cross section.

Sect. 2.3 describes the first technique and sect. 2.4 is a review of the latter technique. Chapter 3 contains a paper that describes recent progress in the validation of the beam emission rates Q_{bes} .

$$n_b^{E,m} = f^{E,m}(\alpha) N_b^E \exp\left(-\int dl \sigma_{stop}^E(\alpha) n_e\right) \quad (2.5)$$

$$n_b^{E,m} = f^{E,m}(\alpha) \frac{I_{bes}^E}{Q_{bes}^E(\alpha) n_e} \quad (2.6)$$

2.2.2 Isolating the active charge exchange component

In expressions 2.2-2.4 we have assumed that the active charge exchange (ACX) line of a maxwellian ion population can be adequately described by a gaussian parametrized by its width, peak position and intensity. Hence, the first step in analysing charge

exchange spectra comes down to fitting a gaussian to the ACX component. However, the active line of interest will in general be blended with emission from not fully ionized impurities that can exist in the colder plasma edge and with passive charge exchange (PCX) emission from the interaction with thermal neutral particles recycling at the wall. These parasitic emission lines can be subtracted from the spectrum by modulating the neutral beam, assuming the plasma is not altered during one modulation cycle. This assumption is only true if either the modulation is very fast or the beam power is low enough such that it does not distort the ionization balance. Dedicated diagnostic beams have been developed for this purpose. Alternatively, when using the heating beams for CXRS the beam power is often sufficiently high such that the active emission is much brighter than the passive CX emission and both components can be distinguished by fitting, using the higher ion temperature and rotation in the plasma core compared to the edge localised PCX emission. Additional information that can help to constrain the PCX components can be obtained from passive lines of sight not intersecting the neutral beam or from the ion temperature and rotation close to the last closed flux surface.

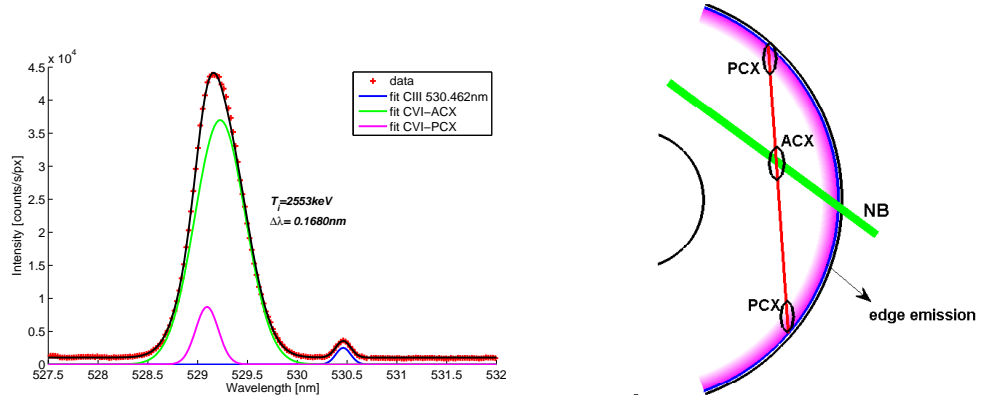
Fig. 2.1(a) shows a fitted spectrum of the C VI (n=8-7) charge exchange line from TEXTOR for a line of sight intersecting one of the heating beams. This is probably the most simple CX spectrum possible. Three lines are taken into account when fitting the spectrum: a CIII line from the edge which can be used as a wavelength reference, the active CX line and emission from passive CX. Fig. 2.1(b) shows the localisation of the emission layers. The difference in T_i and $\Delta\lambda$ make it possible to fit these two features to the C VI line which appears as a single asymmetric line. The assumption that the PCX emission can be approximated by a gaussian line is less valid than for the ACX component, but induces no considerable errors if the PCX intensity is low compared to the ACX intensity. Work carried out modelling the PCX emission is described in [20, 21].

Much more complicated CX spectra than the one shown in fig. 2.1 have been used for the diagnosis of tokamak plasmas. 'Recipes' to analyse the most commonly used CX spectra, based on experience gained from several tokamaks, can be found in [22]. Crucial in the analysis of more complex spectra is the identification of all lines such that natural wavelengths and relative transition probabilities can be used to reduce the number of free parameters by coupling. The fact that many of these techniques can be reliably used is thanks to an ongoing collaboration between atomic physicists and plasma spectroscopists. The software package CXSFIT [23], originally developed at JET and now maintained by ADAS ¹, allows efficient interactive fitting with several parameter coupling options.

2.2.3 The physics of charge exchange spectroscopy

The effective charge exchange emission rate $Q_{cx}(\alpha)$ introduced in eq. 2.4 determines the intensity of the observed spectral line and is needed to relate the ACX intensity

¹Atomic Data and Analysis Structure, <http://www.adas.ac.uk>

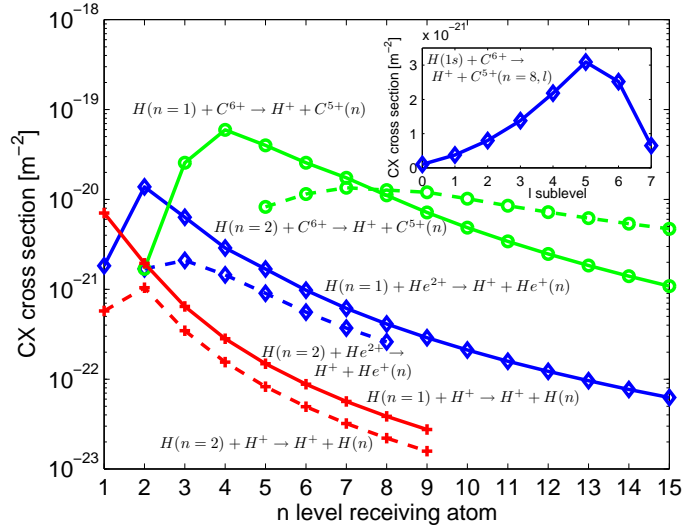


(a) Fitted active C VI ($n=8-7$) spectrum from TEX-TOR #111515. (b) Localization of the emission contributing to the measured spectrum.

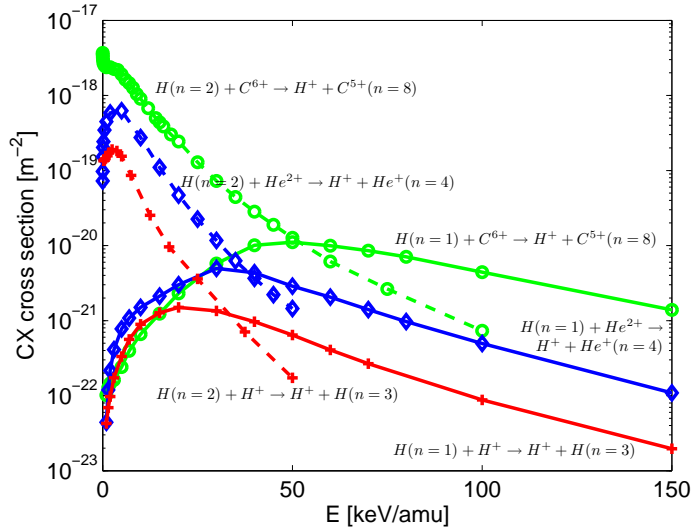
Figure 2.1: Example C VI charge exchange spectrum and the spatial localization of the components fitted to the spectrum.

to the density of the ion of interest. The primary reaction involved in constructing the effective emission rate is charge transfer from the donor atom to an (excited) state of the receiving atom, where it can then decay radiatively or be redistributed collisionally. CX cross sections are very large at low collision energies and very selective in the nl -levels that are populated.

The charge exchange cross sections between $H(n=1,2)$ and H^+ , He^{2+} and C^{6+} are shown in fig. 2.2. The data shown in fig. 2.2 are taken from ADAS data files, which contain a compilation of cross sections from various, mainly theoretical, sources. We will not discuss the possible methods to calculate the fundamental cross sections; an overview can be found in [25]. An intuitive semi-classical approach can partially explain the Z - and n -scaling of these cross sections [11]. Consider an electron moving in the attractive potential of two ions separated by a distance r : a fully stripped ion with charge Z and a hydrogen nucleus to which the electron is initially bound. At low impact energies, the time the electron needs to orbit around the nucleus is smaller than the collision time and the probability for a CX reaction to occur only depends on the possibility of a path leading from a bound state on the hydrogen atom to the ion. For all internuclear distances smaller than r_{max} , there exists a point on the electron orbit where the force attracting the electron to each of the nuclei is the same and the probability to remain bound to one of the ions is the same as to the other ion. On a line from one nucleus to the other the potential energy is $V = -e^2/(4\pi\epsilon_0)(Z/(r - r_H) - 1/r_H)$ with r_H the distance to the hydrogen nucleus. The maximum of this potential barrier that the electron has to overcome to move from the hydrogen nucleus to the ion is $V_{max} = -e^2/(4\pi\epsilon_0 r_{max})(1 + \sqrt{Z})^2$. This is sketched in fig. 2.3. The electron, which is initially in state n_H , will be able to move



(a) n -dependence of cross sections for charge exchange between $H(n=1,2)$ and H^+ , He^{2+} and C^{6+} at an impact energy of 50keV/amu . The position of the peak in the cross sections increases with n_H and Z . The inset in the upper right shows the l -dependence of the cross section for CX from ground state H into $C^{5+}(n=8)$ at 50keV/amu .



(b) Energy dependence of charge exchange cross sections between $H(n=1,2)$ and H^+ , He^{2+} and C^{6+} into the upper levels of the receiving atoms ($n=3, 4$ and 8 respectively) that contribute most to commonly measured CXRS spectra. CX from the excited states becomes very important at low impact energies.

Figure 2.2: n -resolved charge exchange cross sections for $H(n=1,2)$ impact on the fully stripped low- Z impurity ions that are most of interest for CXRS, compiled from ADAS adf01 data files [24].

to this point if V_{max} is low enough such that it equals the initial potential energy of the electron, perturbed by the Coulomb attraction of the ion with charge Z . This can be expressed as $V_{max} = -Ry/n_H^2 - e^2Z/(4\pi\epsilon_0r_{max})$. The two expressions of V_{max} can be combined to obtain an expression for the internuclear distance that allows a charge exchange reaction, $r_{max} = (e^2n_H^2)/(4\pi\epsilon_0Ry)(1 + 2\sqrt{Z})$. This gives us the cross section at impact velocities smaller than the orbital velocity of the electron, summed over all n (eq. 2.7).

$$\sigma_{cx} = \frac{\pi r_{max}^2}{2} = 2\pi h^2 c^2 a_0^2 n_H^4 (1 + 2\sqrt{Z})^2 \quad (2.7)$$

The principal n -shell into which the electron will be caught can be found by using $V_{max} = -RyZ^2/n_Z^2 - e^2/(4\pi\epsilon_0r_{max})$. This yields eq. 2.8.

$$n_Z = n_H Z \left(\frac{1 + 2\sqrt{Z}}{2\sqrt{Z} + Z} \right)^{1/2} \approx n_H Z^{3/4} \quad (2.8)$$

This simple model described here can already explain some of characteristics of the CX cross sections shown in fig.2.2. The position of the peak in the cross sections in fig. 2.2(a) appears at higher n_Z for higher Z and also doubles when going from $n_H=1$ to 2, according to eq. 2.8. In fig. 2.2(b), one can see that in the low energy limit, the charge exchange cross section becomes very large for excited hydrogen and the cross section increases approximately linearly with Z , as predicted in eq. 2.7. For neutral beam energies that are currently in use ($\approx 50\text{keV/amu}$), charge exchange from excited states in the beam will especially be important for the fractional energy components (see sect. 2.2.4.3). In the upper right corner of fig. 2.2(a) the l -resolved cross sections for CX to the $n=8$ shell of C^{5+} is shown. The cross section is strongly peaked to higher l -states. This can also be understood from our simple model. We assumed the electron was transferred from the hydrogen atom to the ion Z when the potential on a line between both nuclei was just low enough. This implies that the electron was moving towards the nucleus Z . Hence, states with on average a direction of motion towards the nucleus are more likely.

In fig. 2.2(b) one can see that the CX cross sections drop sharply with energy ($\sigma_{cx} \propto E^{-7/2}$), in contrast with the simple intuitive model described here which does not depend on energy. This is because when the impact velocity becomes comparable to the electron velocity, the time during which the atom is close enough to the ion for a CX interaction to occur should be taken into account, as well as the higher electron velocity which is needed to compensate for the movement of the ion.

The next step in the reaction which is of interest to us, once the electron is in an excited state of the receiving ion, is radiative decay. The selection rules only allow transitions with $\Delta l = \pm 1$. Because mostly high l -states are populated by charge exchange and $l=0..n-1$, the most important transition becomes $\Delta l=1, \Delta n=1$ [9]. This is called the yrast sequence. The electron thus cascades down rather than to decay directly to the ground state. This is favorable for charge exchange spectroscopy

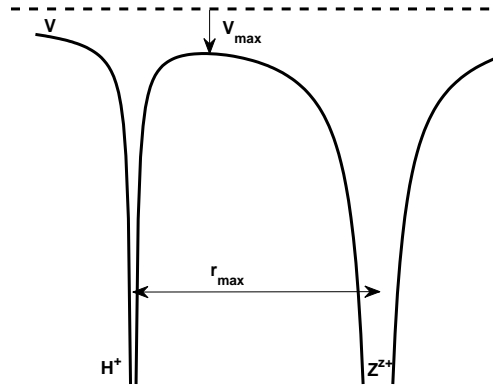
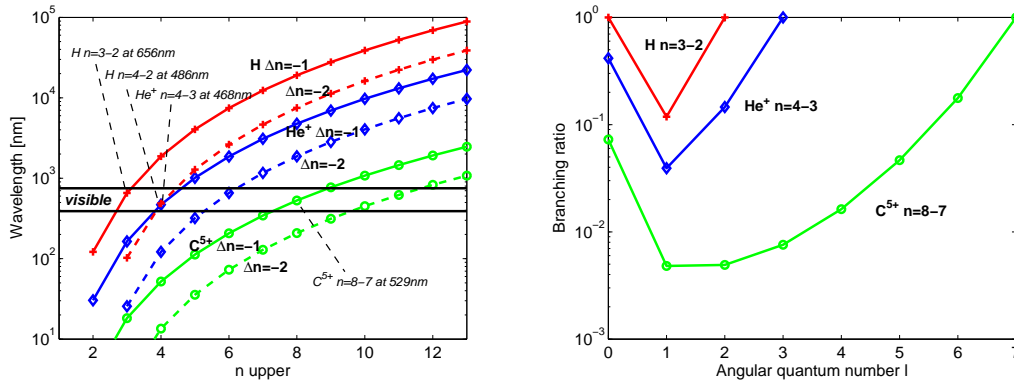


Figure 2.3: Classical potential energy of an electron attracted to two nuclei. In the low collision energy limit, a charge exchange reaction occurs if the distance between the two nuclei is at most r_{max} such that the potential V_{max} is low enough to let an electron cross the barrier.



(a) Wavelengths of $\Delta n=1$ and $\Delta n=2$ transitions of interest for CXRS. Transitions in the visible occur at upper n -levels slightly above the ones preferentially populated by charge exchange. (b) Branching ratios for $\Delta n=1$ transitions of interest for CXRS as a function of the l -number of the initial state.

Figure 2.4: Wavelengths of transitions of possible interest for CXRS and branching ratios for these transitions as a function of angular quantum number l .

because several $\Delta n=1$ lines are in the visible. Fig. 2.4(a) shows the wavelengths corresponding to $\Delta n=1$ and $\Delta n=2$ transitions in H, He⁺ and C⁵⁺. The visible lines are typically from upper n -states just beyond the peak in the cross section shown in fig. 2.2(a), but the cross sections are still large enough to ensure sufficient population by charge exchange.

For the calculation of the effective emission rates one has to go further than

calculating only the radiative decay of states populated by CX. All possible collisional processes have to be taken into account that can cause a redistribution of the excited population before the electron is lost again through ionization or charge exchange. For the density of particles in each state n we can write down the balance equation (eq. 2.9) using the cross sections for all of the involved processes, assuming the plasma is optically thin². The summation over α is over electrons, bulk ions and impurities present in the plasma. The notion electron loss stands for both ionisation and charge exchange with bulk ions that cause the electron to be lost from our population.

$$\begin{aligned}
\frac{dN_n}{dt} = & \overbrace{\sum_{n'>n} A_{nn'} N_{n'}}^{\text{radiative gain}} - \overbrace{\sum_{n'<n} A_{n'n} N_n}^{\text{radiative loss}} \\
& + \overbrace{\sum_{\alpha} \sum_{n' \neq n} \langle \sigma_{nn'}^{\alpha} v \rangle N_{n'} N_{\alpha}}^{\text{collisional (de)excitation into } n} - \overbrace{\sum_{\alpha} \sum_{n' \neq n} \langle \sigma_{n'n}^{\alpha} v \rangle N_n N_{\alpha}}^{\text{collisional (de)excitation out of } n} \\
& - \overbrace{\sum_{\alpha} \langle \sigma^{\text{loss}} v \rangle N_n}^{\text{electron loss}} + \overbrace{S_{ext}}^{\text{external sources}}
\end{aligned} \tag{2.9}$$

The external source term in eq. 2.9 is the beam driven charge exchange term (eq. 2.10). N_Z is the density of the fully stripped impurity ion that is the parent of the population N_n . N_b is the neutral beam density.

$$S_{ext} = \langle \sigma^{cx} v \rangle N_b N_Z \tag{2.10}$$

The set of equations 2.9 constitute a collisional-radiative (CR) model [26]. In the assumption of a steady state plasma and beam, $dN_n/dt = 0$, the densities N_n can be obtained from eq. 2.9 by matrix inversion. The effective CX emission rate for a transition $n \rightarrow n'$ can be derived from the populations by using eq. 2.11. In practice eq. 2.9 is solved for $N_n/N_Z N_b$ instead of N_n .

$$Q_{cx} = \frac{A_{n'n} N_n}{N_Z N_b} \tag{2.11}$$

Q_{cx} depends on the electron and ion temperature because of the averaging of the cross sections over the (maxwellian) velocity distribution and on the electron and (impurity) ion densities through their appearance in the excitation and loss terms of eq. 2.9.

The hidden difficulty in the balance equations (eq. 2.9) is not only that all cross sections must be known over the relevant energy range but also in the choice of the

²Opacity induces non-local effects as well as the need to take absorption into account in eq. 2.9

energy levels n , which do not necessarily coincide with the principal quantum numbers n . This number of states is always infinite, but for practical purposes, the CR modelling can be truncated due to the strong decay of the CX cross sections with n . The levels n are supposed to correspond to eigenstates of the atom of interest, given the relevant external magnetic and electric fields. Although we are only interested in transitions between states with different principal quantum number n , both the charge exchange cross sections depend strongly on the orbital quantum number l and so do the radiative rates, hence collisions that redistribute the l -population have a strong effect on the observed line intensities. This is referred to as l -mixing. For an atom only perturbed by a weak external magnetic field, the natural choice of the energy levels and states in the CR model are those corresponding to the spherical eigenstates $n \equiv (n, l, j, m_j)$. In hot magnetized plasmas, the thermal motion of the ions in the magnetic field induces a Lorentz electric field $E_L = q\mathbf{v} \times \mathbf{B}$, which causes a mixing of the spherical eigenstates and split of the energy levels by the motional Stark effect. In this case, the natural choice would be to characterize the states according to their parabolic quantum numbers $n \equiv (n, k_1, k_2, m)$. It does in principle not matter which set of eigenstates one uses, for low field strengths each orbital from one set can be described as a linear combination of orbitals from the other set, but translating cross sections from one picture to another can be hard because the eigenstates can be aligned along different axes. Therefore, taking the full hamiltonian into account in a single picture is difficult. Because cross sections are calculated in spherical coordinates and collisional l -mixing is dominant, it is customary to use those for CR modelling for CXRS. For MSE diagnostics (see sect. 2.4), one is interested in the line intensities of transitions between individual Stark states. Because the energy separation due to the Lorentz field is much larger than due to the magnetic field in this case, the parabolic states are most adequate for this purpose.

Because l -mixing is important for evaluation of the CX emission rates, some rules of thumb have been derived to assess if mixing needs to be taken into account or whether redistribution among l -states is unimportant. The CR model can strongly be simplified in the extreme cases of either no coupling between sublevels or full mixing in which case the sublevels have a statistical population³. Sampson [27] has derived an analytical formula (eq. 2.12, n_e is in m^{-3}) to assess the importance of collisional mixing from the assumption that mixing occurs if the collision rate between states with different l , but the same j , equals the total radiative decay rate of the collisionally coupled j level. Because collisional coupling goes fastest through the $j=1/2$ level that one is used to derive the general expression (2.12) for all n .

$$n \geq 59.29 \left(\frac{Z^{7.5}}{n_e} \right)^{\frac{1}{8.5}} \quad (2.12)$$

As noted above, motional Stark mixing is more difficult to take into account. A rule

³A statistical population means a population according to the degeneracy of the state.

of thumb for the onset of collisional mixing has been derived by Fonck [15] starting from the assumption that mixing occurs if the separation of energy levels in the atom due to the Motional Stark effect becomes equal to fine-structure separation. The n -level from which onwards this occurs is given in eq. 2.13. MSE mixing will be important at high T_i (in keV) and B (in T). In tokamak plasmas, collisional mixing is more important than motional Stark mixing.

$$n \geq 1.91 \left(\frac{Z^{11}}{T_i B^2} \right)^{\frac{1}{12}} \quad (2.13)$$

The criteria for mixing of sublevels (2.12-2.13) are plotted in figure 2.5. The n -levels that correspond to $\Delta n=1$ transition in the visible are all subject to collisional and motional Stark mixing, but they do not reach a full statistical population yet. As illustrated by Boileau et al. [18], a full CR model for CXS needs to take the sublevels into account explicitly.

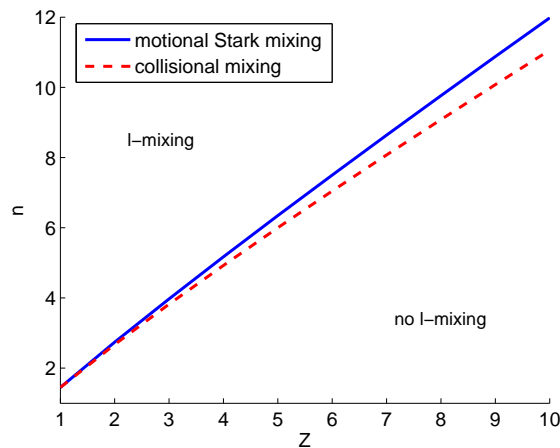


Figure 2.5: Criterium for motional Stark [15] and collisional mixing [27] of sublevels. $n_e=5 \cdot 10^{19} \text{m}^{-3}$, $T_i=3 \text{keV}$, $B=3 \text{T}$. The sublevels belonging to n -states that give rise to transitions in the visible are mixed by both collisions and the motional Stark field.

Above, we have outlined how the CX emission rates can be calculated and which considerations are to be taken into account. In practice, the ADAS306 and ADAS308 codes from ADAS [24] are (nlj) - and (nl) -resolved solvers for the full CR model. Details on the atomic physics considerations and default collision rates at the base of the ADAS CX collisional radiative model are described in [28]. The ADAS CX rates are considered to be the most reliable and are widely used within the fusion community and have been used in the following chapters of this thesis. Fig. 2.6 shows the effective ADAS CX emission rates for H ($n=3-2$), He^+ ($n=4-3$) and C^{5+} ($n=8-7$) as a function of the H beam energy.

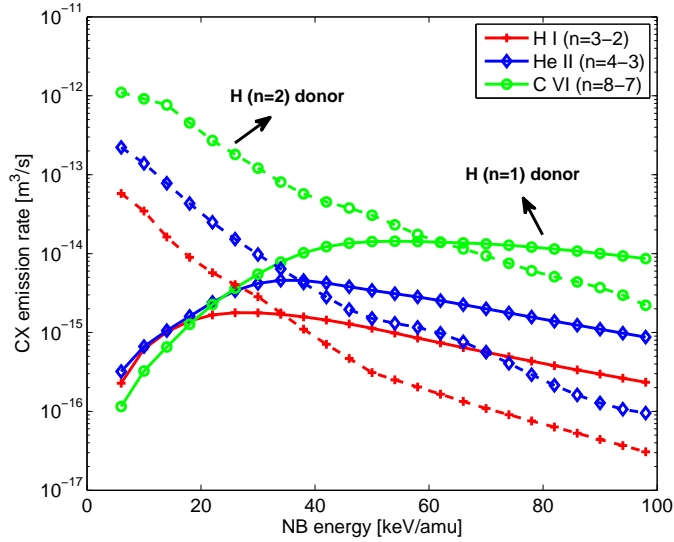


Figure 2.6: NB energy dependence of the ADAS effective charge exchange emission rates for the H I ($n=3-2$), He II ($n=4-3$) and C VI ($n=8-7$) transitions for ground state and excited donor atoms. [24]. $n_e=3 \cdot 10^{19} \text{m}^{-3}$, $T_e=T_i=3 \text{keV}$.

2.2.4 Atomic physics effects on the charge exchange line shape

2.2.4.1 Effect of fine structure on the line shape

The fine structure of the principal energy levels as well as the splitting due to magnetic and electric fields can alter the CX line shape to such extent that an appreciable deviation occurs with regard to the simple Doppler broadened gaussian. The eigenenergies of the full hamiltonian can be calculated numerically (see e.g. [29]), but analytical solutions (in first or second order perturbation theory) only exist taking into account a single perturbation term. Therefore it is useful to estimate the importance of each term separately.

Fonck et al. [15] considered the fine structure to be the most important effect to take into account. The energy shift due to spin-orbit coupling (in (nlj) -representation) is given by eq. 2.14 and scales as Z^4/n^3 . The effect is negligible for the visible transitions in H and He^+ , but can lead to an error of $\approx 10\%$ on the measured C or O ion temperature at about 200eV [15]. The relative importance of the fine structure broadening compared to the Doppler broadening decreases strongly with increasing T_i .

$$\Delta E_{SO} = \frac{\alpha^2 Ry Z^4}{2 n^3} \frac{j(j+1) - l(l+1) - 3/4}{l(l+1/2)(l+1)} \quad (2.14)$$

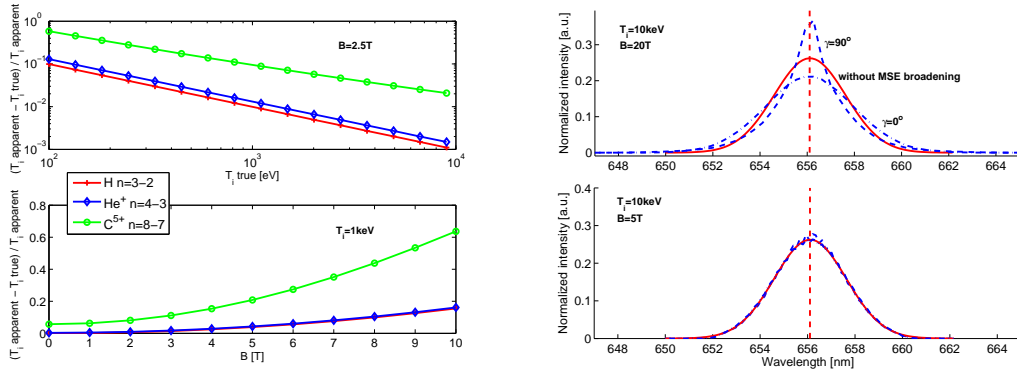
For strong magnetic fields (Paschen-Back effect) the energy shift due to the magnetic field is given by eq. 2.15 (in (nls) -representation). The energy shift is in-

dependent of Z and the ion mass. The Doppler shift is proportional to the velocity $v \propto 1/\sqrt{M}$, hence especially heavier elements will be effected. The visible transitions in higher Z elements occur at higher n , which implies higher m_l levels as well. Blom et al. [30] have calculated the spectral broadening due to both the fine structure and the external magnetic field in the assumption of a statistical population. They have parametrized the full multiplet by a sum of 3 gaussians, which closely resembles the actual multiplet. In the absence of a magnetic field their data are consistent with those of Fonck et al. [15]. From a magnetic field strength of approximately 3T onwards, the influence of the magnetic field on the C VI CX-line becomes as important as the fine structure correction. We have fitted the parametrized multiplets given by Blom et al. with a single gaussian and compared the apparent and true ion temperature as a function of temperature and magnetic field. The results of this is shown in Fig. 2.7(a). For typical tokamak plasmas, the corrections stays below 10%, but one has to be careful with C VI measurements in the plasma edge. Note that fine structure can also generate an apparent line shift if the upper level does not have a statistical population.

$$\Delta E_B = \frac{e_0 \hbar}{2m_e} (m_l + 2m_s) B \quad (2.15)$$

Due to their motion in a strong magnetic field, plasma ions and atoms in a tokamak experience a strong Lorentz electric field. The energy shift of hydrogen-like energy levels corresponding to this force is given by eq. 2.16 (in (nk_1k_2) -representation). Unlike the previous spin orbit coupling and magnetic field broadening mechanisms that tend to become less important at higher temperature, this effect is linear in the velocity, just like the Doppler broadening. Hence at sufficient high temperatures, MSE broadening will be the dominant fine structure generated broadening mechanism. For this reason it is important to assess the importance of MSE broadening. Therefore we have made a numerical simulation of MSE broadening and applied it to the most important hydrogen-like transitions. The results of this simulation applied to the D_α line are shown in fig. 2.7(b) for a 5T and 20T magnetic field. The results are somehow surprising at first sight. One would expect a much stronger broadening, especially for a view perpendicular to the magnetic field when the particles that contribute to the wings in the spectrum experience the strongest Lorentz field. However these particles will only emit σ -radiation, which has a smaller or zero shift in the direction of the observer and hence both effects partially cancel each other. Note that this is less the case for the rarely used D_β emission line which has also sigma components with higher wavelength shifts. Our results slightly deviate from those obtained earlier by Mandl [29], but the conclusion remains that the effect can be safely neglected at magnetic fields currently used in tokamaks and the effect will at high fields first start to be important for deuterium emission lines because of the n/Z scaling in eq. 2.16.

$$\Delta E_{MSE} = \frac{3}{2} e_0 a_0 (k_1 - k_2) \frac{n}{Z} \mathbf{v} \times \mathbf{B} \quad (2.16)$$



(a) Apparent ion temperature increase due to fine structure and magnetic field broadening of the H (3-2), He⁺ (4-3) and C⁵⁺ (8-7) emission lines using the parametrization from [30], in case the emission line would be fitted by a single gaussian. The effects are only important for low ion temperatures and heavier elements. The angle between line of sight and magnetic field is 20° . (b) Numerical simulation of the effect of MSE broadening on the D α line for a view parallel ($\gamma=0^\circ$) and perpendicular ($\gamma=90^\circ$) to the magnetic field. The results shown here slightly deviate from those obtained by W. Mandl [29], but the conclusion remains that the effect is only important at magnetic fields above 10T.

Figure 2.7: Effect of spin orbit coupling, magnetic field and motional Stark field broadening on the CX line shape.

2.2.4.2 Charge exchange cross section effects

The energy dependence of the charge exchange cross sections can possibly distort the CX line shape and emission rate in high temperature plasmas as the beam velocity cannot longer be assumed to be much larger than the thermal velocity of the plasma ions. Charge exchange with ions that have a relative velocity close to the peak in the cross sections is favored over CX reactions with either more or less energetic ions. Therefore this effect usually leads to a reduction of the observed ion temperature. The importance of the cross section effect increases with temperature and is especially important for light elements. If the distortion of the emission line is sufficiently small, the line can still be assumed gaussian, but with a different width, position and intensity. The differences between the observed and true T_i , v_{rot} and Q_{cx} are referred to as cross section corrections. Because a measured spectrum corresponds to the velocity distribution along a line of sight of the ions that have undergone charge exchange, the cross section corrections will be sensitive to the angle between line of sight and neutral beam. The cross section correction for the plasma rotation will also depend on the angle between line of sight and toroidal direction.

A first report of cross section effects to explain discrepancies between plasma rotation measured on the heating and diagnostic beam on TFTR is made by Howell et al. [19]. Von Hellermann et al. describe in detail both a computational [31] and

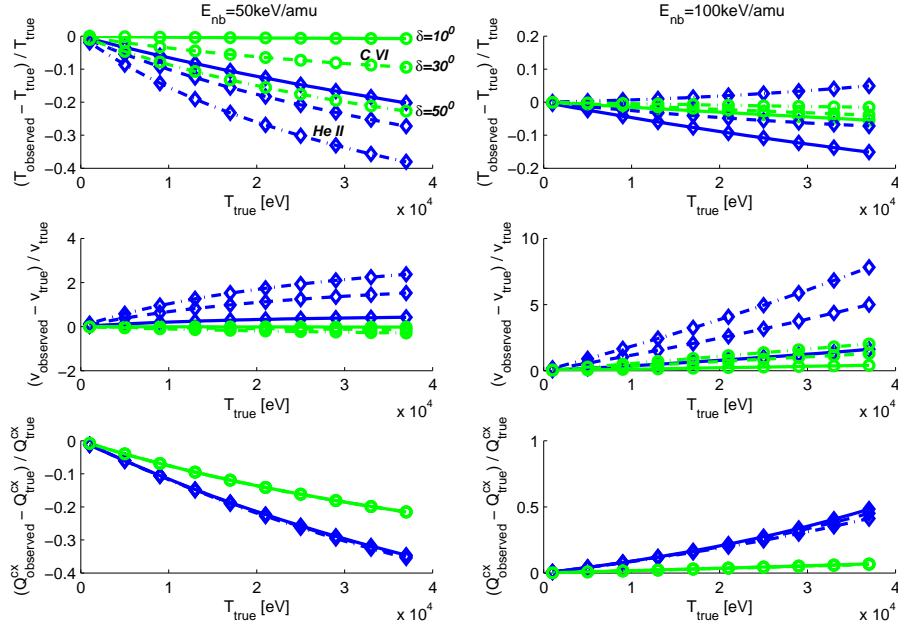


Figure 2.8: Analytical cross section corrections to the observed temperature, toroidal rotation and emission rate for the He II ($n=4-3$) and C VI ($n=8-7$) CX lines as a function of temperature, using the formulas of [32] and ADAS data for a hydrogenic beam energy of 50 and 100keV/amu. A rotation of 100km/s is used for this illustration and, like in most tokamaks, the lines of sight are tangential to flux surfaces at the intersection points with the NB.

analytical [32] method to take the cross section effects into account. Fig. 2.8 plots the cross section corrections for the He II ($n=4-3$) and C VI ($n=8-7$) CX lines for a JET-like NB (50keV/amu) and for the ITER DNB (100keV/amu). As expected, the effect is clearly larger for the lighter helium than for carbon and the effect on the ion temperature and rotation increases with the angle δ between l.o.s. and the direction perpendicular to the beam, but in the plane of the line of sight and NB. For the calculation of the correction on the rotation a plasma velocity of 100km/s has been assumed for this illustration. At low rotation velocities, but high temperatures, the correction can be of the same magnitude or even larger than the velocity itself, even for the C VI CX line. This is especially important for measurements of the poloidal plasma velocity.

For a full treatment of the cross section corrections, charge exchange from excited beam neutrals and the power fractions within the beam must be accounted for as well.

Solomon et al. [33] pointed out that one can overcome the atomic physics calcu-

lations for correcting the observed plasma rotation when measuring simultaneously on a co- and counter-NB. The results of their measurements were compared with the atomic physics calculations. A tendency to overcorrect was observed, unless the excited beam population for the lower energy fractions in the beam was enhanced over the expected values. Given the striking resemblance between this observation and the results of corrections to the modelling of excited beam populations in chapter 3, this observation does not disvalidate the atomic physics calculation of the cross section effect, it only points out the need for correct cross sectional and neutral beam data.

When the ion temperature becomes too high compared to the beam voltage, the emission line becomes too much distorted and the gaussian approximation is not longer valid. According to [32], a rule of thumb for this temperature is given by eq. 2.17.

$$T_i > \frac{M_z}{10M_{nb}} E_{nb} \quad (2.17)$$

This could especially be a concern for light elements. For H I CXS, this maximum temperature for a 50keV/amu beam is as low as 5keV. We have implemented a numerical simulation of the cross section effect, resembling the description given in [31] and applied this to a maxwellian velocity distribution. We fitted a gaussian line to the result to see the deviation. In most cases, the gaussian approximation could be safely used up to much higher temperatures then given by eq. 2.17. In fig. 2.9 a numerical simulation of the D α -CX spectrum is compared with the Doppler broadened gaussian in the absence of cross section effects and with the best fitting gaussian for the rather extreme conditions of a beam energy of 50keV/amu and an ion temperature of 20keV. Although the effect of the cross section effect is very large, the emission line is still approximately gaussian.

2.2.4.3 Charge exchange from excited states in the neutral beam

When evaluating the effective charge exchange emission rate, charge exchange from excited hydrogen in the neutral beam should be taken into account. The excited fraction in the beam is typically 0.2-0.5%, but at low collision energies the CX cross sections can be several orders of magnitude larger than for ground state charge exchange. Hence, taking into account the excited states is especially important at low NB voltages or for fractional energy components in positive ion neutral beams.

The importance of the excited states was first pointed out by Rice et al. [34] as a mechanism to populate highly excited states in Ar¹⁶⁺ by CX from intrinsic neutral hydrogen. First emission rates of beam driven CX with low-Z ions are published by Isler et al. [35]. Hoekstra et al. [36] have performed Classical Trajectory Monte Carlo (CTMC) calculations to obtain the CX cross sections from excited states and have implemented those in ADAS. The effective CX emission rates from the n=1 and n=2 levels of neutral hydrogen are shown in Fig. 2.6 using ADAS308 and the cross sections from [36], except for the H α line.

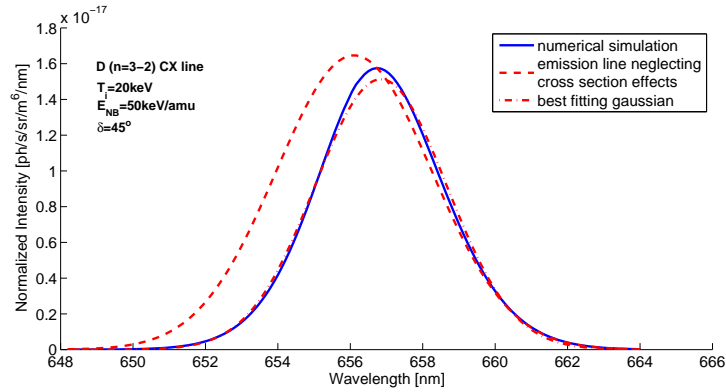


Figure 2.9: Numerical simulation of the cross section effect for the D ($n=3-2$) CX line (per beam atom and per D^+ ion along the l.o.s.), in comparison with the emission neglecting the cross section effect and the best fitting gaussian. The beam energy is 50keV/amu and the ion temperature is 20keV. The angle between line of sight and NB is 45° and is directed along the beam. Because the cross sections peak at lower beam energies the emission is shifted to the red wing.

In practice, the excited beam population $f(n)$ is calculated by a CR model dedicated to the beam population (see sect. 2.4), or from tabulated data obtained by this CR code. The effective CX emission rate can then be reconstructed as a linear combination of the ground state and excited state contributions (eq.2.18).

$$Q_{cx}^{\text{eff}} = \sum_{n=1..n_{max}} f(n) Q_{cx}^{\text{eff},n} \quad (2.18)$$

Because the effect of excited neutrals increases very fast when lowering the beam voltage under 50keV/amu, several experiments have been performed in which the plasma conditions (and hence the impurity concentrations) were kept constant, but the beam voltage was varied. Maggi et al. [37] have calculated C^{6+} and Ne^{10+} densities on ASDEX Upgrade with and without taking the $n=2$ population into account while changing the beam voltage from 15 to 30keV/amu. Not taking into account the $n=2$ population resulted in errors up to a factor of 10 at the lowest beam voltage, while a variation of the concentration within 20% over the voltage scan was obtained when taking the excited population into account. A similar experiment has been performed on TEXTOR by Jaspers et al. [38] with comparable results. Bepamyatnov et al. [39] have performed CXRS measurements of the B^{5+} density during a beam voltage scan on Alcator C-Mod. Taking into account the excited states in the beam up to $n=3$, the measured densities were consistent within the scatter.

It should be noted that the excited beam fraction that was used for the analysis of the experiments mentioned here was wrong by approximately 20% for $n=2$ and a factor of 2 for $n=3$ (see chap. 3 for a clarification of this issue). This could, as well as uncertainties on the beam power fractions when changing the beam voltage,

account for some of the remaining discrepancies in [37, 39].

2.2.4.4 Halo neutrals

The charge exchange reactions produce a population of product ions or atoms surrounding the beam. The direct emission following the primary CX reaction is what is of interest for charge exchange spectroscopy. However, the product atoms have a finite lifetime before being ionized and the atoms or ions that have decayed to the ground state can be excited again by electron or ion impact or via charge transfer. This can give rise to secondary or delayed emission. There is a conceptual difference when this occurs on hydrogen or on an impurity ion population. In the case of hydrogen, the population is neutral and not bound to the field line geometry anymore and the neutral cloud is called a beam halo, while impurity ions still follow the field lines and the delayed emission is referred to as a plume (sect. 2.2.4.5).

The neutral hydrogen halo formed around the beam leads to two effects: (1) the observed emission is not localized anymore to the intersection between the line of sight and the neutral beam and (2) the intensity of the hydrogen CX line will be enhanced and cannot be interpreted anymore by the single effective CX rate for the primary CX reaction. A possible third consequence is that CX reactions between the halo neutrals and impurity ions could affect the impurity CX lines. However, the collision energy in these thermal-thermal collisions will for tokamak plasmas be too low to excite the higher lying n-shells of interest.

Because the halo is not a local effect, a complete treatment is in principal 3D and depends on all plasma profiles as well as the beam and l.o.s. geometry as one has to track the neutral halo atoms from their birth place till ionization, accounting for all collisional processes. Note that time dependent codes developed for beam emission could be used for this if the rates are replaced by thermal-thermal reactions instead of beam-thermal reactions and a modification is made such that CX is a redistributive process instead of an electron loss reaction.

Mandl [29] approximated the calculations to a 2D integration in the assumption that the halo is predominantly in the ground state, hence only ionization from the ground state needs to be taken into account, and that D_α emission is observed whenever an atom is excited to $n=3$ by particle impact or charge exchange (coronal limit without cascading). The two relevant competing processes thus are ionisation of the neutral deuterium and CX and excitation to $n=3$. Ionisation peaks at higher energies and thus will an increasing temperature lead to a reduction of the halo emissivity. All processes scale linearly with plasma density, but at high densities the penetration length of the beam becomes smaller and contamination of the direct signal by halo from the edge could decrease the ratio between direct and halo light. The ratio between halo and direct emission drops as a function of beam voltage, because the total CX cross section drops faster with energy than the CX cross section that lead to a population of $n=3$ (or higher). At $T=5\text{keV}$ and $n_e=2 \cdot 10^{19} \text{ m}^{-3}$, the ratio

between halo and direct CX emission is in the order of 0.2 for a 40keV/amu beam according to Mandl's calculation [29] and reaches 1 for a beam energy of 13keV/amu. Note that the assumptions made by Mandl will overestimate the effect of the halo because ionisation from excited states is not taken into account, but the calculations give a good estimate of the importance of the effect.

2.2.4.5 The plume effect

The analogy of the halo for impurity ions is called the plume effect. The plume emission arises from ions that have undergone CX with the beam neutrals, flow along the field lines and are excited to the level of interest before being ionised. The first calculations on the plume intensity are by Fonck et al. [15] and depend on the beam and line of sight geometry, apart from the dependence on the electron density and temperature profiles. Excluding stepwise processes and neglecting the geometrical part, the intensity ratio plume to prompt will scale according to eq. 2.19. In words, the plume to prompt intensity scales with the excitation rate to n and the beam driven CX source rate of ions with charge $Z-1$, and is inversely proportional to the electron loss rate and the direct CX rate into n .

$$\frac{I_{plume}}{I_{acx}} \propto \frac{Q_{z-1}^{exc,n}(T) Q_z^{cx,tot}(E_{nb})}{Q_{z-1}^{ion+cx}(T) Q_z^{cx,n}(E_{nb})} \quad (2.19)$$

Because the excitation cross sections drop with n , the plume effect will especially affect the lower n transitions. The total CX rate decreases with beam voltage, while the specific CX rate into the n -shell of interest peaks at 20-50 keV/amu for the low- Z transitions in the visible. Therefore, the plume will especially be a concern for the often used $\text{He}^+(n=4-3)$ transition and for low beam voltages.

Fonck et al. [15] have also given a method to calculate approximately the line of sight integration and plume attenuation which is required to model the contribution to the plume spectrum from the corresponding sources in the beam and predicts a plume to prompt ratio of about 30% for PDX and TFTR for a 90keV/amu beam. This increases to about 70% for a 45keV/amu beam for a beam and l.o.s. geometry which are in the equatorial plane. If the line of sight is not tangential to the field lines (e.g. close to perpendicular) the plume component can be minimized. Gerstel et al. [20] have applied a Monte Carlo calculation to JET discharges to not only predict the plume intensity, but also the spectrum. The experimental data they compare to in [20] is limited to discharges with helium beams in which case a second beam plume contribution exists from single ionized beam injected helium. A full time dependent CR model has been developed to study the dynamics of highly ionized argon moving through a region in the plasma that is beam heated [40], but has not yet been applied to the specific case of the helium plume.

Experimentally, case studies of the plume effect are rare in literature despite the possible problems it can cause being acknowledged quite often. Curiously, Bell

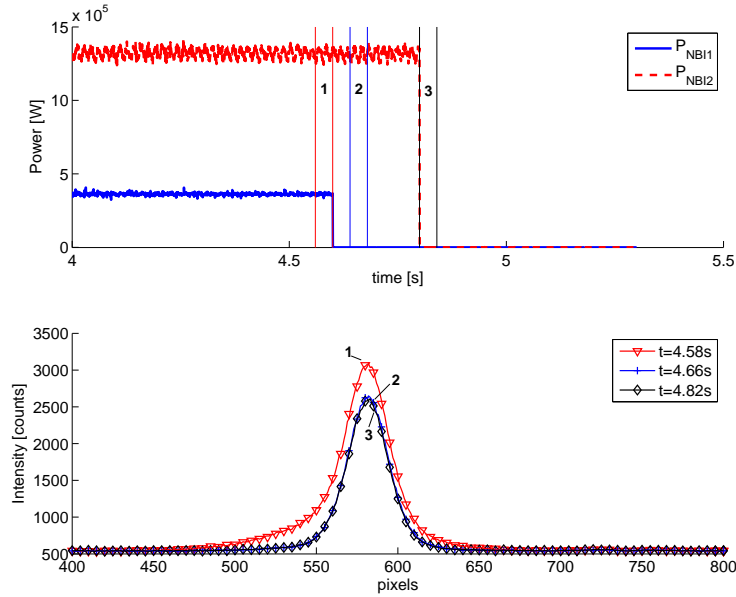


Figure 2.10: Helium plume experiment on TEXTOR (#103873): raw spectra of the 468nm line. The (equatorial) lines of sight intersect NBI1, but not NBI2. During the injection of full power NBI2, the same spectrum is measured as just after the injection. The width of the passive emission corresponds to 200eV. No sign of a plume is found. During the injection of NBI1 (360kW), the wings in the helium line are due to direct beam driven charge exchange and show the expected Doppler broadening and shift corresponding to the core ion temperature and rotation.

[41] has measured a plume on the 529nm C^{5+} line on lines of sight not intersecting the beams. The plume intensity reached about 20% of the ACX intensity on similar lines of sight intersecting the beam. The measured intensity was higher than what was expected from Fonck's model [15], but the radial profile was similar as the expected one. However, it is not entirely clear if the presented results could not have an alternative explanation as being caused by interactions between C^{6+} and the beam halo. A simple experiment on TEXTOR where we checked the existence of a helium plume is summarized in fig. 2.10. When NBI2 is fired into the plasma without NBI1, no plume signal could be detected on the equatorial lines of sight although from a geometrical point of view they are expected to be sensitive to the plume of NBI2.

It should be noted that, especially in the presence of beryllium such as on JET, the He II spectrum at 468nm can be complicated and it is not always possible to identify non-gaussian features such as a plume with certainty.

2.2.5 Fast ion charge exchange spectroscopy

The detection of fast ions using charge exchange spectroscopy is a natural extension of the now standard CXRS technique that is applied to measure the properties of the thermal ion population on many tokamaks. A thermalized ion population has a maxwellian velocity distribution and is thus characterized by 3 parameters: an ion temperature, a bulk rotation and a density. The projection on a line of sight of the Doppler shifted emission of a maxwellian ion population emitting monochromatic light gives a gaussian spectral line in which the ion temperature, rotation and density are encoded as the width, line shift and intensity of the line (see section 2.2.1). In the presence of a supra-thermal ion population, the same diagnostic technique can still be used but some complications arise.

First, a fast ion population in a tokamak will in general be anisotropic and the velocity distribution becomes two-dimensional (function of velocity parallel and perpendicular to the magnetic field, the velocity distribution is uniform in the third velocity coordinate, the gyro phase). Because only a projection on a line of sight is measured, there is a loss of information and the measured spectrum will depend on the geometry between the line of sight and the local magnetic field. ICRH accelerated ions mainly have a large perpendicular velocity and will be most easily detected with lines of sight perpendicular to the magnetic field. The clearest signature of beam injected ions will occur if the angle between l.o.s. and magnetic field is close to the initial pitch angle at which the fast ions are injected.

A second complication is related to the implicit assumption made above that each ion has the same probability to emit light. The charge exchange cross sections are energy dependent and hence the probability of an ion to undergo charge exchange with a beam neutral will depend on the collision velocity between the ion and the neutral atom from the beam. This means that the measured spectrum will be distorted by the geometry between the probing neutral beam and the fast ion velocity distribution. For thermal ions this gives rise to cross section effects which can be approximated analytically [32], but for fast ions this effect is much more important and one has to resort to forward numerical modelling of the spectral shape [31, 20, 42]. The effective CX emission rates from the ADAS database [24] for He^{2+} and H^+ are displayed in fig. 2.6. The emission rates strongly drop with energy and peak around 40keV/amu. This also puts a limit on the energy range of the ions that can be detected, especially the fast fusion born α 's can only be detected when they have already slowed down significantly. Or alternatively more energetic beams have to be used to detect faster α 's.

A third complication is that, unlike the thermal CX features, the fast ion generated spectrum is much broader in wavelength space and has a low spectral intensity. As a result the fast ion feature is easily buried under emission lines from impurity ions or obscured by the photon noise on the Bremsstrahlung continuum. Ways to mitigate this include fast modulation of the probing neutral beam, having passive lines of sight not intersecting the beam and modelling the spectral shape of the spectrum and fitting this to the data. The fast deuterium spectrum has the ad-

ditional complication that it can partially overlap with the beam emission spectrum.

Notwithstanding the above mentioned limitations, charge exchange spectroscopy has shown to be capable of detecting the slowing down spectrum of ^4He beam ions injected in JET [31] and fusion born helium at TFTR [43]. Recently the same diagnostic principle has been successfully applied to the notorious deuterium $n=3\rightarrow 2$ ($\text{D}\alpha$) CX spectrum at DIII-D [42, 44]. Both the detection of slowing down beam ions as well as ICRH accelerated ions [45] has been demonstrated on DIII-D using lines of sight that look perpendicular to the toroidal field. A diagnostic based on the same design has been installed on NSTX [46] and LHD [47]. The DIII-D diagnostic has been upgraded [48] to include lines of sight with a toroidal component and also 2D fast ion profiles have been measured using a relatively simple setup of a camera and a bandpass filter tuned to the wavelength range of interest [49].

We have investigated the possibility to obtain radial profiles of the fast ions injected by the neutral beams by combining the emission from the neutral beam itself and the fast ion charge exchange part of the spectrum. The development of this technique on TEXTOR and the difficulties that were encountered are described in section 4.2 of chapter 4 and the possibility for the detection of fast deuterium ion tails on JET is investigated in chapter 4, section 4.3. Chapter 4 also contains some example spectra and a method to simulate fast beam ion spectra.

2.3 Neutral beam attenuation

In order to convert the CX emissivities into local impurity densities using eq. 2.4, the local neutral beam fluxes are needed. But the importance of knowing the NB penetration goes far beyond measurements of the impurity densities. The neutral beams are the most important actuators for external heating and torque, non-inductive current drive and core plasma fuelling. For the modelling and interpretation of NB heated discharges, detailed knowledge is required about the fast ion deposition and hence of the heating and torque exerted upon the plasma. Also for basic machine protection, the neutral beam attenuation is needed for reliable shine-through models of the non-absorbed power deposited on the wall opposite to the beam.

If the beam power and the power distribution among the fractional energy components in the beam are known before the beam enters the plasma, the local beam densities can be calculated along the beam path using eq. 2.5. This calculation is implemented in commonly used analysis codes for NB heated discharges such as CHEAP, PENCIL and the NUBEAM package in TRANSP. The crucial parameters in this calculation are the plasma density and the effective beam stopping cross sections $\sigma_{stop}^E(\alpha)$. The main electron loss process for beam neutrals is charge exchange with bulk or impurity ions at energies below approximately 40keV/amu and ion impact ionization at higher energies. Stepwise ionization through excited states becomes increasingly important with plasma density and beam voltage and causes

a 20% increase of the beam stopping for JET-like beams (50keV/amu) and a 45% increase for the ITER heating beam operated at 500keV/amu. Because of the importance of the excited states, a full CR beam model is needed for the calculation of the beam stopping cross sections. A detailed discussion on the consistency of various CR models as well as on the key cross sections for proton impact ionization used therein can be found in sect. 3.3.3 in chapter 3. Therefore, we will here only show the results of the beam stopping modelling. Fig. 2.11 shows the voltage scaling of the ADAS beam stopping cross sections. There is only a weak dependence on Z_{eff} as the cross sections scale nearly linear in Z . The beam stopping drops fast as a function of beam voltage. A higher beam voltage ensures sufficient beam penetration to the core of large tokamaks, but over 50keV/amu the effective CX emission rates drop fast as well. For current tokamaks, the optimum beam energy for CXRS is close to 50keV/amu, while for the higher densities and larger dimensions of ITER the optimum for core CXRS on the diagnostic neutral beam is around 100keV/amu. The heating beams on ITER will be operated at 500keV/amu.

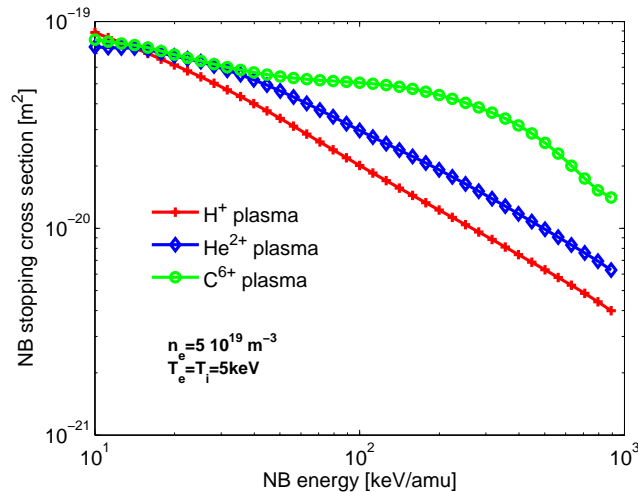


Figure 2.11: ADAS beam stopping cross sections as a function of beam energy for a pure H^+ , He^{2+} and C^{6+} plasma.

2.4 Beam emission and motional Stark effect spectroscopy

2.4.1 Overview

When the D_α beam emission spectrum (BES) was recorded for the first time and the motional Stark manifold was identified [50], one immediately realized the diagnostic potential of this spectrum.

The intensity of the beam emission spectrum directly relates to the excited population ($n=3$ or 4) in the beam from which the ground state density can be obtained.

Hence it was proposed to derive the local beam fluxes from BES, using eq. 2.6, instead of using a beam attenuation code. This eliminates the exponential error propagation due to uncertainties in the beam stopping cross sections and electron density as the beam is attenuated. It also has the advantage of reducing the need of an absolute calibration on CXRS to a relative calibration between several spectral bands [51, 52, 53]. This is the only feasible option to measure helium ash densities with the requested accuracy on ITER where only a small fraction of the beam power reaches the plasma center and where regular calibrations of the front optics will be impossible [54]. The use of beam emission as a beam density diagnostic will be treated in sect. 2.4.3.1. The main source of uncertainty in eq. 2.6 are the total H_α and H_β beam emission rates. These can be calculated using a CR model dedicated to the beam neutrals with a structure similar to eq. 2.9. A review on published beam emission rates with some corrections that had to be applied can be found in chapter 3 and the details will not be treated here. Often beam emission analysis cannot be performed on every shot. In that case beam emission (either by firing the beam into plasma or gas) is can still be used to characterise the beam (power fractions [55, 56, 57], alignment [58], divergence [55]) for use in attenuation codes. Section 2.4.3.2 specifically deals with beam in gas emission.

Apart from using the total intensity can the lines within the beam emission spectrum be used to obtain information about the magnetic field. The motional Stark effect (MSE) causes the beam emission line to split up into several lines with different polarizations as illustrated in fig. 2.12. The physics of the MSE diagnostic is discussed in sect. 2.4.4. Both the spectral splitting and line ratios [55, 59] can be used (sect. 2.4.4) as well as the polarization pattern [60] (sect. 2.4.4).

A prerequisite for obtaining any information out of the BES/MSE spectrum, is the fitting of a correct model to the experimental data, taking into account parasitic emission lines in the same wavelength range. The fitting algorithms used to fit the beam emission spectra throughout this thesis are described in section 2.4.2.

2.4.2 Fitting of the beam emission spectrum

On positive ion beams there are three energy fractions in the beam giving rise to 3 MSE manifolds of 9 observable lines each in the case of H_α beam emission (see fig. 2.12) and 10 observable lines in the case of H_β . If a line of sight crosses several beams, the corresponding MSE spectra will be blended, but can still be distinguished if the voltages or intersection angles are different. The beam emission feature also overlaps with background impurity lines, most notable for red-shifted beam emission is the C II Zeeman multiplet around 6579, and with the D I and H I active CX lines. Therefore it is not trivial to fit BES spectra in a way that is robust enough to allow the fitting of a large number of spectra without much user intervention. Luckily many parameters can be coupled, reducing the number of free parameters in the fit.

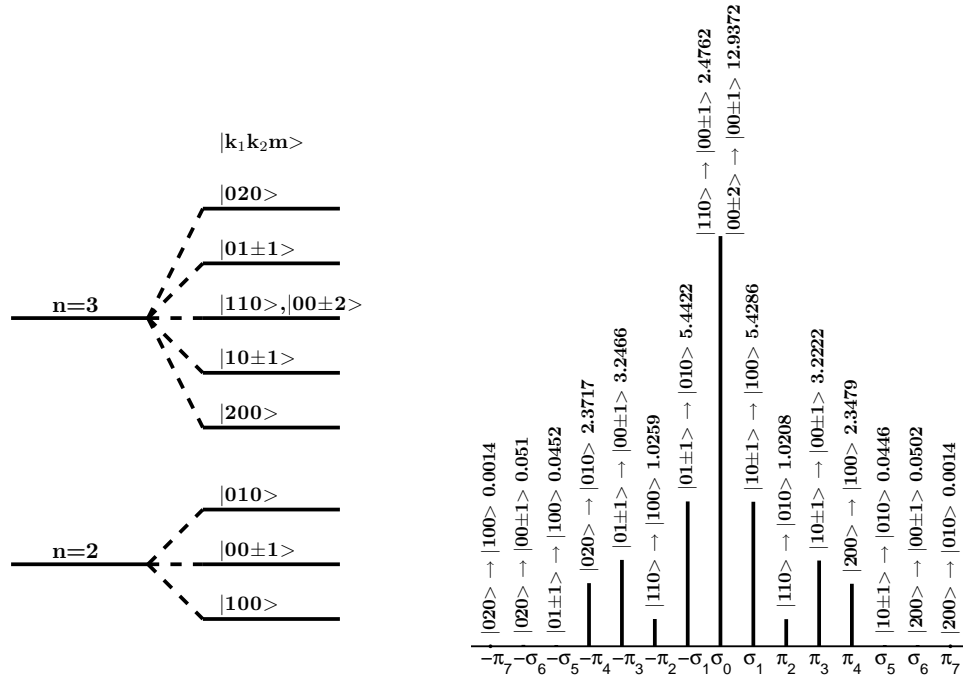


Figure 2.12: Motional Stark splitting of the $n=3$ and $n=2$ levels of hydrogen with the parabolic quantum numbers indicated. The resulting H_{α} spectrum is shown to the right with an identification of the lines. The relative intensities which are drawn correspond to a statistical population of $n=3$, and are integrated over all solid angles. The A-values [10^7 s^{-1}] have been calculated using the methodology of [29], for an electric field of 10^7 V/m . When there are two negative or positive m -levels in a transition, the sign of the m -level is preserved, the given A-value then corresponds to the sum of the two transitions.

A beam emission fitting code, called BESFIT, has been developed that allows the user to easily couple or fix parameters to user defined initial estimates or to externally loaded data. Models are included for D_{α} and D_{β} beam emission in plasma or gas. The settings can be stored as a 'recipe' that can then be applied to process a full shot as a batch job, once a stable algorithm is found. This approach is inspired by CXSFIT ([23], maintained by ADAS), but due to the more difficult parameter coupling scheme the flexible IDL minimisation routine MPFIT [61] has been used here instead of the more efficient, but computationally more complex, implementation of CXSFIT. Several other options borrowed from CXSFIT are the automatic detection of active frames and beams contributing to the spectrum and the use of previous frame estimates as well as the truncation of gaussians after a number of standard deviations to increase computation speed.

The line shape of a single MSE line, representing the projection of the energy distribution within the NB on a line of sight, is determined from a beam in gas shot

without magnetic field. For shots with magnetic field, a second distortion of the line shape can occur due to the variation of the Lorentz field along a line of sight. It is found that on JET the line shape can still be approximated well enough by a single gaussian with increasing width if the beam energy increases. Because such a beam in gas shot is only available at specific voltages, this width is in practice only used as an initial estimate. On tokamaks where the beam is broad with regard to the plasma minor radius, as on TEXTOR, the geometric effects of Doppler shifts and Stark splitting along a line of sight will give rise to an asymmetric MSE line shape, and hence to an apparent asymmetry between $I_{+\pi}$ and $I_{-\pi}$. An analytical method to take these effects into account is described in [62] and a simulation code of the MSE line shape is described in [63]. Any line shape that can be easily calculated or approximated with a simple function only depending on a small number of free parameters could easily be implemented in BESFIT, but up to now, no line shapes other than gaussians have been necessary.

The instrument function in BESFIT is approximated by a sum of gaussians, this allows for easy convolution. The relative intensities and spacing of lines within the 658nm C II multiplet are taken from ADAS, leaving only the (edge) magnetic field, line width and overall intensity as free parameters.

The most stable recipe to analyse the beam emission intensity is to couple the ion temperature and rotation of the D I and H I CX lines to each other and to set the intensity ratio between them equal to the $H/(H+D)$ ratio measured at the edge of the plasma by the dedicated diagnostic. The deuterium ion temperature and rotation can be left free in the fit but the stability of the fit is increased when initial estimates are taken from the C VI CX line. Alternatively, one could fix the temperatures to C VI and leave the $H/(H+D)$ ratio free, but this was found to be unstable at typical JET hydrogen concentrations below 10% and results from TEXTOR at higher $H/(H+D)$ are still in doubt as the CX line shape from H and D can be strongly distorted by cross section effects. The ion temperature and rotation from the deuterium charge exchange line on JET agreed rather well with the C VI ion temperature, even if the latter was not used as initial estimate, but no extensive comparison has been made. The coldest part of the unshifted H/D-line is removed from the minimization as this part is usually overexposed and to reduce the influence an inexact representation could have on the rest of the fit. The Stark feature is assumed symmetric, but the line ratios within the σ - and π -groups are left free. In fig. 3.6 in chapter 3 an example of a fitted D_α beam emission spectrum is shown and fig. 3.7 shows a typical D_β spectrum. The D_β spectrum has a 20-fold lower intensity and needed to be averaged in time to obtain sufficient signal.

In the current implementation of BESFIT the line ratios within the σ - and π -groups on different beams and energy components is coupled. Leaving this free would induce too many free parameters and cause unstable fitting. For the results on the MSE line ratios shown in fig. 3.12 and 3.13, a single beam was used and the weights on the spectrum were reduced except for the E/1 component.

2.4.3 Beam emission as a neutral beam diagnostic

2.4.3.1 Beam in plasma emission

The use of beam emission intensities to obtain the neutral beam density profiles was recognized early on as a check on the beam stopping calculations. This topic is reviewed in detail in chapter 3, where it is shown that current agreement between expected and measured beam densities is overall satisfactory. CR modelling with Stark level resolution has been undertaken for better interpretation of the MSE multiplet, but only at densities lower than those encountered in tokamak plasmas will there be a deviation on the total emissivity from $n=3$. Time dependent modelling can be necessary in regions of the plasma where there is a strong density gradient: at 50keV/amu the NB travels about 2cm before the $n=3$ population reaches steady state.

A logical extension of measuring the beam densities is to provide an in situ check on the NB power fractions [55, 57]. The power fractions measured with BES have been compared with the expected beam densities (from measurements on the partially neutralised beam in the JET NB testbed) during a voltage scan. The results are compared in table 2.1, using the updated beam emission rates. The results are also plotted and discussed in chapter 3, fig. 3.11(a) and sect. 3.4.2. The agreement is very good, which gives some confidence in the voltage scaling of the beam emission rates.

shot	V [kV]	E/1 ppf	E/2 ppf	E/3 ppf	E/1 bes	E/2 bes	E/3 bes
75050	78.9	0.706	0.112	0.181	0.690	0.147	0.163
75048	89.1	0.715	0.127	0.158	0.709	0.157	0.133
75047	99.3	0.726	0.139	0.134	0.716	0.172	0.111
75046	111.4	0.742	0.150	0.107	0.721	0.186	0.092

Table 2.1: Power fractions based on testbed measurements and from beam in plasma emission for a voltage scan (pini 8.7). This data is plotted in fig. 3.11(a)

Another, in practice very useful, application of beam emission spectroscopy is the characterisation of the l.o.s. geometry by the known beam voltage and measured Doppler shift of the BES components. See e.g. [58] for an application on JET. This is also the method applied on TEXTOR.

2.4.3.2 Beam in gas emission

The practical importance of beam into gas emission for fusion devices is primarily the determination of the NB power fractions using the intensity ratios of the emission from each energy component and the calibration of the MSE diagnostic with the known vacuum field.

The NB power fractions can be obtained from beam in gas emission on the neutralized beam from which the ions have been removed and from beam emission on the partially neutralized beam, as it is usually done on NB test stands. In any case, for measuring the power fractions, the voltage scaling of the beam into gas emission rates is needed. The experimentally obtained beam into gas emission rates from [64] (in the coronal limit) are the only source of atomic data currently available for the interpretation of the beam emission intensity from H and H⁺ collisions with H₂. When measuring on a mixed beam of ions and neutrals, it requires extensive modelling to obtain the power fractions of the neutrals. The procedures are described in [65, 66]⁴. In this case, most of the measured light comes from the ions undergoing charge exchange and these cross sections are known to relatively good accuracy (experimentally easily accessible). Hence this method can be considered a reliable technique to measure the power fractions of the ions in the beam, which can then be modelled towards the neutral beam power fractions. Directly measuring the power fractions on the neutral beam using the H+H₂ Balmer- α emission rates is conceptually easier, but the cross sections have larger error bars. Fig. 2.13(a) shows the emission cross sections as a function of voltage and fig. 2.13(b) shows a typical beam emission spectrum from JET when the toroidal magnetic field is switched on. When taking into account the error bars, one finds a 1σ -uncertainty on the E/1 power fraction of about 10% of the total beam power using this method, but especially between 20 and 50 keV/amu the uncertainty could be larger due to the steep slope in the cross sections and the large error bars on these few points.

The power fractions from beam in gas emission in the JET vessel and the expected power fractions based on an analysis involving beam emission data from the JET NB Testbed are compared in table 2.2. This data is plotted in fig. 3.11(b). For the highest and lowest beam voltage the agreement is nearly perfect, while for the 80-100kV range there is still a slight deviation, probably due to the inaccuracy of the H+H₂ Balmer- α emission rates.

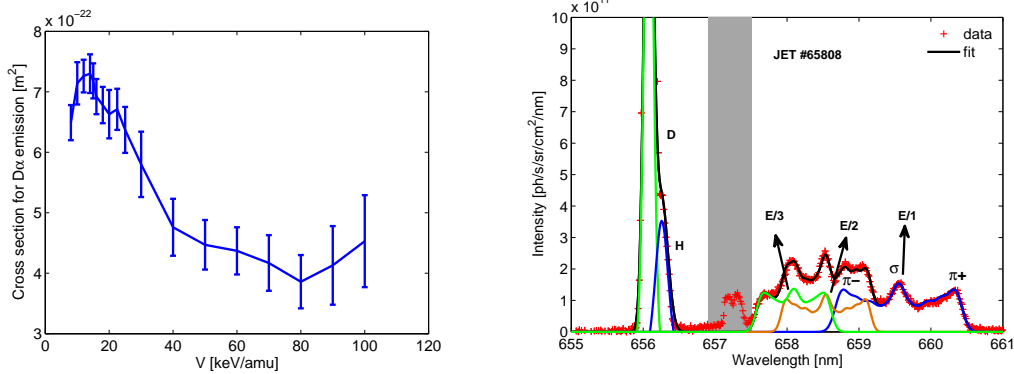
For the calibration of MSE diagnostics one can use the known vacuum field during a beam into gas shot. However, the relative intensities of the lines within the MSE multiplet are substantially different compared to beam in plasma emission. This can have severe effects on the reliability of the calibration. For polarization based MSE, the amount of sampled σ - and π - light will depend on the n=3 population structure in case σ - and π - components overlap in the sampled wavelength region. Intensity ratio based MSE will even be more dependent on the n=3 sublevel equilibrium in case only the total intensity ratio Φ_{σ}/Φ_{π} can be measured and not the more difficult to resolve $\Phi_{\sigma 1}/\Phi_{\pi 3}$ ratio.

The non-statistical character of the n=3 line ratios can clearly be seen compar-

⁴A correction to the analysis in [65, 66] should be applied, as particle densities and fluxes are mixed up in the formulas leading to the interpretation of the observed photon flux. Any reference to corrected jetppf power fractions in this work means that this corrections has been applied.

shot	V [kV]	E/1 ppf	E/2 ppf	E/3 ppf	E/1 bes	E/2 bes	E/3 bes
77532	69.0	0.699	0.097	0.204	0.725	0.095	0.181
77531	79.1	0.706	0.112	0.181	0.763	0.105	0.132
77530	89.2	0.715	0.127	0.158	0.770	0.133	0.097
77528	99.1	0.726	0.139	0.134	0.773	0.116	0.111
77529	99.2	0.726	0.139	0.135	0.771	0.131	0.098
77533	109.1	0.739	0.149	0.112	0.758	0.153	0.089
77534	114.1	0.747	0.153	0.100	0.746	0.163	0.091

Table 2.2: Power fractions from the corrected testbed based analysis and from beam in gas emission for a voltage scan (pini 8.6) on JET. This data is plotted in fig. 3.11(b)



(a) Experimentally determined cross sections for H α emission of the H projectile in H₂+H collisions from [64]. The voltage scaling of these cross sections is often used to determine the NB power fractions from beam in gas emission. The large error bars can induce considerable uncertainty.

(b) Fitted beam into gas emission spectrum from JET #65808. The grey area is not taken into account in the fit. The deviation from a statistical population of the n=3 subpopulation is mostly clearly visible in the increased overall π -emissivity and increased π_4/π_3 ratio compared to beam in plasma emission (fig. 3.6) or the synthetic spectrum shown in fig. 2.12.

Figure 2.13: Cross sections and example spectrum for beam in gas emission.

ing fig. 2.13(b) and fig. 3.6 which show beam in gas and beam in plasma emission spectra from JET. The intensity of the π group is clearly higher than the σ group intensity, which is typically observed when the target density is not high enough to equally populate the n=3 sublevels. Table 2.3 lists the observed line ratios and total intensity ratios observed on a beam in gas and plasma discharge on JET. The strong deviation with the statistical ratios is clear and results in the observation of a lower Φ_σ/Φ_π . This provides a possible explanation for difficulties in the calibration of MSE diagnostics using beam in gas emission. Other effects such as ionized beam neutrals that undergo charge exchange within the line of sight might also play a role, but we have not been able to observe this on MSE spectra from JET and it is very weak on TEXTOR beam in gas spectra.

	in gas #65808	in plasma #76763	statistical
σ_1/σ_0	0.429	≈ 0.41	0.353
π_2/π_3	0.893	≈ 0.35	0.314
π_4/π_3	1.448	≈ 0.81	0.728
$\sum \sigma / \sum \pi$	0.454	≈ 0.7	$\frac{1+\cos^2(\theta)}{\sin^2(\theta)} (\geq 1)$
$\sigma_1 A_{\pi 3} / \pi_3 A_{\sigma 1}$	0.418	≈ 0.42	$\frac{1+\cos^2(\theta)}{2 \sin^2(\theta)} (\geq 0.5)$

Table 2.3: Stark line ratios for beam in plasma and gas from JET.

The MSE line ratios during beam in gas discharges have been modelled for the interpretation of MSE diagnostic calibrations as well as for more fundamental understanding.

Foley et al. [67] has modelled the sublevel population of a neutral hydrogen beam travelling through H₂ gas taking all sublevels up to n=3 into account. The full hamiltonian (fine structure, (motional) Stark and Zeeman terms) is retained in the determination of the eigenstates of the system. Unfortunately, the published results are restricted to very low values of the magnetic and motional Stark field. At tokamak conditions the motional Stark field is by far dominant, and higher n-states are important as well.

Gu [68] has extended his beam into plasma modelling to beam into gas by changing the potential in the cross section calculations. The main result is that a statistical population distribution is reached at higher density than in plasma and therefore the I_π over I_σ ratio is higher. The correction of Gu's model was not enough to reach consistency with measurements of the polarisation pattern on DIII-D [68], but this is a rather indirect check on the atomic modelling and the remaining inconsistency was at least partially attributed to contamination by other sources of polarized light.

Another possible application of beam in gas spectroscopy is the calibration of the polarization sensitivity of the entrance optics of an intensity ratio based MSE diagnostic. From the known direction of the vacuum magnetic field and the l.o.s. versus beam alignment, one can derive an approximate correction for the different transmission of the σ - and π -emission using the measured intensity ratio $\Phi_{\sigma 1}/\Phi_{\pi 3}$ which is not distorted by atomic physics effects.

2.4.4 The Motional Stark effect diagnostic

The characteristic substructure of the D _{α} beam emission multiplet due to the motional Stark effect (MSE) splitting of the degenerate n=3 state has been exploited much more intensively than the total intensity of the multiplet itself. The MSE diagnostic is the sole diagnostic that can provide localized information on the internal magnetic field in the plasma core from the line splitting, intensity ratio and direction of polarization of the MSE lines. The MSE measurements do not directly

relate to one of the components of the magnetic field vector, but can effectively be used to constrain the possible magnetic field topologies generated by a magnetic field reconstruction code such as EFIT.

From a diagnostic point of view, for the line splitting and intensity ratio between σ - and π -lines one needs to measure the full spectrum at high spectral resolution, while for polarization based MSE a narrow bandpass filter is used to select a single σ - or π -line of which the direction of polarization needs to be measured.

Spectral MSE: line splitting based

The use of MSE splitting as a magnetic field diagnostic has first been recognised on JET [55, 59]. The Stark splitting is proportional to the Lorentz field and hence yields a measure for the magnetic field component perpendicular to the neutral beam. Because the toroidal field is usually an order of magnitude larger than the poloidal field and the beams have to be injected near perpendicular, it is on current tokamaks not possible to obtain the Stark splitting with sufficient accuracy to obtain information on the poloidal field. The most successful application of line splitting based MSE is the measurement of the plasma diamagnetism as a diagnostic for the thermal and perpendicular fast ion pressure profiles [59].

In case of a high beam voltage combined with a high magnetic field, both the Stark splitting and the spectral intensity are increased, opening the possibility of current profile reconstructions from line splitting based MSE. Because polarization based MSE will be impossible on ITER due to degradation of the front optics, a line splitting based MSE diagnostic looking in the equatorial plane to the heating beams is proposed as the standard MSE diagnostic on ITER [69]. Simulations of the MSE spectrum from the ITER heating beams show that sufficient accuracy can be achieved [69].

Spectral MSE: line ratio based

The angular dependence of the σ - and π -emission can be used to obtain one constraint on the direction of the Lorentz field and hence on the direction of the local magnetic field. Just as for line splitting based MSE described above, the full spectrum needs to be measured and resolved. If the σ_1 - and π_3 -lines can be resolved, the intensity ratio of these two lines directly relates to the angle θ between l.o.s. and Lorentz field. One only needs to account for the branching ratio and the possible difference in sensitivity of the entrance optics to both polarizations ($T_{\sigma\pi}$), which is a weak function of θ itself, but for small changes in pitch angle this can be neglected or taken into account analytically in the assumption that the first mirror is the most important element reducing the reflectivity of p-polarized waves over s-polarized waves⁵. The polarization sensitivity can be obtained from discharges in which the

⁵In the assumption of pure Motional Stark emission and only taking the first mirror into account:

$\mathbf{1}_n$: unity vector normal to the first mirror

$\mathbf{1}_{\sigma,\pi}$: unity vector along direction of polarization

magnetic field is known, such as beam in gas discharges. The non-statistical $n=3$ population (see sect. 2.4.3.2) is not a concern when the σ_1 - and π_3 -lines can be resolved.

$$\frac{\Phi_{\sigma_1}}{\Phi_{\pi_3}} = \frac{1 + \cos^2(\theta)}{2 \sin^2(\theta)} \frac{A_{\sigma_1} T_{\sigma\pi}}{A_{\pi_3}} \quad (2.20)$$

In case only the total σ - and π -emission can be resolved with sufficient accuracy, as it is the case on most tokamaks, eq. 2.21 needs to be used, which contains apart from $T_{\sigma\pi}$ also a term $\alpha_{\sigma\pi}$ which corrects for the non-statistical population of $n=3$. For tokamak plasmas and positive ion beams, $\alpha_{\sigma\pi}$ is typically 0.85 and depends mainly on beam voltage and electron density. A CR-model can be used to predict the $n=3$ Stark level populations [50, 68, 70]. In chapter 3, the model of Marchuk et al. [70] is compared to the total measured σ to π ratio, the first mirror and theta dependence being corrected for by using the σ_1 to π_3 ratio again. The agreement is very well. In practical situations, $T_{\sigma\pi}$ could be determined using a beam into gas shot at highest possible field and beam voltage from the σ_1 and π_3 lines or alternatively from an in-vessel calibration using a polarized light source. The total σ - to π - emissivity, which can be determined at higher statistical accuracy, can then be used in tokamak experiments in combination with a modelled $\alpha_{\sigma\pi}$.

$$\frac{\Phi_{\sigma}}{\Phi_{\pi}} = \frac{1 + \cos^2(\theta)}{\sin^2(\theta)} \alpha_{\sigma\pi} T_{\sigma\pi} \quad (2.21)$$

One of the major drawbacks of line ratio based MSE is that the sensitivity of the measurements to changes in θ is very low for θ close to 0° or 90° , which are the most common geometries for spectrometer lines of sight aligned to a neutral beam. This is probably the reason, apart from the assumption of a statistical population, that the first attempt of line ratio based MSE was rather unsuccessful on JET [55]. This can partially be mitigated by inserting a tilted polarizer in the entrance optics [71], but ideally the lines of sight have an angle with the toroidal field of approximately 45° . Larger sensitivity under this geometry has been demonstrated at TEXTOR [54], but the effect of the first mirror, combined with the badly resolved multiplet, made measurements difficult. Recently, on DIII-D, a line based MSE diagnostic with favorable viewing geometry is taken into operation [72, 73], based on the use of the σ_1 - and π_3 -lines. The modelling of the MSE line shape is the most crucial element determining the accuracy of the measurements.

Line ratio based MSE has been proposed to be used on the ITER DNB as supplementary information to be extracted from the beam emission channel of the core

R_{sp} : ratio between s- and p-reflectivity of the first mirror

The σ_1 to π_3 ratio becomes:

$$\frac{\Phi_{\sigma_1}(\theta)}{\Phi_{\pi_3}(\theta)} = \frac{A_{\sigma_1}}{A_{\pi_3}} \frac{1 + \cos^2(\theta)}{2 \sin^2(\theta)} \sqrt{\frac{R_{sp}^2 (1 - (\mathbf{1}_\sigma(\theta) \cdot \mathbf{1}_n)^2) + (\mathbf{1}_\sigma(\theta) \cdot \mathbf{1}_n)^2}{R_{sp}^2 (1 - (\mathbf{1}_\pi(\theta) \cdot \mathbf{1}_n)^2) + (\mathbf{1}_\pi(\theta) \cdot \mathbf{1}_n)^2}}$$

Or, alternatively, if the magnetic field (and hence θ) is known, R_{sp} can be derived:

$$m = \frac{\Phi_{\sigma_1}(\theta)}{\Phi_{\pi_3}(\theta)} \frac{A_{\pi_3}}{A_{\sigma_1}} \frac{2 \sin^2(\theta)}{1 + \cos^2(\theta)}$$

$$R_{sp} = \sqrt{\frac{-(\mathbf{1}_\sigma(\theta) \cdot \mathbf{1}_n)^2 + m^2 (\mathbf{1}_\pi(\theta) \cdot \mathbf{1}_n)^2}{(1 - (\mathbf{1}_\sigma(\theta) \cdot \mathbf{1}_n)^2) - m^2 (1 - (\mathbf{1}_\pi(\theta) \cdot \mathbf{1}_n)^2)}}$$

CXRS spectrometers [74]. The viewing geometry, from one of the upper ports, is favorable as well as the high Lorentz field due to near perpendicular injection of a 100keV/amu beam in a 5T plasma. The line shape however is not known yet and will depend on the design of the beam which is still ongoing.

Polarization based MSE

The classical polarization based MSE diagnostic [60] measures the direction of polarization in a plane perpendicular to the line of sight of either one of the σ (polarized $\perp \mathbf{E}_L$) or π (polarized $// \mathbf{E}_L$) components. In most applications the data is used to constrain the reconstruction of the internal magnetic field. Because the direction of polarization is the quantity of interest, the diagnostic hardware is conceptually very different from the spectral based MSE approach.

The original MSE polarimeter [75] consists of 2 photoelastic modulators (PEMs) with their axes tilted over 45° followed by a polarization filter which has its axis rotated to the middle of the 2 PEM axes. A PEM consists of a birefringent crystal attached to a piezoelectric transducer which modulates the refractive indices in the plane of the PEM at the resonant frequency of the crystal. This induces a time modulated phase shift between the light polarized along and perpendicular to the PEM axis. Only the component of the light polarized along the axis of the polarization filter will be transmitted to the detector. The angle between the polarization of the incoming light and the axis of the PEM will be encoded in the amplitude of the signal oscillating at even harmonics of the PEM driving frequency. The use of 2 PEMs at different frequencies allows to identify this angle from the amplitude ratio of the measured oscillations at both frequencies. Because the properties of optical elements affect the polarization of light, the polarimeters have to be mounted in the periscope attached to the tokamak vessel. The bandpass filter and detector can be placed outside, using optical fibers to guide the light. The bandpass filter can be tilted to tune the selected wavelength ratio such that the Doppler shift matches the beam voltage and Stark splitting.

The use of a bandpass filter avoids the use of a grating based spectrometer, which would reduce the signal intensity and hence the time resolution, but this comes at the cost of reduced information on the spectral purity of the region selected by the bandpass filter. A diagnostic combining the spectral information with the polarization direction is possible when using a polarization beamsplitter (Glan Thompson prism) and reading out the spectra of both polarizations separately [76, 77], but this has not been applied yet as a routine MSE diagnostic.

The calibration of a MSE polarimeter is difficult. One could use a polarized light source to irradiate each line of sight from within the vessel, but this is often either not achievable due to restricted access or the results could not be brought into consistency with measurements on plasma discharges. In practice, discharges are used in which the magnetic reconstruction is reliably known or beam into gas discharges in which the magnetic field reduces to the vacuum field. When the MSE line width

is relatively large with regard to the Stark splitting, it becomes increasingly difficult to select only σ - or π -emission with a bandpass filter. Partially sampling emission from the other polarization group is often unavoidable. As shown in chapter 3, the $n=3$ level has not reached a statistical distribution and yet and this results in a higher π/σ ratio. In case of overlap of components in the sampled wavelength range, variation in n_e and V_b will change the amount of π - and σ -light which is sampled and the emission from unwanted Stark components should be accounted for in the data analysis by use of a CR model [70], although the effect is partially cancelled by the calibration in case a beam in plasma discharge is used at the same beam voltage and electron density as in the experiment. The effect will especially be important for beam in gas calibrations as the $n=3$ subpopulation is far away from statistical equilibrium (see sect. 2.4.3.2). The CR model by Gu et al. [68] provides the $n=3$ subpopulation, relevant for beam in gas calibration discharges. An additional disturbance of beam in gas calibrations can be caused by charge exchange reneutralization of the ions injected by the beam, circulating in the torus [78].

Other sources of polarized light in the sampled wavelength range can be a major concern for MSE. During beam in plasma experiments, there can be emission from fast ions that undergo charge exchange and also experience a motional Stark effect and black body radiation and Bremsstrahlung. The latter two are in principle not polarized, but reflections, for instance on a metallic first wall can provide a net polarized observed radiance.

Polarization based MSE will not be possible in the DT-phase of ITER, because optical labyrinths need to be used to provide sufficient neutron shielding. These will scramble the original polarization in a way that could vary over time as layers may be deposited on the first mirror. Line splitting based MSE is foreseen on the heating beam and additionally line ratio based MSE could be used on the DNB.

2.5 Active hydrogen beam spectroscopy on TEXTOR

2.5.1 Introduction

In this section we will describe the experimental setup of the TEXTOR CXS diagnostic, for completeness on this introductory chapter on CXS spectroscopy and for later reference from chapters 4 and 5, where this setup has been used for fast ion measurements and validation of the helium CXS/BES concentration analysis.

2.5.2 CXS periscopes and lines of sight

TEXTOR has three neutral beams that can be operated on hydrogen or deuterium (see fig. 2.14). There is one diagnostic beam and there are two heating beams of the JET pini type [79] with a maximum operation voltage of 55keV. A complete description of the charge exchange diagnostic on the diagnostic beam can be found

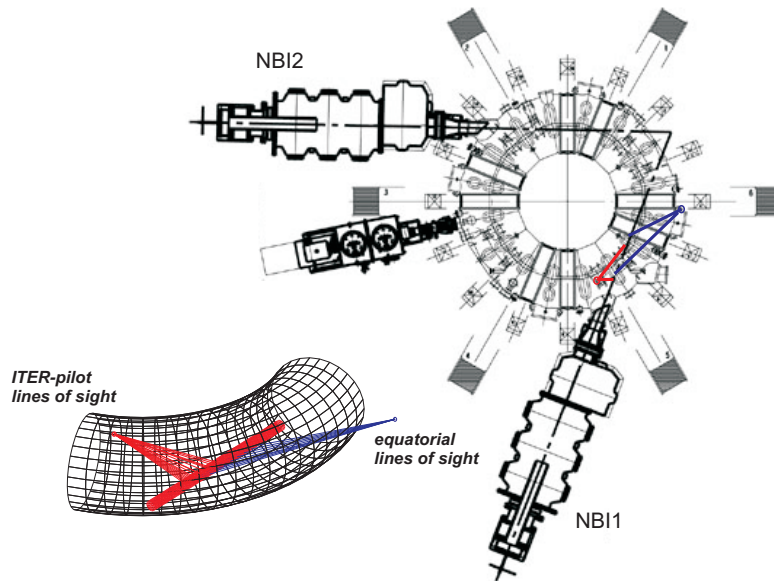


Figure 2.14: Overview of NB injection on TEXTOR with the equatorial and ITER-pilot CXS viewing geometries on NBI1 indicated.

in [80]. The heating beam based diagnostics have all been installed on NBI1, which is in standard configuration injected co- I_p /counter- B_t , and started with a single line of sight looking from the top. This was later extended to a viewing fan with two times 9 active and 1 passive line of sight in the equatorial plane and an edge CXS fiber array (see e.g. [81]) which is not longer in operation. A spectral MSE diagnostic has been installed looking to NBI1 along the direction of injection of the beam [76, 82], but the fibers from this diagnostic have now been removed.

During the preparation of this thesis, two new periscopes have been installed. One having two arrays of 22 fibers looking to NBI1 under an angle of approximately 35° with the equatorial plane. This is a similar viewing geometry as the one that will be used on the ITER diagnostic beam and therefore this set of fibers has been called ITER-pilot [74]. This diagnostic was mainly aimed at clarifying some of the CX diagnostic issues for ITER, such as the use of beam emission to cross calibrate CX data and the modelling of the helium plume. In contrast with the lines of sight in the equatorial plane, the periscope can be retracted to prevent coatings to form on the optical elements, e.g. during boronizations. The fibers can easily be removed from the periscope for calibration purposes. The second periscope which has recently been installed, has 72 fibers in a single array and is looking in the equatorial plane to NBI2. No data along these l.o.s. has been collected so far, but these fibers will be used to test the performance of a prototype spectrometer for the ITER core CX diagnostic under real tokamak conditions.

For routine use, only fibers from the two viewing geometries shown in fig. 2.14 are currently being used. The equatorial fibers span a radial range from 1.72 to 2.00m. The ITER-pilot fibers have a radial range from 1.86 to 2.11m. The radial resolution of the two viewing geometries, determined by the NB density distribution along each line of sight, is shown in fig. 2.15. The ITER pilot or top view lines of sight have a much better spatial resolution than the equatorial ones as they are tangential to the flux surfaces at the intersection with the beam, but they only observe the low field side of the plasma.

MSE and CXS imaging proof of principle experiments have been performed on TEXTOR [83, 84], using the observation port of the former MSE diagnostic.

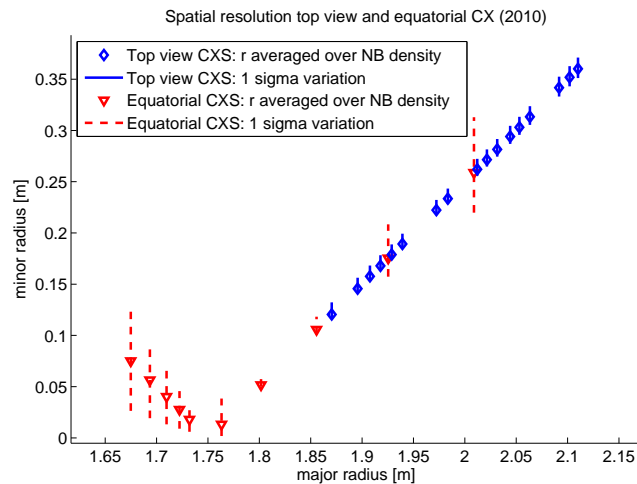


Figure 2.15: Radial resolution of the CXS lines of sight on TEXTOR (as in the 2009-2010 campaigns), obtained from the NB density distribution along each line of sight.

2.5.3 Spectrometers and ccd cameras

Four spectrometers are available for active beam spectroscopy on TEXTOR, three Littrow type spectrometers and one modified Pfund spectrometer, designed by the TRINITY institute (see fig. 4.1 for a sketch of the optical scheme). The TRINITY spectrometer has been installed during the preparation of this thesis and combines a relatively high optical throughput with high spectral resolution and has been used for the fast ion measurements of chapter 4 and the helium experiment of chapter 5. The TRINITY spectrometer is read out with a Roper Scientific PIXIS 400B (1340×400) ccd camera which has a high quantum efficiency and low read-out noise, but has no frame transfer capabilities. Therefore a shutter needs to be used to avoid smearing during read out. This reduces the time resolution of this ccd to 80ms using the fastest settings and hardware binning on each radial channel. A wavelength range of about 9nm can be recorded which allows measurements of broad features. Two spectrometers are read out with Jonathan Wright ccd cameras and one spectrometer is read out with a Pluto camera from Pixelvision. The time resolution on these

spectrometers is usually set to 50ms. The Pixelvision camera can be read out faster, but the signal to noise ratio becomes too low due to poor photon statistics. The ccds are triggered externally by pulses from the TEXTOR JDAQ data acquisition system.

A prototype spectrometer for ITER is currently being built and will in a first phase be installed on TEXTOR. This spectrometer has a much higher optical throughput and allows measurement of the He II 468nm, C VI 529nm and D_α wavelength bands along the same lines of sight.

2.5.4 Calibration

The wavelength calibration is performed using the very well known natural wavelengths [85] of the Ne I or Ar I emission lines of a gas discharge lamp. There are several suitable lines in the vicinity of each of the relevant CXS lines. For the ITER-pilot setup, the lamp can be placed in front of the fibers at the TEXTOR side, but for the equatorial fibers, the fiberhead is illuminated from the spectrometer side and the emission that is backscattered in the cladding of the fibers is used to measure the dispersion and the central wavelength on the ccd chip. The dispersion is easily measured with sufficient accuracy and is assumed constant over the length of the ccd chip. The accuracy of the derived plasma rotation and the validity of the spectral fit as a whole mainly depend on the accuracy of the calibrated position of the natural wavelength of the CX line. A drift up to 1.5px during a day has been observed due to thermal expansion of the mechanical structure of the spectrometer or changes in humidity of the air. One option is to compute this so-called 'pixel reference' from the measured position of a nearby Ne I line from a fresh calibration. The second option is to use an intrinsic impurity line that can be assumed to be not rotating, e.g. emission from a lower ionisation stage during the ohmic phase of a discharge. Fig. 2.16 shows rotation profiles from C VI-CX measured with two spectrometers, one with a fresh Ne I pixel reference and one using the C III line at 530.462nm. Good consistency is found.

The instrument function is measured as being the line shape of a Ne I line as the intrinsic linewidth and Doppler broadening of the lines from the neon discharge lamp are much narrower than the instrument function of the spectrometers at the slit widths used for active beam spectroscopy. The instrument function is approximated as the sum of three gaussians for easy deconvolution in the analysis software. The intensity calibration is performed with a tungsten lamp supplied with an accurate current source and attached to an integrating sphere giving an absolutely calibrated spectral radiance [by LabSphere]. When only T_i and Ω_ϕ or relative intensities are of interest, the intensity calibration is not important, except for the TRINITY spectrometer where a bandpass filter is used and hence the calibration varies over the length of the ccd chip. Only the ITER-pilot lines of sight have been calibrated as these fibers are readily removed from the periscope, the last mirror, window and lenses have been calibrated separately from inside the vessel during an opening.

The radial positions of the observation volumes have been determined using the known beam and observation port coordinates and the Doppler shifts from beam emission. For the ITER-pilot l.o.s., it is assumed that the lines of sight cross the center of the beam as intended by the design. This has been checked to agree reasonably with the variation of the beam emission intensity along two arrays of fibers that are perpendicular to the lines of sight that are aligned along the beam axis. The radial resolution is determined by the intersection length between the l.o.s. and the neutral beam. Assuming a gaussian beam with a 1σ width of 0.11m, the ITER-pilot 1σ resolution for the fibers nearest to the core is approximately 5cm and reduces to 2cm for the l.o.s. most towards the edge. The equatorial lines of sight have a worse radial resolution, near the edge about 7cm and approximately 4cm in the core.

2.5.5 Data acquisition and analysis

The data is read out from the ccd cameras to a local data acquisition PC and uploaded to the Central Storage Facility awaiting analysis. The data can be accessed via the TEC Web Umbrella⁶ (TWU) [86]. The geometry information, wavelength and intensity calibration are also accessible on the TWU via a redirection scheme. The redirections are managed via a CVS controlled file on the TEC code server. Reshuffling the order of tracks is also done via redirection on the TWU as this is also shotnumber dependent.

Charge exchange data is fitted with CXSFIT (see sect. 2.2.2 and [23]). The active D_α data used in this thesis is either analysed with BESFIT (see sect. 2.4.2) or with custom codes because CXSFIT is not able to cope with Zeeman and Stark features. The dark current on the spectra is subtracted as being the average of the last frames after the shot. Poisson noise on the photo-electrons is assumed to determine the error bar on each pixel.

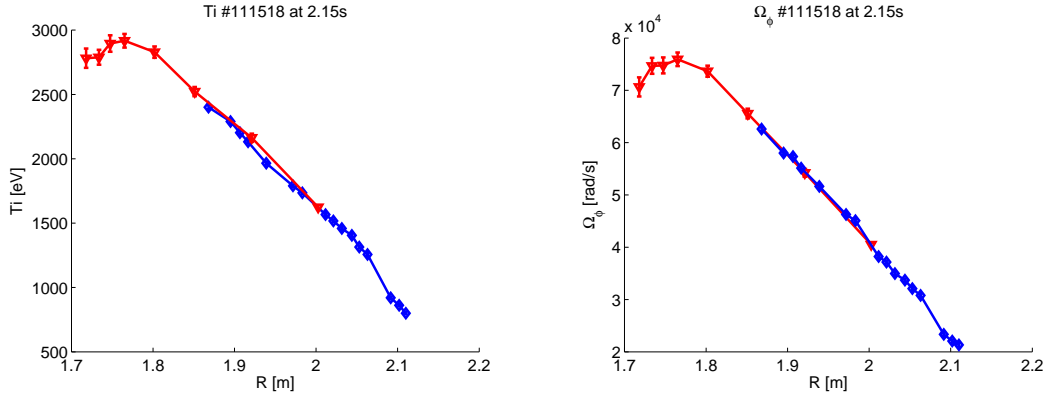
The output of CXSFIT (T_i , Ω_ϕ , I_{cx}) is uploaded to the TEXTOR Physics Database⁷ (TPD) [87]. An example of an ion temperature and rotation profile measured on C VI is shown in fig. 2.16. Fig. 2.16(a) and 2.16(b) show a typical T_i and Ω_ϕ profile from both the equatorial and ITER-pilot lines of sight during a heating phase with full power NBI1. Fig. 2.16(c) and 2.16(d) show some rarely measured non-monotone rotation profiles in the presence of magnetic islands. Having two independent measurements from different viewing geometries and spectrometers allows an important check on the consistency of the results. The error bars are purely statistical and reflect the uncertainty in the fit.

2.6 Outlook

In this chapter, the physics of active hydrogen beam spectroscopy was reviewed from the perspective of an experimentalist. It was made clear that the largest difficulties

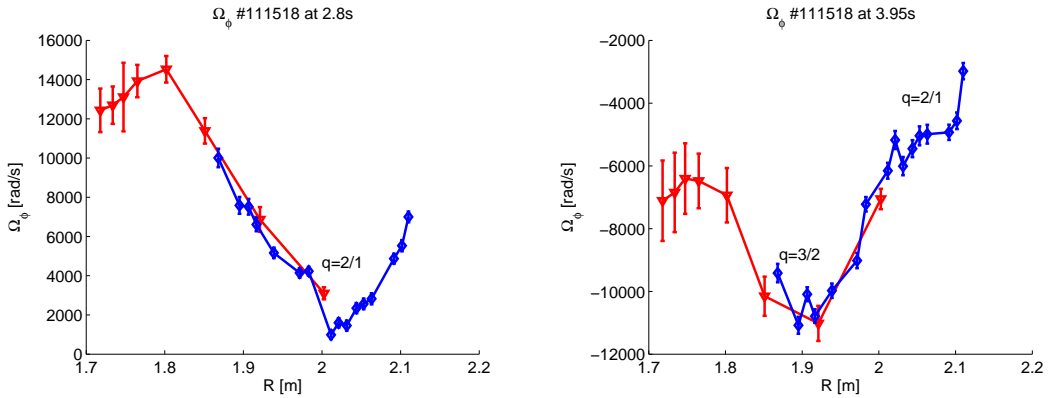
⁶<http://ipptwu.ipp.kfa-juelich.de/textor/all/<shotnumber>/star/cxrs>

⁷<http://orapsrv.zam.kfa-juelich.de/pls/ipptpd/tpd.tpd?strpath=/textor/all/<shotnumber>/tpd/cxrs>



(a) Ion temperature profile during 1.3MW NBI1 heating.

(b) Angular rotation profile during 1.3MW NBI1 heating.



(c) Angular rotation profile during 1.3MW NBI1 heating, with a 2/1 mode locked to the DC DED perturbation field.

(d) Angular rotation profile during balanced NBI1 and NBI2 heating (2.5MW), with freely rotating 3/2 and 2/1 modes.

Figure 2.16: Example of ion temperature and angular rotation profiles from TEXTOR measured with CXS on the C VI ($n=8-7$) line. The core data points (triangles) are measured along the equatorial lines of sight and have been analysed with an external wavelength calibration based on Ne I lines, while the points that extend further to the edge (diamonds) are from the ITER-pilot setup and have their wavelength axis fixed by making use of C III line at 530.462nm during an ohmic phase of the discharge. The error bars are statistical only, i.e. they only take into account the uncertainty from the fit provided the model fitted to the data (see sect. 2.2.2) is exact.

and atomic data and validation needs are related to obtaining the absolute impurity densities from the photon flux intensities. This issue will be treated in more detail in the following chapters and we will give an outlook to the application of CXS on ITER.

The experimental setup on TEXTOR, already described in this chapter, will be used for the fast ion studies and helium density validation measurements of chapters 4 and 5.

Atomic data for the interpretation of beam emission spectra¹

Contents

3.1	Abstract	49
3.2	Motivation	50
3.3	Atomic models of the neutral beam	51
3.3.1	Collisional-radiative models for the neutral beam (n-resolved)	51
3.3.2	Consistency of atomic data for NB emission	52
3.3.3	Consistency of atomic data for NB stopping	53
3.3.4	Collisional-radiative models for the neutral beam (nkm-resolved)	54
3.4	Measured vs. predicted beam emission intensity	56
3.4.1	Consistency of D_α and D_β beam emission intensities	56
3.4.2	Neutral beam power fractions from beam emission	60
3.5	Relative intensities within the MSE multiplet	62
3.6	Conclusions	64
3.7	Acknowledgement	66

3.1 Abstract

Several collisional-radiative (CR) models [88, 89, 90] have been developed to calculate the attenuation and the population of excited states of hydrogen or deuterium beams injected into tokamak plasmas. The datasets generated by these CR models are needed for the modelling of beam ion deposition and (excited) beam densities in current experiments, and the reliability of this data will be crucial to obtain helium ash densities on ITER combining charge exchange and beam emission spectroscopy. Good agreement between the different CR models for the neutral beam (NB) is found, if corrections to the fundamental cross sections are taken into account. First the H_α and H_β beam emission spectra from JET are compared with the expected

¹The contents of this chapter forms a paper published as [E. Delabie, M. Brix, R. J. E. Jaspers, C. Giroud, O. Marchuk, M. G. O'Mullane, Yu. Ralchenko, E. Surrey, M. G. von Hellermann, K. D. Zastrow, and JET-EFDA Contributors, *Consistency of atomic data for the interpretation of beam emission spectra.*, Plasma Phys. Control. Fusion, 52(12):125008, 2010.]

intensities. Second, the line ratios within the Stark multiplet are compared with the predictions of a sublevel resolved model. The measured intensity of the full multiplet is $\approx 30\%$ lower than expected on the basis of beam attenuation codes and the updated beam emission rates, but apart from the atomic data this could also be due to the characterization of the NB path and line of sight integration and the absolute calibration of the optics. The modelled $n=3$ to $n=4$ population agrees very well with the ratio of the measured H_α to H_β beam emission intensities. Good agreement is found as well between the neutral beam power fractions measured with beam emission in plasma and on the JET Neutral Beam Test Bed. The Stark line ratios and σ/π intensity ratio deviate from a statistical distribution, in agreement with the CR model in parabolic states from Marchuk et al. [70].

3.2 Motivation

Powerful neutral hydrogen or deuterium beams provide the dominant external heating and momentum input in most large scale tokamak experiments. For the interpretation of neutral beam (NB) heated discharges, detailed knowledge is required about the energy distribution of the neutrals (power fractions) and the attenuation of the beams in order to obtain radial profiles of the fast ion deposition and hence of the heating, torque and beam driven current. For the quantitative interpretation of charge exchange (CX) spectra, the local NB fluxes and population of excited states in the beam are needed to convert CX emissivities into local impurity densities. All these calculations strongly rely on the accuracy of the atomic data for the NB that is provided by collisional-radiative (CR) models of the beam [88, 89, 90, 91, 92].

When the beam emission spectrum (BES) was recorded for the first time, it was immediately proposed to monitor the beam attenuation, and hence the accuracy of the effective beam stopping cross sections, by using the observed beam emission intensities [93, 18]. This replaces the accumulated error on the beam attenuation along the beam path [55], by a local error in the beam emission rate. Beam emission, when combined with charge exchange recombination spectroscopy (CXRS), also has the potential of reducing the need of an absolute calibration of the CXRS spectra and a calculation of the intersection integral between a line of sight and the NB, to a relative calibration between several spectral bands [18, 51, 52]. The combination of BES and CXRS is the only feasible method to measure helium ash concentrations with the requested accuracy on ITER where only a small fraction (1-3%) of the diagnostic beam reaches the plasma center and where calibrations of the tokamak side optics on a regular basis will be impossible [54]. The beam emission intensity and Doppler shift is also widely used to characterise the beam (power fractions [55, 56, 57], alignment [58], divergence [57]).

Apart from using the intensity of the full BES multiplet, the σ/π intensity ratio [55, 71, 72, 54] and Stark splitting [59, 69] can be used as an alternative to polarisation based Motional Stark effect (MSE) diagnostics, as proposed for the ITER diagnostic and heating beam respectively. For these applications the Stark

level population structure of the beam neutrals is required to model the spectra, like for polarisation based MSE diagnostics when σ - and π -lines overlap.

Despite these promising applications, the use of beam emission has been hampered by the reliability of the involved atomic data and the complexity of the spectra. At the same time, the modelled NB fast ion deposition has been exploited at ever higher accuracy, thereby strongly relying on the accuracy of the underlying beam stopping calculations. It is the aim of this paper to check the consistency of the various beam modelling efforts and to quantitatively compare modelled neutral beam densities with measured beam densities from beam emission on JET.

In section 3.3 several published CR models for the neutral beam are compared. A distinction is made between models that implicitly assume a statistical population of the Stark levels within an n-shell (section 3.3.1-3.3.3) and models that have Stark level resolution (section 3.3.4). The latter models are mainly useful for the analysis of MSE data. In section 3.4 measured beam emission intensities from JET are compared to the expected beam densities from the beam stopping calculations. The expected line ratios within the MSE multiplet are compared with experimental data in section 3.5.

3.3 Atomic models of the neutral beam

3.3.1 Collisional-radiative models for the neutral beam (n-resolved)

The first neutral beam models that take excited states into account are by Boley et al. [94] and Janev et al. [91]. The focus of these works was solely on the penetration length of neutral beams. Although beam stopping is mainly determined by direct proton impact ionization and charge exchange from the ground state, excited states become increasingly important with increasing beam energy and plasma density. Seraydarian et al. [93] found relatively good agreement between the measured and predicted beam emission intensity on DIII-D, using a model based on the data of Boley et al. [94]. However, the ion impact excitation cross sections used in [94] were too large, which makes the interpretation of the beam emission results in [93] difficult. Mandl et al. [55] compared the measured and expected beam densities on JET using the ADAS CR model (here referred to as ADAS89). They found relatively good agreement between model and experiment. Anderson et al. [88] thoroughly revisited the ADAS beam model (here referred to as ADAS97) and brought it to a large extent in line with the 1993 review of atomic data by Janev and Smith [95]. The observed intensity on JET was found to be 30% lower than predicted. Hutchinson [89] built a CR model of the beam based on the Janev 1989 and 1993 atomic datasets [91, 95] and found a large discrepancy with ADAS97. Marchuk et al. [90] assessed the atomic data needs for active beam spectroscopy on ITER (based on the Janev 1993 dataset) and found a good agreement between their CR model and ADAS97, but only compared for the ITER diagnostic beam relevant conditions of 100keV/amu.

3.3.2 Consistency of atomic data for NB emission

An investigation of the discrepancies between the CR models [88, 89, 90] revealed two issues: (1) The high energy part of the proton impact ionization cross section for excited states published in the Janev 1993 review is based on erroneous input data from [96]. Although this error was noted [97, 98] and corrected by the authors [99], the IAEA recommended data in the Alladin database [100] has not changed yet. A new fit to the ionization cross sections has been made and implemented in the CR models of ADAS (see [101] for details) and Marchuk et al. The different datasets are compared in fig. 3.1. (2) Furthermore, a bug in the ADAS CR code affected the CX cross sections for excited donor states in hydrogen, strongly affecting the beam emission rates below 100keV/amu. The corrected dataset will here be referred to as ADAS10². The result of these corrections is visually depicted in fig. 3.2. Both the corrected emission rates of ADAS, Marchuk et al. and Hutchinson agree within 5% for the plasma and beam conditions studied here. The measured beam densities derived from these beam emission rates will be compared with experimental data from JET in section 3.4.

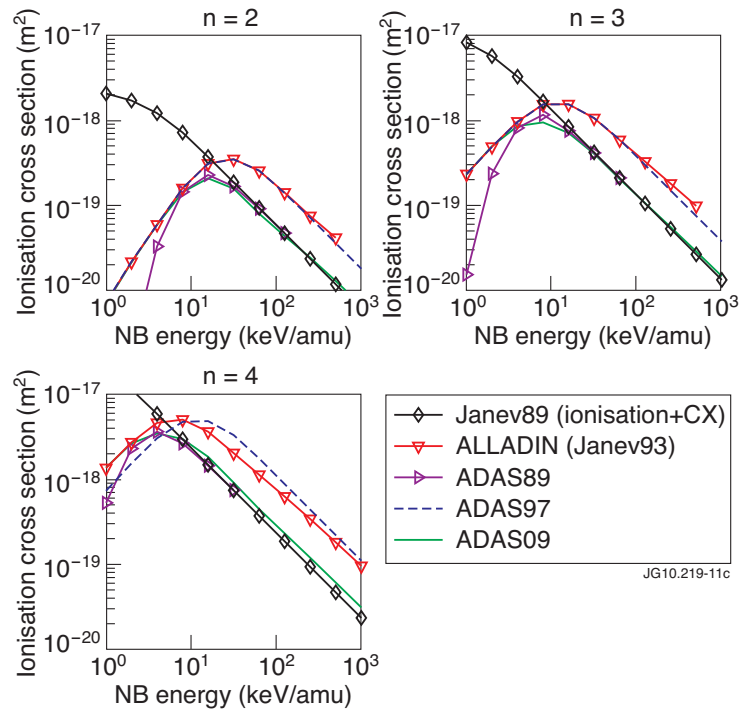


Figure 3.1: Proton impact ionization of excited states of the hydrogen atom. Recommended data sets (Janev89 [91] and Janev93 (as in the ALLADIN database) [95, 100]) and data used in the ADAS beam emission models are shown.

²This data is part of ADAS release v3.1.

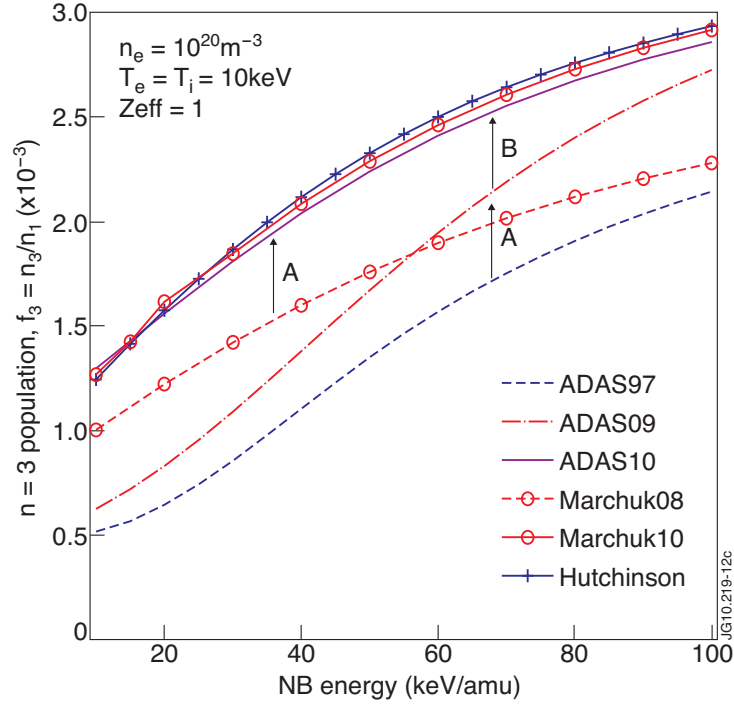


Figure 3.2: $n=3$ population in the beam with regard to the ground state according to different CR models. ADAS: ADAS excited beam population [88, 24]; Marchuk: $n=3$ population from Marchuk et al.[90]; Hutchinson: excited population digitised from fig. 3 in Hutchinson[89]. **A** denotes the change due to the correction of H($n>1$) ionization, **B** marks the change due to a correction of H($n>1$) charge exchange in ADAS.

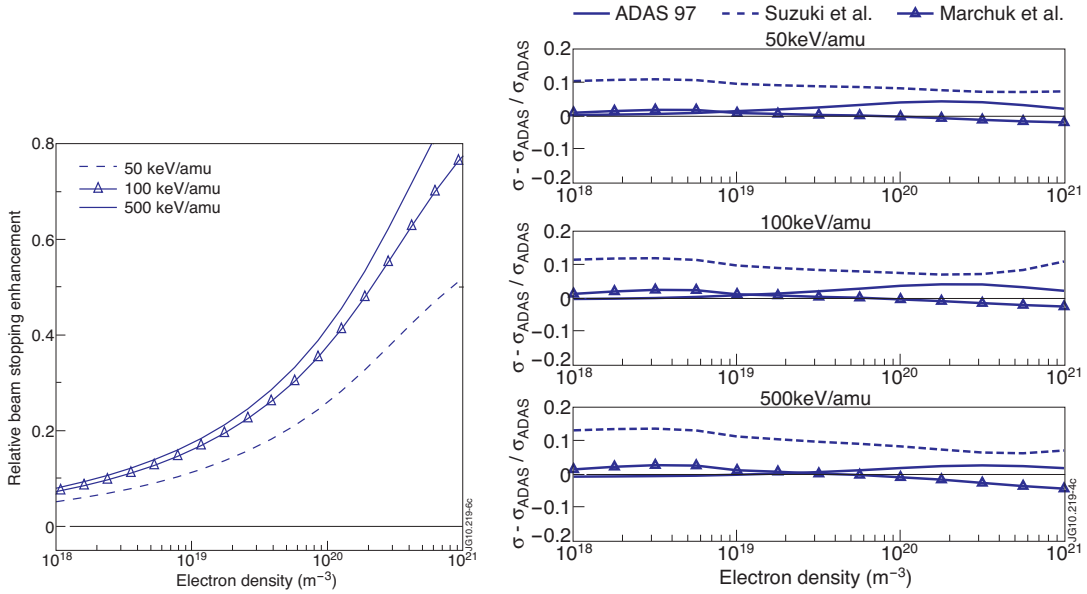
3.3.3 Consistency of atomic data for NB stopping

The changes mentioned above in the electron loss cross sections from excited states in the neutral beam, and the corresponding uncertainties, have only a small influence on the NB stopping cross sections for current experiments. This is because excited states only contribute $\approx 20\%$ to the effective beam stopping cross section for JET-like beams and plasmas (50 keV/amu , $n_e = 5 \cdot 10^{19} \text{ m}^{-3}$). For ITER-like beams (500 keV/amu , $n_e = 1 \cdot 10^{20} \text{ m}^{-3}$) however this augments to $\approx 45\%$. The models used here do not take ionization by the Lorentz field into account, which is negligible for present experimental conditions but could increase the ionization through excited states even further for the ITER heating beams. In figure 3.3(a) the increase of the beam stopping cross section due to stepwise ionization is shown as a function of electron density for several NB energies. In figure 3.3(b) beam stopping cross sections from several datasets are compared. The difference between the beam stopping cross sections from ADAS and Marchuk et al. [90] is in all conditions below a few percent. The analytical expressions for the beam stopping cross sections provided by Suzuki et al. [92] are on average 10% higher for current experimental conditions. The 1989 effective beam stopping data from Janev et al. [91], which is based on outdated data compared to the 1993 review by Janev and Smith [95] and

is not shown here, is higher by more than 20% but merges with the current data at beam energies of several 100keV/amu. The change between the ADAS10 and ADAS97 beam stopping cross sections is also plotted. The difference stays below 5%. In conclusion, the different sets of beam stopping data for deuterium plasmas [88, 90, 92] only show a small deviation and are for current experimental conditions dominated by ion impact ionization and charge exchange from the ground state. Changes in the excited population (e.g. ADAS97 vs. ADAS10) only have a modest impact on beam stopping. It is the accuracy of the fundamental datasets concerning the ground state that determines the overall accuracy of the beam stopping cross sections. The quality of proton impact ionization from the ground state is classified in category B by the IAEA [100] and charge exchange with low-Z ions is categorised as B-C (B: uncertainty 10-25%, C: 25-50%). Charge exchange is dominant below 40keV/amu and ion impact ionization above 40keV/amu. Since Janev and Smith's review on atomic data for fusion plasmas in 1993 [95], there has been remarkable progress in theory concerning these cross sections. The newly published charge exchange cross sections appear to be consistent with the recommended data, but discrepancies have been published for ionization in the intermediate energy region (30-150keV/amu). In figure 3.4(a) the ion impact ionization cross sections from several authors [102, 103, 104, 105] are plotted in comparison with the recommended data [95]. This new data lies higher by about 30% at the peak in the cross section. The Janev and Smith 1993 [95] parametrization at the cross section peak is mostly fitted to the experimental data from Shah et al. [106, 107]. Initially this agreed with close coupling theory, but it was later shown that these results were not converged [104]. Figure 3.4(b) shows the effect if these increased cross sections would be implemented in the CR beam model. The beam stopping cross section is enhanced by approximately 10% for a typical positive ion source neutral beam operating at 50keV/amu. Until confirmation of these theoretical results, we have in this publication used the recommended fundamental cross sections for beam stopping for the comparison between measured neutral beam densities from beam emission and modelled beam densities. We have also found no experimental evidence in our data that the current beam stopping cross sections would be too low. Note that this issue does not affect the beam emission rates, it only affects the attenuation of the beam in the modelled beam density that is used as comparison. For JET (50keV/amu) the beam density at the magnetic axis would typically be lowered by 15%, this effect increases to 50% for the ITER diagnostic beam (100keV/amu).

3.3.4 Collisional-radiative models for the neutral beam (nkm-resolved)

In the models described above a statistical population among the Stark states within the same n-shell was assumed. The violation of this assumption has clearly been demonstrated on JET [55] and it affects the MSE line ratios and σ/π intensity ratio. Boileau et al. [18] included all parabolic states into the ADAS CR model up to n=4, extending the model with statistically populated levels at higher n. Excitation cross sections between parabolic states (derived from (nlm)-resolved cross sections) are not

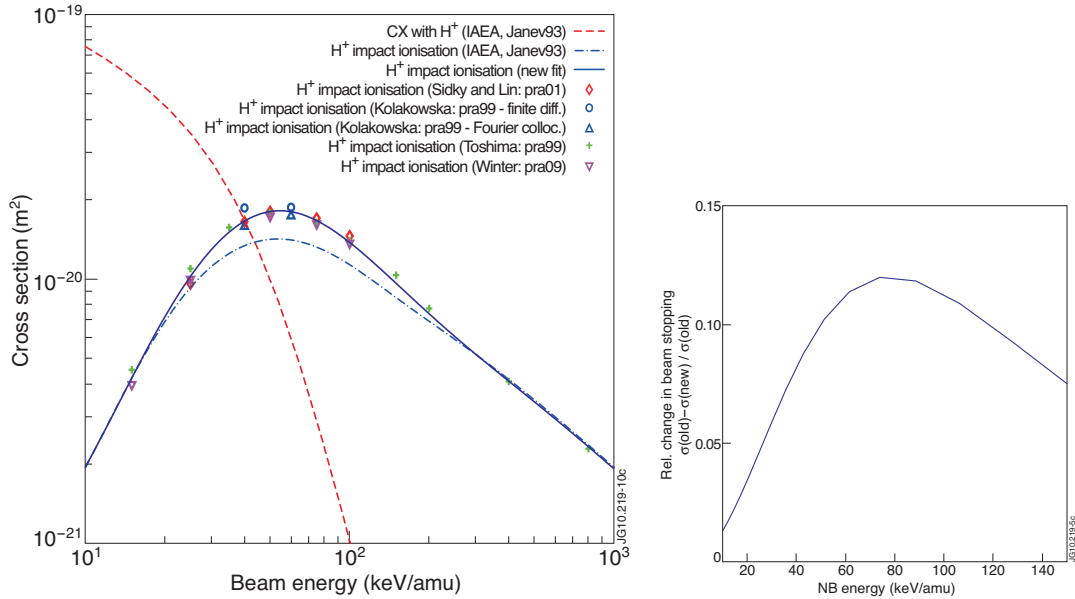


(a) Relative increase of the beam stopping cross section due to stepwise ionization through excited states as a function of electron density, using the CR model of Marchuk et al. [90]. ($T_e=T_i=5\text{keV}$, $Z_{\text{eff}}=1$)

(b) Comparison of NB stopping cross sections from several CR models for the NB. The difference due to the correction of the excited state ionization and charge exchange is also shown. ($T_e=T_i=5\text{keV}$, $Z_{\text{eff}}=1$)

Figure 3.3: The role of excited states in NB stopping and consistency of beam stopping cross sections from several models.

available in literature and therefore these cross sections were calculated in the first Born approximation (B1). Gu et al. [68] repeated this modelling up to $n=5$ for use in MSE diagnostic modelling, but their B1 cross sections deviate from those calculated by Boileau et al.. The validity of B1 cross sections at the intermediate beam energies (≈ 50 keV/amu) used in current experiments is questionable (see e.g. [25, p. 258]). Marchuk et al. [70] have calculated the (de)excitation cross sections between all parabolic states in Glauber approximation up to $n=10$ and implemented these in the NOMAD CR code [108]. For ionization and charge exchange, no (km)-dependence of the donor atom is assumed and the recommended data [95, with corrected ionization] has been used. The results show a significant deviation of the Stark line ratios with regard to the statistical expectation. A strong dependence on the angle between the direction of the collisions and the electric field is found. In figure 3.5(a) the line ratios within the MSE multiplet are plotted for the three published Stark resolved CR models [18, 68, 70]. Figure 3.5(b) show the total Balmer- α emission rate compared to the same model enforcing a statistical population (restricted to $n=5$, $T_e=T_i=5\text{keV}$ and beam voltage is 50keV/amu). The difference is small at the densities used in current tokamak experiments. The time the beam needs to reach a steady-state population with regard to the ground state is not significantly altered compared to the model that assumes a statistical population (max. 3cm at 50keV/amu for $n=3$).



(a) Recommended data for ionization and charge exchange compared with data from recent theoretical publications [102, 103, 104, 105]. (b) Impact of the change in ion impact ionization on the NB stopping cross section. ($T_e=T_i=5\text{keV}$, $Z_{\text{eff}}=1$)

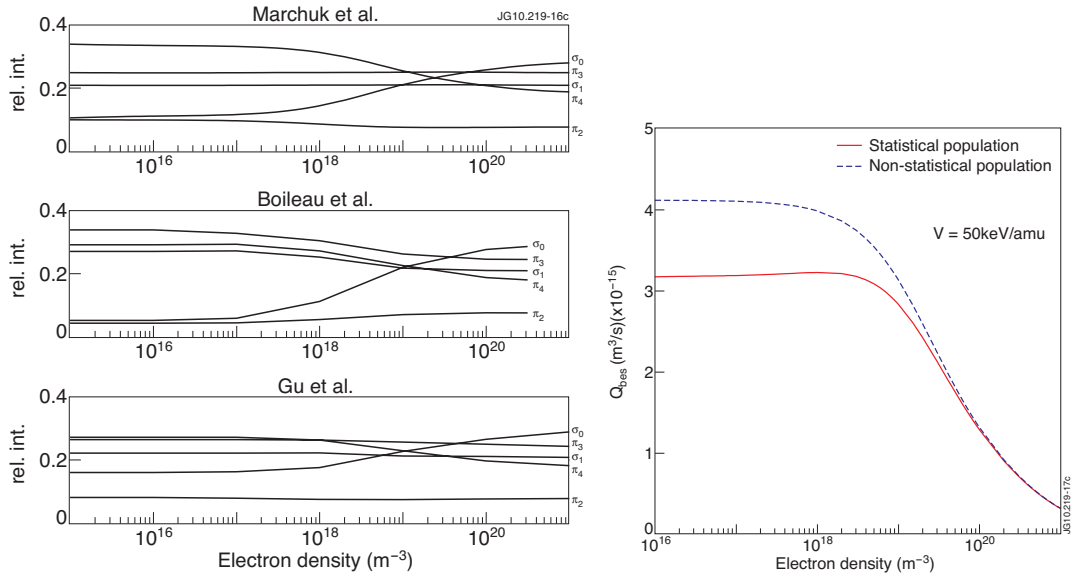
Figure 3.4: Recent theoretical results on the cross sections for H⁺ impact ionization and charge exchange of H(1s), and the impact on the effective beam stopping cross sections.

The MSE line ratios and σ/π intensity ratio will be compared with data from JET in section 3.5.

3.4 Measured vs. predicted beam emission intensity

3.4.1 Consistency of D_α and D_β beam emission intensities

Beam emission spectra on JET can be recorded along the lines of sight (l.o.s.) of the core CXRS diagnostic [109] on either the blue or red shifted wing of the unshifted D_α peak, depending on which viewing geometry is used. In fig. 3.6 a D_α beam emission spectrum is shown and fig. 3.7 shows a D_β spectrum. The beam emission features of several beams sometimes overlap and can only be distinguished if either the beam voltage is different or if beams from different beam banks ('normal' or 'tangential' [58]) are used. The spectra shown here originate from a pulse where only one beam effectively contributed. A fitting code has been developed to process the full D_α or D_β spectrum, including the beam driven DI charge exchange contribution and the parasitic CII Zeeman multiplet around 6580. The results of the fit are also shown in figs. 3.6-3.7. The ion temperature and plasma rotation derived from the DI CX components is in reasonable agreement with the ion temperature and rotation measured on CVI CX, although no extensive comparison has been made.



(a) Line ratios within the MSE multiplet from several Stark resolved CR models [70, 18, 68].

(b) Comparison of the H α beam emission rate for the (nkm)- and n-resolved CR model of Marchuk et al. [70] (restricted to n=5, V=50keV/amu, T_e=T_i=5keV)

Figure 3.5: Effect of Stark level resolved modelling on the MSE line ratios and on the total H α beam emission rate.

In order to compare the measured beam emission intensities with the expected beam densities, the NB attenuation code CHEAP (CHarge Exchange Analysis Package) has been used. The measured beam intensities are converted to the local beam densities integrated along a l.o.s. using the ADAS10 effective emission rates, and the same quantity is obtained from CHEAP using the known intersections between the l.o.s. and the NB. In fig. 3.8, timetraces of the line integrated NB density (full energy fraction) are shown from both beam emission and from the NB attenuation code. Fig. 3.9(a) shows a radial profile of the NB density for all three energy fractions in the beam. The measured (labelled 'BES') and expected beam densities (labelled 'BMS') show qualitatively the same behaviour, but they differ by a constant factor. There is a larger deviation on the track closest to the edge. This latter observation was also made by Mandl et al. [55] and Boileau et al. [18]. This deviation increases at lower electron density and could qualitatively be attributed to the inappropriate use of steady state emission rates in this region of the plasma where a large electron density gradient exists. We have applied time dependent CR modelling but this did not entirely explain the observations, unless an inaccuracy in the localisation of the measurement or the local electron density was assumed as well.

A comparison of the beam densities measured on D β and D α BES respectively, yields an accurate check on the modelled n=4 to n=3 population in the beam. The D β emission rate is approximately a factor 10 lower than the D α emission rate. Nev-

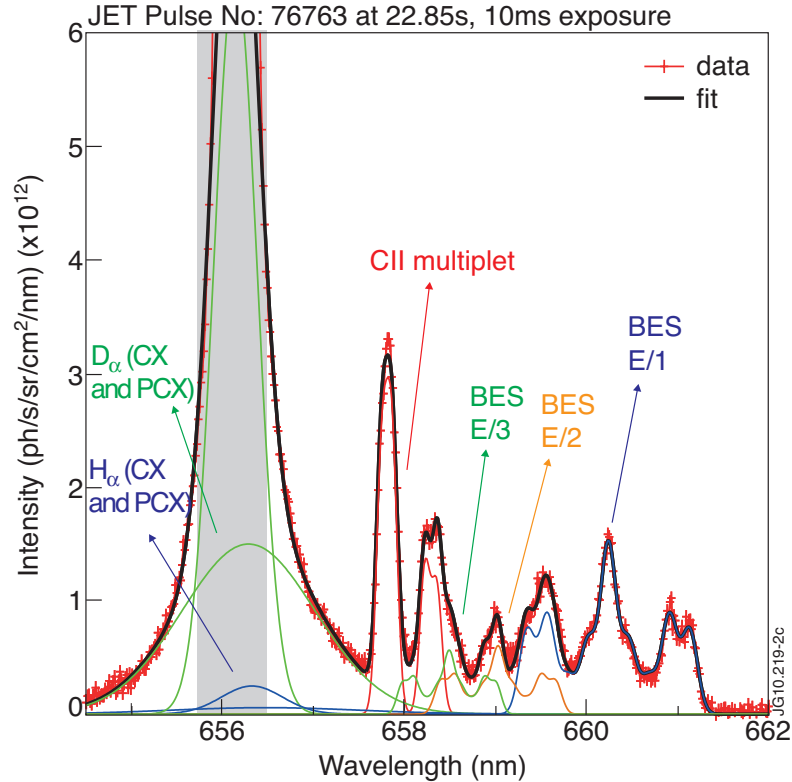


Figure 3.6: D_α spectrum from JET, the experimental data is in red, other lines are fitted features. The three energy components of the BES spectrum are indicated. The active and passive D/H CX contributions are approximated as gaussian lines. The coldest part of the D_α/H_α spectrum (the grey area) is usually overexposed and is neglected in the fit.

ertheless, the measured beam densities agree very well using the ADAS10 emission rates. This is illustrated in fig. 3.9(b) on two consecutive, nearly identical shots, one with the spectrometer tuned to D_α BES, one to D_β . The measured densities agree within approx. 10%. Most of the difference is correlated with noise on the LIDAR electron density profile. Note that a relatively large discrepancy was found using the outdated emission rates.

As mentioned before, the BES and CHEAP line integrated beam densities agree very well except for a general scaling factor. In fig. 3.10 the measured beam density is plotted against the modelled density for the full energy component in the NB. The measured beam density is 34% lower than expected for beam 8.7 [58]. Apart from the issues related to the atomic modelling of the excited states addressed in this paper, the remaining discrepancy could also be due to inaccuracies in the assesment of the intensity calibration and the geometry between l.o.s. and NB.

The calibration and alignment with the beams is described in detail by Giroud et al. [58]. The optics are calibrated with an absolutely calibrated source, except for the last window which is calibrated by sending a laser to a retroreflector inside the

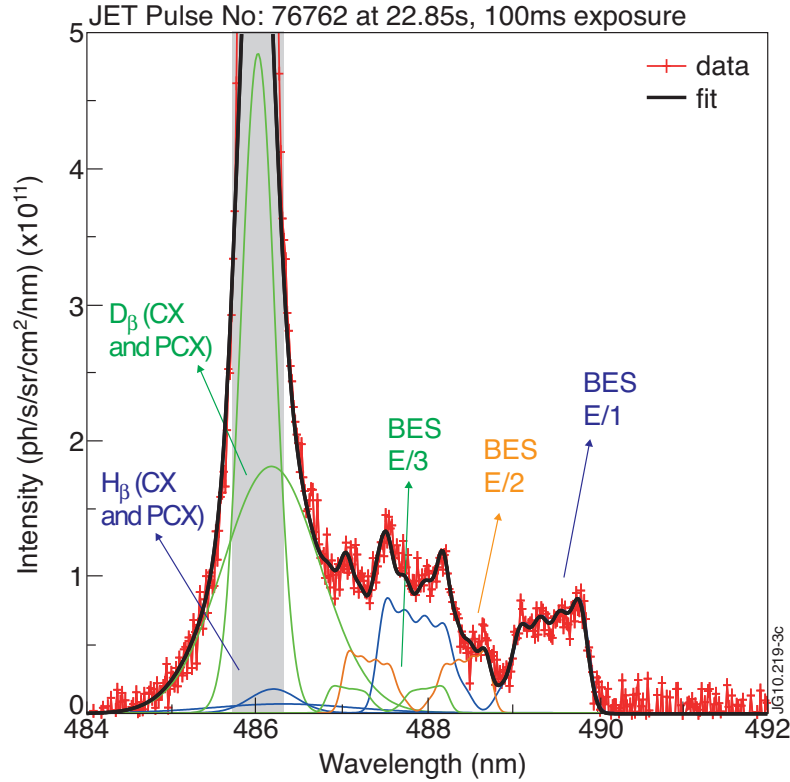
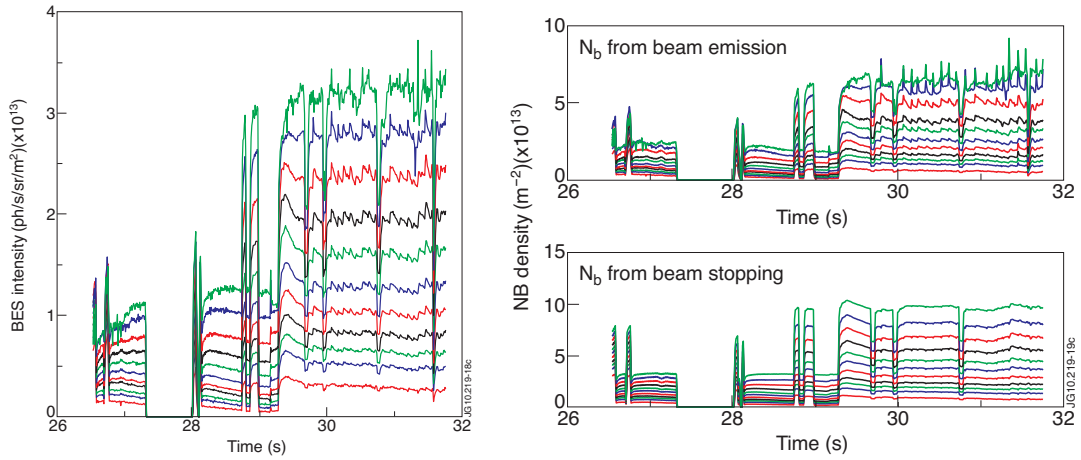


Figure 3.7: Example D_β spectrum from JET. The coldest part of the D_β/H_β spectrum (the grey area) is neglected in the fit.

tokamak vessel. The alignment between the lines of sight and the neutral beams is based on beam emission Doppler shifts and relative CX intensities when individual beams are switched on/off. The anticipated accuracy of the calibration factor is 6-20% (see [58] for details).

The uncertainty on the active volume is as low as 2% [58], but only if the neutral beam path can be assumed to be perfectly characterized. The characterization of the beam path is the main source of uncertainty in the determination of the active volumes. The model used to obtain the path length through the beam assumes a diverging gaussian beam, which is a fair approximation far enough from the beam source, as demonstrated by the beam trajectory simulation code described in [110], which is benchmarked against the beam position and divergence measured from the beam footprint obtained on a calorimeter plate in the neutral beam box [110].

The presence of impurity ions affects both the beam stopping and emission rates. The C^{6+} concentration from CXRS has been taken into account in the evaluation of both the beam stopping and the beam emission rates, neglecting other impurities. Beam stopping is, at 50keV/amu, a weak increasing function of Z_{eff} , while the beam emission rates decrease with increasing the impurity concentration. However, for the discharges studied here, Z_{eff} from Bremsstrahlung was below 2 and a unreason-



(a) Beam emission intensity of the full energy component for #72324 along several lines of sight of the JET core CXRS diagnostic. Two beams contribute to the beam emission spectrum. (b) Time traces of the line integrated NB density (E/1 component) derived from beam emission (top) and from a NB attenuation code (bottom) for #72324. Two beams contribute to the line integrated beam density.

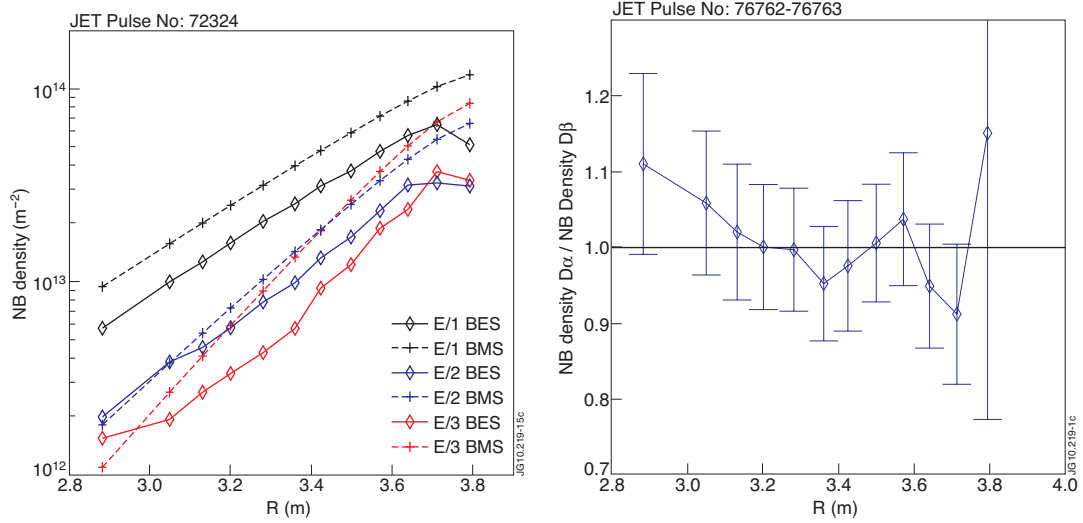
Figure 3.8: Time traces of the beam emission intensity and the beam density along a line of sight (E/1 component beam 8.7 + 8.8).

ably large carbon concentration should be assumed to change the measured beam density by 30%.

The attenuation of the neutral beam and hence the NB power deposition is mainly a function of electron density. The ratio between expected and measured beam densities along a core track as function of integrated electron density along the neutral beam path gives a calibration independent verification of the beam stopping. Within the range of electron densities for which we have beam emission data, we have seen no trend in the ratio of BES to CHEAP full energy beam densities as function of electron density. This gives confidence in the effective beam stopping cross sections that are currently in use, although the range of attenuation factors obtained on a single core track was too small to resolve the issue concerning H(1s) ionization by proton impact mentioned in section 3.3.3.

3.4.2 Neutral beam power fractions from beam emission

Following the methodology of section 3.4.1, beam in plasma emission can be used to characterize the distribution of the beam power over the partial energy fractions in the beam (see e.g. Mandl et al. [55] for an earlier application of this method). The results of this analysis have been compared with the power fractions based on measurements on the JET Neutral Beam Test Bed and measured by beam into gas emission firing the neutral beam into the tokamak vessel filled with D_2 gas at low pressure. The JET NB Test Bed does not have a bending magnet to remove ions from the partially neutralised beam leaving the neutraliser and therefore the test



(a) Profile of the NB density integrated along a l.o.s. for the three energy fractions in the beam for #72324 at 30.3s. 'BES' refers to measured data using beam emission, 'BMS' is the expectation from a beam stopping code.

(b) Ratio of NB densities measured on D_α and D_β beam emission from two similar discharges. The NB attenuation code predicts a maximum difference between the shots of approximately 5% at this time frame. The beam density measured on D_α is consistent with the beam density measured on D_β.

Figure 3.9: Consistency between beam densities from beam emission and the expected NB density from a beam attenuation code (#72324) and consistency between D_α and D_β.

bed analysis is based on the interpretation of beam emission from a mixed beam of ions and neutrals fired onto a gas target. It requires extensive modelling [65, 66] to interpret the spectroscopic data from the test bed in terms of the power fractions in the ion beam leaving the source. This is then modelled forward in order to obtain the power fractions in the neutralized beam. The comparison with the beam in plasma power fractions revealed a misinterpretation of the spectroscopic data on the NB Test Bed as it is described in [65] and [66] (the beam density in eq. (2) in [66] should be beam particle flux, therefore the power in the E/2 and E/3 fractions were underestimated by $\sqrt{2}$ and $\sqrt{3}$ respectively). This error has been corrected and the result of the comparison with beam in plasma emission is shown in fig. 3.11(a) for a beam voltage scan. Fig. 3.11(b) shows the comparison for a series of beam into gas discharges on JET. After correction of the test bed power fractions and the beam emission rates, all three methods agree rather well.

For the beam into gas discharges of fig. 3.11(b), the agreement at the highest and lowest voltage is very good, but a slight discrepancy is seen between 40 and 50 kV/amu. Experimentally determined H_α emission cross sections from Williams et al. [64] have been used for both the NB into gas power fractions shown here and for the test bed analysis where the emission originates from both the excitation

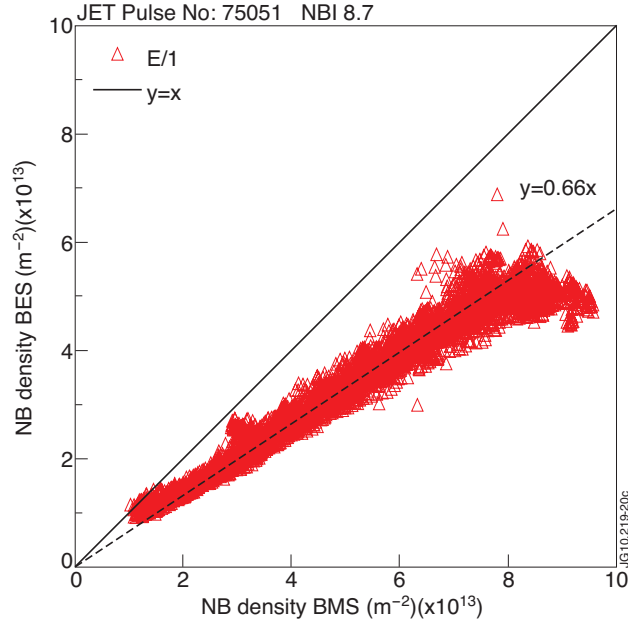
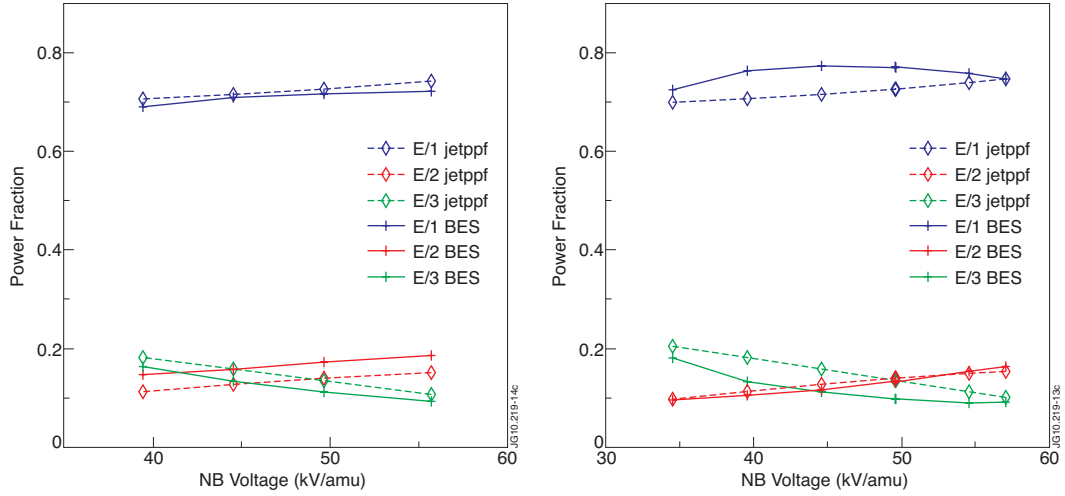


Figure 3.10: NB density from BES against the beam stopping (BMS) prediction for beam 8.7 (#75051). The odd edge channel (see fig. 3.9(a)) is neglected.

of the neutrals and charge exchange of the ions. The excitation cross sections of atomic hydrogen in H_2 have larger error bars than the H^+ charge exchange cross sections in H_2 [64]. This puts in doubt the reliability of NB into gas experiments for measurement of the NB species mix, despite the more extensive modelling that is required when the power fractions are measured on the ion beam on the test bed or on the neutral beam during standard tokamak operation. The good agreement which is obtained here between the NB in plasma power fractions and the test bed data does not only give some confidence in the voltage scaling of the emission rates between 10 and 55 keV/amu, it also indicates that beam into plasma emission is a reliable method to obtain the NB species mix in situ.

3.5 Relative intensities within the MSE multiplet

The MSE multiplet on JET is sufficiently resolved on the core channels of the CXRS diagnostic to observe the individual lines of the full energy component. Therefore the measured line intensities can be used to check the modelled Stark level population within $n=3$. Because the σ -lines are polarized perpendicular to the Lorentz field and the π -line parallel, the observed intensities between σ - and π -lines can be distorted if the front end optics are sensitive to the polarization. Therefore only the ratio of the lines within one polarization group provides a direct comparison which is free from geometric or diagnostic artifacts. Fig. 3.12 shows the measured and predicted MSE line ratios as a function of electron density. Although the minimum electron density that was obtained, is not low enough to do an accurate check on the electron



(a) The data labelled 'BES' is from beam emission in plasma (#75046-75050), the data labelled 'jetppf' shows the expected power fractions. (b) The data labelled 'BES' is from beam in gas emission (#77528-77534), the data labelled 'jetppf' shows the expected power fractions.

Figure 3.11: Distribution of the power among the fractional energy components in the NB, as a function of beam voltage. The power fractions measured with beam emission are compared with the expected fractions from a model based on test bed measurements.

density scaling, the agreement with the modelled line ratios that were obtained with Marchuk et al.'s CR model [70] is very good and the deviation with the statistical line ratios is clear.

The use of the ratio between the observed σ and π radiance to obtain information on the direction of the Lorentz field, and hence on the magnetic pitch angle, has rarely been successful. This is mainly due to the non-statistical features in the MSE spectrum. The classical polarization based MSE diagnostic [60] is much less sensitive to this effect, except when σ and π lines overlap in the sampled wavelength region. In this case a change in electron density could change the amount of σ and π light which is sampled. In fig. 3.13 the modelled total σ - and π -emissivity is plotted as a function of electron density for a beam energy of 55keV/amu. The difference with the statistically expected ratio can be as high as 20% for standard tokamak conditions. In order to compare with the experimentally observed ratio, the disturbing effect of the geometry and the polarization sensitivity of the first mirror was obtained using the ratio between the σ_1 - and π_3 -lines. These originate from the same upper level and hence $\Phi_{\sigma_1}/\Phi_{\pi_3}$ is independent of the population structure. However, because the Stark splitting is usually not large enough, it is in practical situations difficult to obtain this ratio with the accuracy that is needed for direct use as a constraint on the magnetic field reconstruction. The measurements compare well to the model, but the use of Φ_{σ_1} and Φ_{π_3} induces considerable statistical noise.

In fig. 3.14, the expected measurement Φ_{σ}/Φ_{π} is plotted as a function of the angle θ between a line of sight and the Lorentz field taking into account the effects of

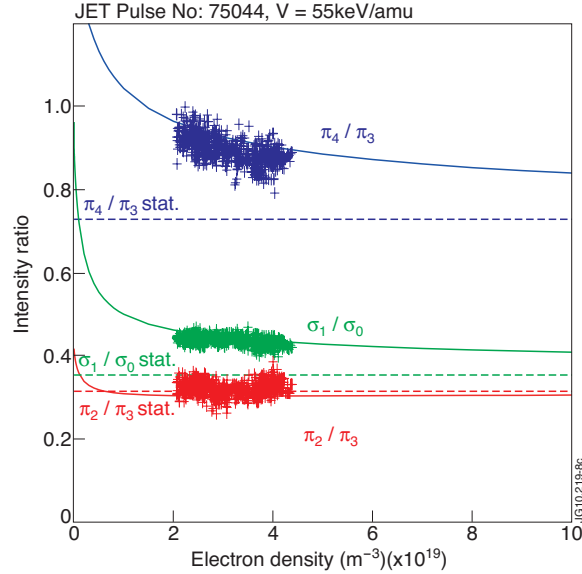


Figure 3.12: Stark line ratios within the MSE multiplet as a function of electron density. Data from a central track of the JET core CXRS diagnostic (MSE multiplet best resolved) is compared with the model from Marchuk et al. [70]. The dashed lines show the expected line ratios when the $n=3$ level would have a statistical subpopulation.

the $n=3$ non-statistical population and a first mirror with an s -reflectivity which is 15% larger than the p -reflectivity. This value was obtained from the $\Phi_{\sigma 1}/\Phi_{\pi 3}$ ratio and the known beam and l.o.s. geometry during a beam into gas shot for which the magnetic field is purely toroidal. One can see that the main effect that causes a deviation between the simple geometrical prediction ($\Phi_{\sigma}/\Phi_{\pi} = (1 + \cos^2 \theta)/\sin^2 \theta$) and the measurements is the non-statistical character of the $n=3$ population. The measured points agree very well to the modelled curves, however for the equatorial viewing geometry used here, this method cannot be used to obtain useful information about θ (and hence the magnetic pitch angle), because a large change in θ is needed to cause a measurable change in Φ_{σ}/Φ_{π} .

3.6 Conclusions

In this paper we have analysed the consistency of several collisional-radiative models [88, 89, 90] that have been developed to calculate the neutral beam stopping and population of excited states in hydrogen plasmas. The results of the calculations are compared with experimental data from JET. Revisiting the proton impact ionization of excited states and identification of a mistake in the ADAS rescaling of the charge exchange cross sections allowed us to achieve consistency between all models. The corrected data will be in a next ADAS release. The calculated relative $n=3$ to $n=4$ population agrees within 10% to the measured ratio from JET using the H_{α} to H_{β} beam emission intensities. Good agreement is found as well on the

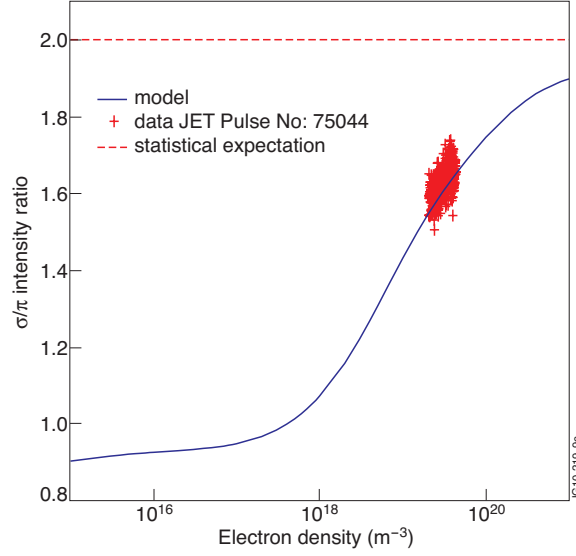


Figure 3.13: Ratio between the total σ - and π -emissivity (integrated over all solid angles). The experimental data points have been obtained from the measured σ - and π -radiances through $\frac{I_\sigma}{I_\pi} = \frac{\Phi_\sigma}{\Phi_\pi} \frac{\Phi_{\sigma 1} A_{\pi 3}}{\Phi_{\pi 3} A_{\sigma 1}}$. The label 'model' refers to the model of Marchuk et al. [70]. The dashed line shows the statistical prediction $I_\sigma = 2I_\pi$

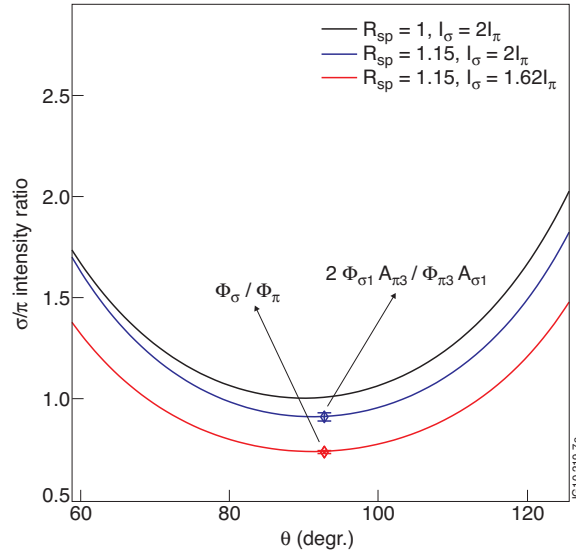


Figure 3.14: Ratio of the expected σ - over π -radiance as a function of angle θ between a core line of sight and the Lorentz field. R_{sp} is the ratio between the s- and p-reflectivity of the first mirror. The case $R_{sp}=1$, $I_\sigma=2I_\pi$ corresponds to the standard prediction $\Phi_\sigma/\Phi_\pi = (1 + \cos^2 \theta)/\sin^2 \theta$. The blue and red curve correspond to the situation with a polarization sensitive first mirror and with a $n=3$ population that has not reached a statistical distribution. The points indicate measurements from JET #75044. For this viewing geometry a large change in θ is needed to cause an appreciable change in the measured Φ_σ/Φ_π intensity ratio.

power fractions measured with BES and on the JET Neutral Beam Test Bed, if a correction to the analysis in [65, 66] is taken into account. The power fractions measured with neutral beam in gas emission show a slightly larger deviation. The radial profiles and time traces of the measured and modelled NB density agree well but the overall intensity of the measured beam density is $\approx 30\%$ lower. The reason for this is uncertain. Apart from the involved atomic data, this could also be due to a combination of calibration, alignment and especially the characterization of the neutral beam path. These issues are currently the main motivation to use beam emission. The Stark line intensities within the MSE multiplet are in good agreement with a sublevel resolved model [70]. The measured σ/π intensity is disturbed by the polarization characteristics of the tokamak side optics and the $n=3$ subpopulation structure, the latter effect is consistent with the CR modelling.

The overall agreement found on JET between the modelled and expected beam emission intensities gives confidence in the proposed scheme combining charge exchange and beam emission that will be used to measure the helium ash on ITER. The agreement between the modelled and measured MSE spectra gives confidence in the Stark resolved CR modelling and hence such a model could be used to correct the measured σ/π -ratio when used to constrain magnetic field reconstructions.

3.7 Acknowledgement

This work was supported by EURATOM and carried out within the framework of the European Fusion Development Agreement. The views and opinions expressed herein do not necessarily reflect those of the European Commission.

Fast ion charge exchange

Contents

4.1	Principles and background of the technique	67
4.2	Test of fast ion charge exchange spectroscopy on TEXTOR	68
4.2.1	Instrumentation	68
4.2.2	Sample Data	70
4.2.3	Modelling and Interpretation	72
4.2.4	Passive charge exchange emission	74
4.3	Test of fast ion charge exchange spectroscopy on JET . . .	75
4.4	Discussion and conclusion	78

4.1 Principles and background of the technique

In a DT fuelled fusion reactor, about 20% of the generated power is channelled to the ^4He fusion product. The operation of fusion reactors will rely on the heating of the plasma by the slowing down of these fusion produced α -particles to balance the energy losses and to maintain a steady-state operating regime. External heating and control of the ion population in the plasma via the injection of energetic neutral beams or electromagnetic waves that are in resonance with the gyromotion of the ions rely on the same principle of creating a fast ion source and heating the plasma through the slowing down of these ions. Therefore, confinement of fast ions and understanding fast ion transport is crucial for the development of a steady operating scenario. Apart from transport considerations related to the heating of the plasma by fast ions is it of capital importance to protect the inner wall of fusion reactors from impact by energetic ions. The current view on fast ion behaviour (reviewed in detail by Heidbrink et al. [111], and by the ITER Physics Group on Energetic Particles [112]) is that the transport is neoclassical, except for transient transport phenomena such as interaction with MHD modes as fishbones, sawteeth and toroidal Alfvén eigenmodes that can cause a radial redistribution of the fast ions and can in the extreme lead to the fast ions being expelled from the plasma. It should be noted however that the diagnostic evidence on which the knowledge on fast ion transport is based is mainly indirect and bound to large uncertainties due to the modelling involved in the interpretation of the diagnostic data. More recent work [113] partially deviates from the (neo)classical view on fast ion transport by

measuring diffusivities which resemble turbulent transport. In order to clarify the fast ion transport mechanisms, the further development of diagnostics that can provide information about the spatial profiles or the velocity distribution of confined fast ions is more than desirable.

Section 2.2.5 of chapter 2 contains a brief introduction of the methodology. The next two sections 4.2 and 4.3, contain a paper on the application of fast ion CXRS on TEXTOR and a test of this method using the instrumentation for thermal CXRS on JET.

4.2 Test of fast ion charge exchange spectroscopy on TEXTOR ¹

In this section the fast ion relevant capabilities of the upgraded CXRS diagnostic on TEXTOR are described. The diagnostic setup is aimed at combining the information from the emission following charge exchange between circulating fast ions and neutral particles from a beam and the emission from excited neutral beam particles. The use of CXRS as a fast ion diagnostic depends on two items: (1) the diagnostic capability to detect the spectrum, described in section 4.2.1 and 4.2.2 and (2) the interpretation of the signal, partially based on modelling - discussed in section 4.2.3. Section 4.2.4 contains a discussion on problems caused by background emission. Possible improvements to the diagnostic are suggested.

4.2.1 Instrumentation

In order to detect fast ion slowing down features, a charge exchange diagnostic with high optical throughput is needed with a spectrometer and ccd camera that can detect the whole relevant wavelength range with sufficient spectral resolution to resolve parasitic impurity lines. The geometry between line of sight and magnetic field at the intersection with the neutral beam determines to which part of velocity space the diagnostic will be sensitive to.

The CXRS diagnostic [114] on TEXTOR has been upgraded to adress several physics issues related to the exploitation and hence the design of the core ITER CXRS diagnostic which will look to the 100keV/amu hydrogen DNB from upper port 3. Therefore, this TEXTOR setup has been called ITER-pilot to distinguish it from the other CXRS diagnostics on TEXTOR. One of the characteristics it has in common with the core ITER CX diagnostic is the viewing geometry. The 19 lines of sight that are used for the work in this chapter span a radial range from 1.85 to 2.13m and intersect one of the heating beams (NBI1) at local pitch angles with the toroidal magnetic field between 30 and 40 degrees. A drawing of the NB injec-

¹Most of the contents of this section has been published in [Rev. Sci. Instr., Vol. **79**, 10E522 (2008)] in a modified format

tion geometry is displayed in fig. 2.14 with the TEXTOR CXRS viewing geometry indicated. The viewing geometry has a strong effect on the analysis of the MSE spectrum (see chapter 2 and 3), but also effects the CX spectra of anisotropic ion populations, such as fast ions originating from neutral beam heating. The angles between the lines of sight and the magnetic field of the ITER-pilot diagnostic on TEXTOR are nearly the same as the pitch angles at birth of ions injected by a second neutral beam (NBI2), injected counter to the direction of NBI1, at the other side of the torus. This viewing geometry allows to be sensitive to the slowing down spectrum of NBI2 ions on the blue wing of the D_α spectrum while the BES spectrum is measured on the red wing of the spectrum.

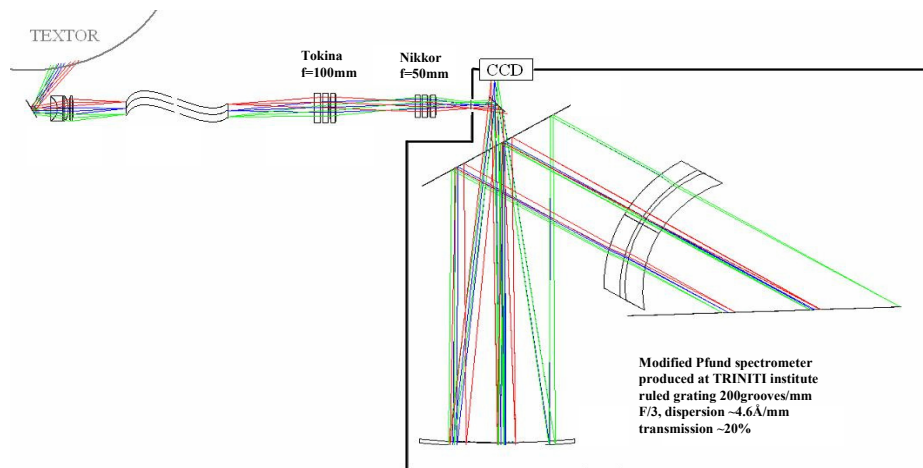


Figure 4.1: ZEMAX model of the TRINITY spectrometer used for the fast ion D_α CX measurements on TEXTOR. A band pass filter (not shown) is placed between the two lenses.

The collected light is guided through optical fibers to a high etendue, high resolution spectrometer ($F/3$, $A\Omega=6.2 \cdot 10^{-3} \text{ mm}^2\text{sr}$ per radial channel, $f=480\text{mm}$, dispersion= $4.6\text{\AA}/\text{mm}$). The Echelle grating is used in 13th order and a bandpass filter ($\lambda_0=6561\text{\AA}$, $\Delta\lambda=200\text{\AA}$) blocks light outside the relevant wavelength range that could overlap with the D_α spectrum at different orders. The slit of the spectrometer has been set equal to the width of the image of the fibers in order to maximise the etendue whereas the instrument function can still be satisfactory modelled with a sum of 3 gaussians with a total FWHM of only 1.4 \AA . A simplified sketch of the spectrometer layout is shown in fig. 4.1.

The spectra are read out with a low noise (11.6 e^- -rms), high quantum efficiency (QE=90%) PIXIS400B ccd camera from Princeton Instruments. This ccd has a large chip which allows to record a spectral range of 120\AA . A mechanical shutter is used during the read out period of the camera, which limits the time resolution to 80ms with an effective exposure time of 40ms. The intense D_α line (656nm) from excitation of cold atoms near the wall can saturate the detector, but illumination

with intense lines from a neon gas discharge lamp show that the charge leakage between pixels on the ccd is negligible.

The fiber bundle can be removed from the periscope which guides it into the vessel without breaking the vacuum in order to routinely perform a calibration between radial channels and along the length of the ccd chip, necessary for the quantitative study of broad spectral features. These calibrations are performed with an integrating sphere calibration lamp yielding an optical transmission of 8.5% (assuming the calculated value from the etendue of the spectrometer is correct). During an opening of the vacuum chamber the last mirror, vacuum window and periscope optics have been separately calibrated yielding a transmission of 32%.

4.2.2 Sample Data

Before proceeding to the modelling and interpretation of the spectra, we first show some sample data in fig. 4.2. Four spectra are shown, an ohmic reference spectrum, a spectrum during injection of NBI1 or NBI2 only, and a spectrum during simultaneous injection of NBI1 (counter- I_p) and NBI2 (co- I_p). On the ohmic spectrum, there is no active charge exchange data and no fast ions, the background is flat. During injection of NBI1 only, one can see the active charge exchange emission on thermal ions, but there are no fast ions moving towards the observer on the blue wing of the spectrum. During injection of both beam simultaneously, one can see the active charge exchange emission of fast ions injected by NBI2. The deuterium slowing down spectrum (in inlay) has usually a similar or lower intensity than the Bremsstrahlung on TEXTOR. The active CXRS slowing down spectrum is also contaminated by impurity lines from low ionisation stages of mainly C and O. Passive charge exchange (PCX) between fast ions and thermal neutrals from the wall has been observed. Therefore a non-localised fast ion related signal in the energy range 15-50keV can sometimes be observed during high power NBI2 heating without NBI1 acting as a probing beam. In first instance we will neglect this feature, but discuss it later (section 4.2.4). No D_α related signal from neutrals moving towards the observer has so far been seen above approx. 15 keV during ohmic shots or when only NBI1 is injected. A possible approach to eliminate all spectral features that are not induced by the probing beam is fast beam modulation (much faster than the slowing down time) [42]. For technical reasons this is not achievable on TEXTOR due to the long read out time of the ccd cameras and constraints on the beams. An alternative approach is modelling of all non-active features in the spectrum, making use of the high S/N ratio of the TEXTOR CXRS spectra and the good spectral resolution which allows to resolve the parasitic impurity lines. In Fig. 4.3 a similar set of spectra is plotted on an energy axis (the Bremsstrahlung, taken equal to the continuum at energies much larger than the beam injection energy, is subtracted). When the NBI2 injection energy is changed from 30keV (blue crosses) to 51keV (red diamonds), the change of the 'step' in the spectrum (the onset of the D_α slowing down feature at the injection energy) can easily be seen.

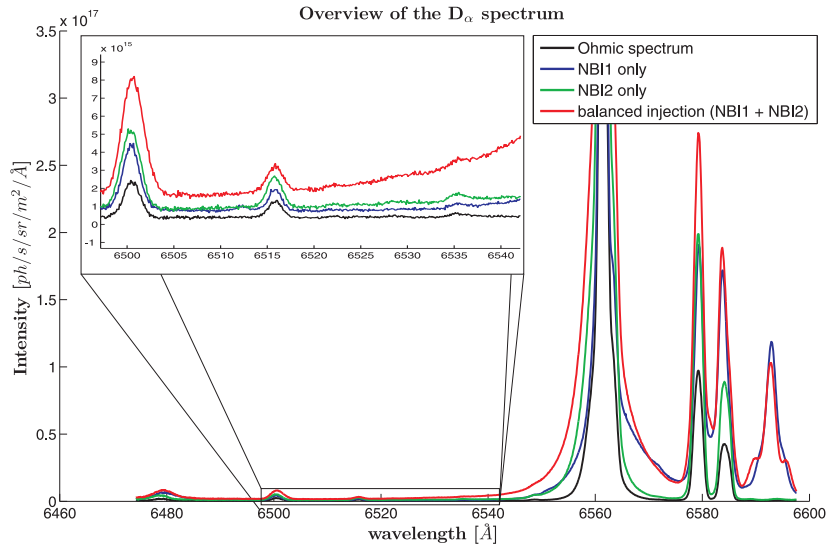


Figure 4.2: The full D_α spectrum is shown (black) for an ohmic plasma, (blue) a plasma with only the probing beam (no fast ions moving towards the observer), (green) a plasma during injection of NBI2 with ions moving to the observer but without active CX signal and (red) with both beams. In the inlay the signal in the fast ion relevant wavelength range is shown. A part of the BES spectrum (from 658nm to 660nm, overlapping with a CII multiplet) is seen on the red wing of the D_α line (656nm).

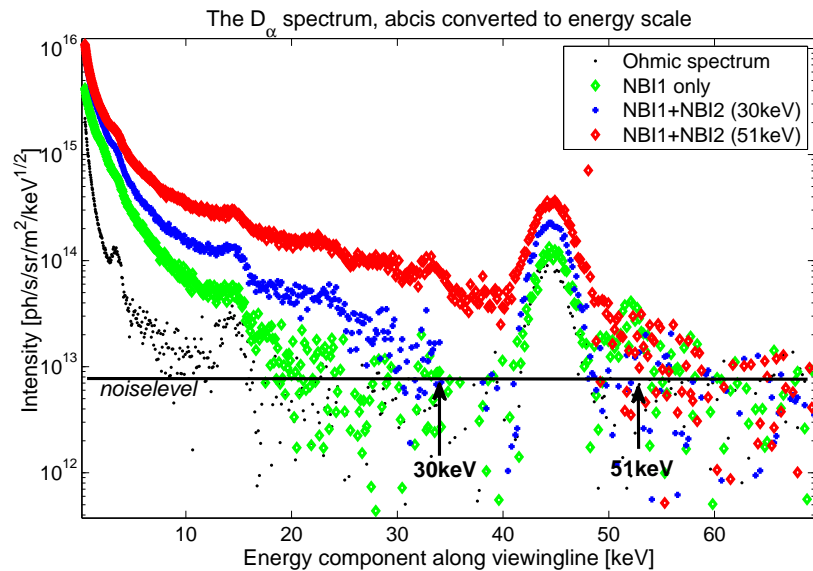


Figure 4.3: Spectra for different acceleration voltages in NBI2 (Bremsstrahlung subtracted). The injection energy is changed from 30keV (blue) to 51keV (red). An ohmic spectrum (black) and spectrum with only NBI1 (green) are given as reference. Impurity lines overlap with the fast ion spectrum at 15, 22, 32 and 45keV.

4.2.3 Modelling and Interpretation

The modelling aspects needed to extract the fast ion density from the raw data cover both the modelling of the passive spectra (Bremsstrahlung, impurity lines and possibly passive charge exchange) as well as the modelling of the active fast ion spectrum itself.

First, in order to obtain information about the position and widths of all the impurity lines, a time averaged passive spectrum (without NBI1) is fitted. The positions and widths of the low intensity lines that are obtained this way can be used as initial values or fixed when fitting the active beam phase of the discharge (although not all the impurity lines are identified, we assume no active charge exchange lines or emission from high ionisation stages from the rotating core plasma). All parameters concerning the brighter lines can be left free. Passive charge exchange is neglected.

As a second step in the analysis, the spectral shape of the slowing down spectrum is assessed in order to obtain a model to fit to the data. The slowing down of fast ions in plasmas is described by the Fokker-Planck (FP) equation. We have used an analytical steady state solution to the Fokker-Planck equation for neutral beam injected ions (eq. 4.1), valid at energies close to the injection energy [115, 116]. ζ is the pitch ($\zeta = v_{\parallel}/v$), τ_s is the slowing down time, S is the fast ion birth rate, ζ_0 is the pitch at birth, v_c is the critical velocity ($= (3/4\pi^{1/2}m_e/m_i)^{1/2}v_e$) and α describes the pitch angle scattering (mainly a function of T_e) [116].

$$g(v, \zeta) = \frac{\tau_s S}{4\pi(v^3 + v_c^3)\sqrt{\pi\alpha}} \exp - \frac{(\zeta - \zeta_0)^2}{4\alpha} \quad (4.1)$$

An example of the modelled slowing down function for TEXTOR as a function of velocity and pitch is shown in fig. 4.4. One can see the initial velocity and pitch of the beam ions and the spread in pitch angle as the ions slow down in the plasma. The beam ion velocity distribution function is first normalized in velocity space ($g_n(v, \zeta)$) and hence becomes independent of the source rate. $g_n(v, \zeta)$ is then multiplied with the velocity dependent charge exchange emission rates [31, 24]. From the resulting emissivity only the projection on a line of sight is retained to give the expected spectral slowing down feature (eq. 4.2). v_{col} is the collision velocity between the fast ions and the neutrals in the beam and v_{los} is the component of the fast ion velocity along a line of sight.

$$f^{FP}(\lambda \equiv \lambda_0 + \frac{v_{los}\lambda_0}{c}) = \int \int dv d\zeta g_n(v, \zeta) v^2 \times \int d\phi Q_{CX}(v_{col}) \delta\left(\frac{\mathbf{v} \cdot \mathbf{v}_{los}}{v_{los}} - v_{los}\right) \quad (4.2)$$

In fig. 4.4, the part of the velocity distribution function that contributes to the measured signal at a certain Doppler shift is shown as the area within each of the black curves. For the TEXTOR case we are only sensitive to ions from NBI2 on the

blue wing of the D_α spectrum.

In a third step, in order to be able to obtain quantitative information on fast ion density profiles, the local neutral density of the beam which is used as diagnostic beam needs to be known along each line of sight. Instead of calculating the beam attenuation, we have used the intensity of the beam emission spectrum to obtain the beam density (see chapter 2 and 3 for details). This method does not only reduce artefacts concerning attenuation of the probing neutral beam but also the uncertainties in the absolute calibration and alignment with the beam. For the TEXTOR spectra using the ITER-pilot viewing geometry the BES spectrum is recorded on the red wing of the D_α spectrum. The slowing down feature which is then fitted against the data thus takes the form of eq. (4.3). The right hand side of eq. 4.3 is evaluated for every energy component in the beam j that deposits the fast ions and summed over every component in the beam k that is used as a diagnostic. I_k^{BES} is the beam emission intensity of the k th energy component in the diagnosing beam and Q_k^{BES} is the effective beam emission rate (see chapter 3 for a discussion).

$$I_{\text{fast}}^j(\lambda) = \sum_{k=E,E/2,E/3} \frac{I_k^{\text{BES}}}{n_e Q_k^{\text{BES}}} f_{k,j}^{\text{FP}}(\lambda) \quad (4.3)$$

In a final step, the expected spectral features (eq. 4.4) are fitted to the experimental data. The free parameters are the fast ion densities (α_j), the intensities of the impurity lines and the continuum background. A typical result of the fit is shown in fig. 4.5.

$$I(\lambda) = \sum_{j=E,E/2,E/3} \alpha_j I_{\text{fast}}^j(\lambda) + I_{\text{imp}}(\lambda) + I_{\text{brems}}(\lambda) \quad (4.4)$$

When fitting the slowing down spectra, the information contained in the spectra is reduced to the fast ion densities over a rather broad area of velocity space. Nearly all energy resolution is lost. Partly, this is intrinsic to fast ion charge exchange spectroscopy, the projection on a line of sight and convolution with the velocity dependent charge exchange cross sections (eq. 4.2) smoothens the measured spectrum. A further loss of energy resolution of the D_α CX spectrum arises from the motional Stark effect. The neutralized fast ions are moving at high velocity in a magnetic field, so they experience a Lorentz electric field in their rest frame, just like in case of the neutral beam emitted MSE spectrum. The line splitting gives rise to a broadening of the spectrum. This effect has been neglected in the calculation of the spectral shape for TEXTOR (eq. 4.3), but would further reduce the energy resolution by a few keV. This insensitivity of the spectral shape to changes in $g(v, \zeta)$ has been observed at TEXTOR. Fast ion charge exchange should therefore mainly be considered a diagnostic to give information about the total fast ion density rather than a diagnostic to measure changes in the pitch angle or velocity distributions.

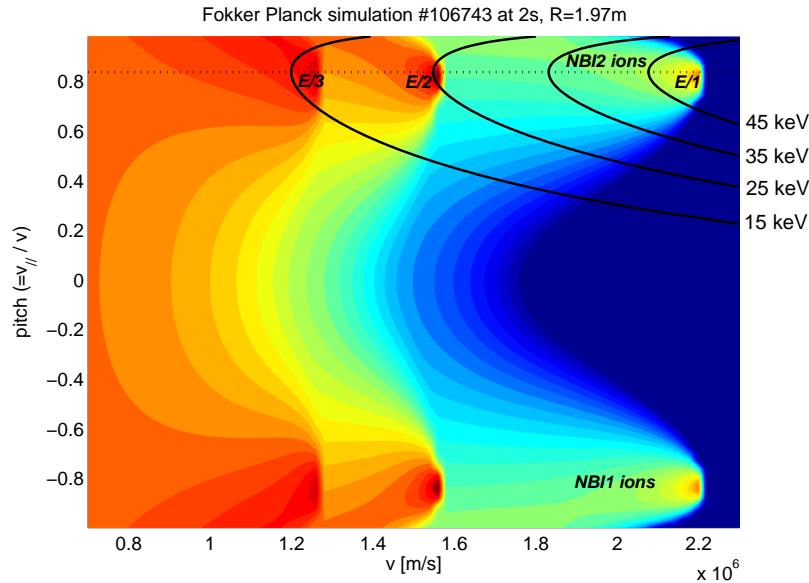


Figure 4.4: Fokker-Planck simulation [115] for a TEXTOR pulse with both beams injected. The beams are nearly identical but the pitch has opposite sign. The dashed line indicates the pitch of a CXRS line of sight. The full curves enclose the area of velocity space that can contribute to the measured signal at specified energies. Within each of these regions the weighting factors are inhomogeneous (see [31, 45]).

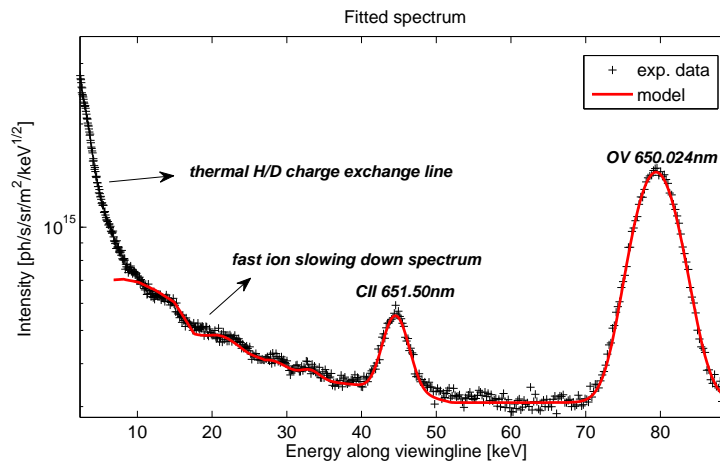


Figure 4.5: Fitted spectrum. In order to determine the intensity of the slowing down spectrum, the impurity lines and Bremsstrahlung must be fitted simultaneously with the synthetic slowing down spectrum from the FP model. Wavelength axis is converted to energy scale. The other lines seen in the D_α slowing down tail are impurity lines.

4.2.4 Passive charge exchange emission

In the preceding sections measurements of a tail in the D_α CX spectrum from TEXTOR have been shown to originate from neutral beam injected ions and a method

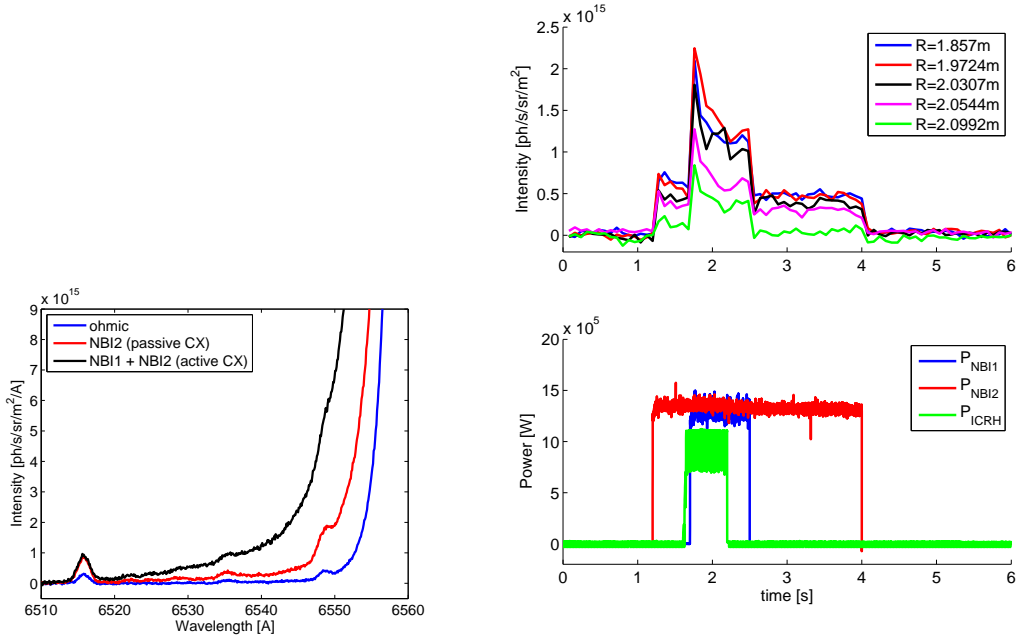
for analysis has been proposed. For the localisation and quantitative interpretation of this data, we have neglected passive charge exchange (PCX), i.e. CX between fast ions and less energetic neutrals that do not directly originate from the NB that is used as probing beam. Unfortunately, this assumption was too optimistic. In fig. 4.6(a) a spectrum with only NBI2 (fast ion source, creating a PCX blue shifted fast ion CX signal) is compared with the ACX+PCX signal when both NBI1 and NBI2 are switched on. An ohmic spectrum is shown as reference. In fig. 4.6(b) the spectral intensity that corresponds to fast ions moving along a line of sight with an energy of 30 to 40keV/amu is plotted as a function of time. No fast ion signal is recorded when NBI2 is switched off, as it should be. When only NBI2 is on, we see a PCX component with an intensity of about 30% of the intensity of the active+passive spectrum when both beams are injected.

The problem of the passive emission is also encountered on 'classical' CX spectroscopy on C^{6+} , but in the case of CX spectroscopy on thermal ions, one can make use of the advantage that most of the PCX signal comes from the plasma edge where the temperature and plasma rotation is low. Therefore, one can use the difference in spectral shape to model the PCX component. In case of fast ion CX spectroscopy, the spectral shape of the PCX component is nearly the same as the one of the ACX component and also stretches to the injection energy of the beam. This limits the prospects to separate the ACX and PCX contribution based on modelling. The option of using fast beam modulation or lines of sight that do not intersect the neutral beam seems therefore the only option to remove the PCX emission from the localised active component. However, fast beam modulation is not possible due to the long readout time of the ccd cameras that are available at TEXTOR and limitations on the neutral beam power supplies. Installing passive fibers with exactly the same viewing geometry, but not intersecting the beams, is the most promising option. Instead of obtaining the information about the passive emission from fitting a frame before the shot, one could analyse a passive frame and also derive the passive fast ion emission from this, if the assumption that the PCX emission is toroidally homogeneous is valid.

We have sought for situations in which the PCX emission is low enough that it can be neglected, but no such data was found. In chapter 5.3 the beam modulation technique is employed, using the first frame after switch off of NBI1, but with NBI2 still on.

4.3 Test of fast ion charge exchange spectroscopy on JET

The possibility to measure fast beam ion densities has been pioneered at JET by von Hellermann et al. [31], measuring the slowing down of helium injected by the neutral beams. In this section we explore the possibility to measure a more commonly present fast deuterium population with CXRS at JET with the existing CXRS lines of sight and spectrometers. The possibility to measure fast beam ions depends on



(a) Blue wing of the D_α spectrum with and without beams, Bremsstrahlung is subtracted. In the spectrum with NBI2 but without NBI1, one can still see some charge exchange signal originating from fast ions that is not driven by neutrals from NBI1.

(b) Intensity of the D_α spectrum (Bremsstrahlung subtracted) between 651.9nm and 652.5nm (corresponding to 30 to 40keV/amu along a line of sight). Also shown are the NBI1 and NBI2 beam power and the ICRH power time traces. Typically 20-30% of the fast ion CX signal in this energy range is passive.

Figure 4.6: Illustration of passive fast ion CX (TEXTOR #106743).

both the NBI and CXRS geometry and the optical throughput of the diagnostic. There are two neutral beam banks at JET, each containing 8 beams, of which 4 are injected 'radially', intersecting the magnetic axis at an angle of approx. 65 degrees and 4 are injected 'tangentially' at an angle of approximately 52 degrees with the magnetic axis. All beams are injected in the same direction, co-current in standard configuration. This implies that the beam emission spectrum will always be measured on the same wing of the D_α spectrum as where the fast ion feature is expected. This can be overcome by looking perpendicular to the beam or one could look at higher energies, at wavelengths corresponding to Doppler shifts beyond beam emission.

Several sets of fibers (see fig. 4.7) looking to the neutral beams are connected to tunable spectrometers and have been used to record spectra to test the application of the technique using the existing hardware. There are two optical periscopes on JET that look to the octant 8 beams that are situated in the equatorial plane, one is looking from octant 1 (fibers connected to a spectrometer called ks5c) and the other

from octant 7 (called ks5a). The beam emission Doppler shift is relatively large, but it is still possible to resolve fast ions with tangential velocities corresponding to more than 35 keV/amu. There is a single l.o.s. looking through all octant 8 beams from the top of the vessel (connected to a spectrometer called ks5b), the BES Doppler shift is zero along this line of sight and this viewing geometry could potentially be used to measure fast ions with a large perpendicular velocity. Unfortunately, because this line of sight is looking down towards the divertor, the background of the spectrum where we expect to see the fast ions is much more polluted by small impurity lines and the fast ion feature is difficult to extract. The poloidal charge exchange viewing geometry (called ks7a) has the best geometry to see fast ions that have not undergone a lot of pitch angle scattering yet. On the set of sample data collected at JET however it was very difficult to interpret the continuum beyond the wings of the D_α spectrum, probably due to a rather small flat field of the spectrometer which causes a strong inhomogeneous calibration along the length of the ccd chip. Therefore, the best data that unambiguously show a slowing down spectrum were recorded with ks5c. Fig. 4.7 contains an overview of the pitches (v_{\parallel}/v) of the available lines of sight, neglecting the poloidal magnetic field. The highest sensitivity to beam injected ions will occur on the redshifted wing of the ks7a D_α spectrum, the blue shifted ks5a and red shifted emission on ks5c could also be used.

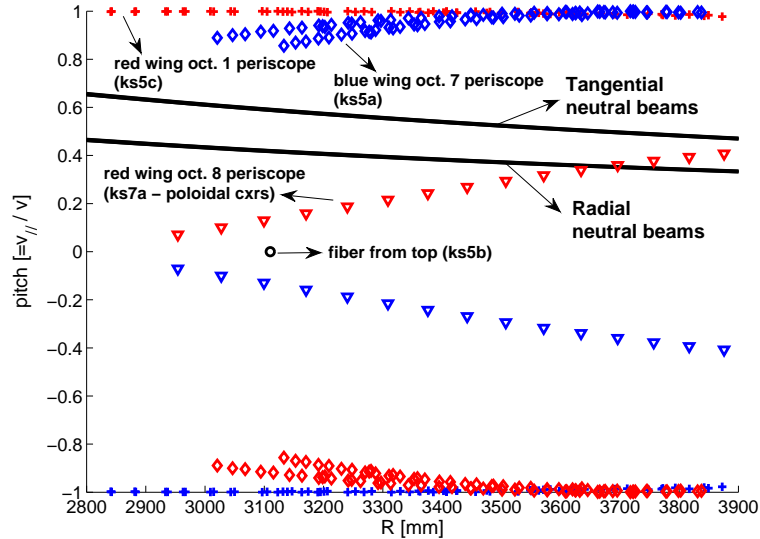


Figure 4.7: Pitch of the neutral beams and the lines of sight on which a fast ions charge exchange signal could potentially be seen, in the assumption of a purely toroidal magnetic field. Symbols in red indicate red shifted fast ion CX spectra, and blue symbols indicate blue shifted CX spectra.

In fig. 4.8 an example fast ion spectrum from JET is shown from the ks5c spectrometer which is the standard spectrometer used for core charge exchange

spectroscopy. A tail in the spectrum is seen beyond the beam emission spectrum. Beam emission stretches up to an equivalent energy of about 35keV. The fast ion spectrum goes up to approximately 80 keV and is then obscured by a broad emission line. The injection energies of the beam are shown in the table at the right. The horizontal line shows the Bremsstrahlung offset, taken as the average of the signal at energies beyond the highest beam energy. An ohmic spectrum is shown as reference to the spectral shape without beam generated spectral features. The fast ion tail in this spectrum is quite clear, but the spectrum has been averaged over about 900ms (the data was recorded at a time resolution of 10ms). Between 39 and 71 keV, no impurity lines are visible and the signal has been binned in two energy groups indicated by the vertical lines in fig. 4.8. The Bremsstrahlung has been subtracted in order to obtain a signal which is proportional to the fast ion density. The time traces of the signal obtained this way is plotted in fig. 4.9 for each of the energy bins for 2 shots: #72313 and #72351. The injected NB power is similar for both shots, but the electron density is approximately a factor 2 higher for #72351. For the lower density shot (fig. 4.9(a)) the binned fast ion signal has a signal to noise ratio of about 5 for the lowest of the two energy bins and about 2 for the highest energy bin. The CX fast ion intensity shows a clear correlation with the neutron rate. For the higher density shot (fig. 4.9(b)), the signal to noise ratio drops to about 1. This deterioration of the signal of noise ratio with density is expected because the fast ion CX intensity is proportional to both the fast ion density which is inversely proportional to the electron density for a given source rate and to the local neutral beam density which is lower in the core at high plasma density because the beam is more attenuated. The photon noise from the Bremsstrahlung increases proportional to the electron density.

In conclusion, the feasibility to use charge exchange to measure the beam ion density profiles on JET is limited by the signal to noise ratio. Useful fast ion data could be obtained at wavelengths corresponding to Doppler shifts beyond beam emission looking from the equatorial ports. No unwanted emission has been seen at this wavelength range for the equatorial viewing geometry, except during ELM crashes. During an ELM the background in the spectrum suddenly increases, even at very high energies. This could be due to scattered emission from the bright cold D_α line.

4.4 Discussion and conclusion

Charge exchange between beam neutrals and fast ions injected by the neutral beams has been detected by charge exchange spectroscopy on TEXTOR and JET. Variation of the beam voltage on TEXTOR makes the origin of the fast ion signal unambiguous. The spectral shape of the fast ion spectrum corresponds to the expected shape which has been calculated based on an approximation of the fast ion slowing down function and a convolution with the charge exchange emission rates.

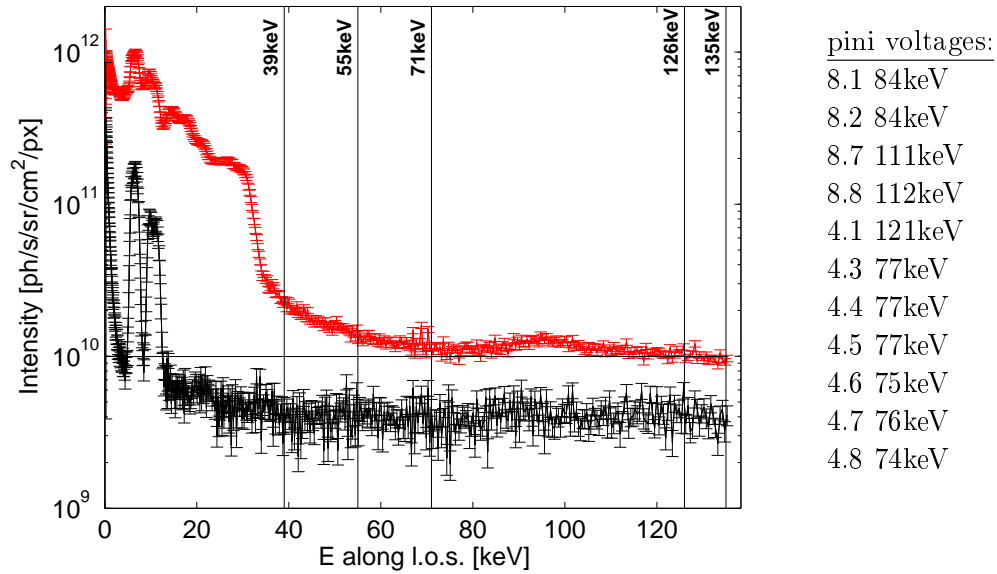


Figure 4.8: Red wing of the D_α spectrum from JET (ks5c, #72313). In red an averaged spectrum (46.4s to 47.3s) during NB operation, in black a reference in the ohmic phase before NB injection. The wavelength axis (Doppler shift) is converted to the equivalent energy along a l.o.s.. The voltages of the beams are indicated in the table. There is a broad impurity line obscuring the fast ion spectrum around 100keV. The vertical bars indicate the signal that has been used to obtain the time traces in fig. 4.9. Between 128 and 135keV, there is no fast ion signal anymore and the continuum in this wavelength range has been used to determine the Bremsstrahlung background.

A method to obtain fast ion density profiles from fitting of the fast ion spectrum and taking into account the beam emission intensity which is observed on the same spectrum, is proposed.

However, the application of the method to study the fast ion transport and confinement is limited by the pollution of the signal by passive charge exchange between background neutrals and fast ions on TEXTOR and by the limited signal to noise ratio obtained on JET due to the lower optical throughput. A faster ccd camera is proposed for the TEXTOR diagnostic, which would allow to use beam modulation in order subtract the fitted passive emission.

A preliminary analysis using subtraction of the passive emission after switch off of the diagnostic beam is used to derive fast ion density profiles on TEXTOR in section 5.3 in chapter 5.

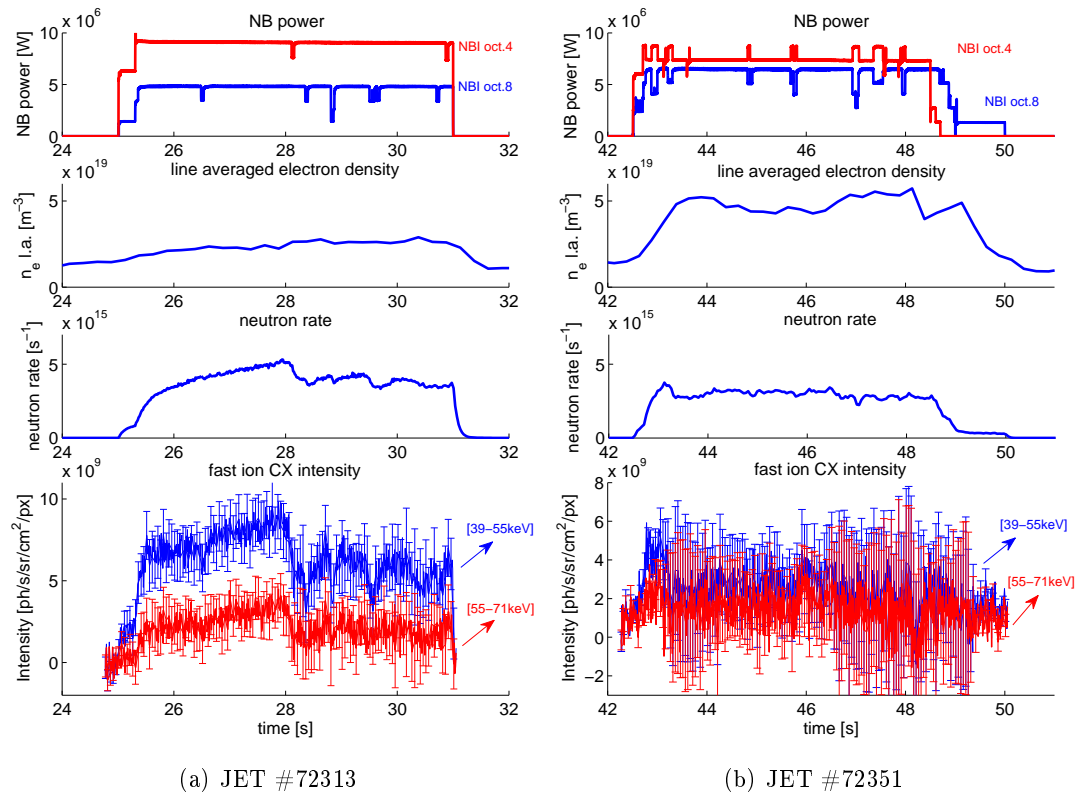


Figure 4.9: Time traces for two JET discharges with similar beam power: one at a relatively low density of $2-2.5 \times 10^{19} m^{-3}$ and one at higher density of about $5 \times 10^{19} m^{-3}$. The fast ion CX intensity drops drastically with electron density.

Applications of beam emission and fast ion charge exchange spectroscopy

Contents

5.1	Introduction	81
5.2	Measuring the helium density with active beam spectroscopy	81
5.2.1	Motivation	81
5.2.2	Helium concentration measurements from combined beam emission and charge exchange spectroscopy	82
5.3	Fast ion density profiles from charge exchange spectroscopy	83

5.1 Introduction

In chapters 2-4, the importance of beam emission to measure absolute impurity concentrations was emphasized, especially in view of the high beam penetration on ITER. In the first section of this chapter, we try to validate this technique on TEXTOR helium concentration measurements. In the second section we apply the CXS/BES technique to fast beam ion spectra on TEXTOR.

5.2 Measuring the helium density with active beam spectroscopy

5.2.1 Motivation

The main motivation for the quantitative assessment of beam emission is the measurement of impurity concentrations from the combination with CXRS, as outlined in the introduction to this thesis and in chapter 3.

We have implemented a diagnostic combining BES and CXRS on TEXTOR, resembling the CXRS diagnostic for ITER [54]. A similar diagnostic setup is being commissioned on Alcator C-Mod [117]. Both carbon and helium concentration profiles have been measured on TEXTOR. The main aim of the experiments was to check the atomic data involved and the cross calibration procedure based on Bremsstrahlung

as proposed for ITER. A study of helium exhaust using the CXRS/BES data is described in [118]¹. It is difficult to benchmark the absolute values of the measured impurity concentration as there are no other diagnostics capable of providing the same data. A comparison between Z_{eff} from the CXRS carbon concentration and Bremsstrahlung is possible, but this does strongly depend on the accuracy of the intensity calibration of the Bremsstrahlung as well as on the assumption that carbon is the dominant impurity contributing to Z_{eff} . In the next section the measured helium density is benchmarked against the electron density rise during a strong helium gas puff. Measuring the helium concentration by injecting a hydrogen beam in a pure helium plasma is another method to check the accuracy of the analysis, but it has been proven very difficult to produce a helium plasma of sufficient purity on TEXTOR.

5.2.2 Helium concentration measurements from combined beam emission and charge exchange spectroscopy

A strong helium gas puff has been injected in TEXTOR during the flat top of discharge #103357. The helium is injected at 2s during 250ms and the line integrated density rises from 1.83 to 2.75 10^{19} m^{-2} . The density was relatively stable before the injection and the deuterium gas valve was closed, i.e. pumping was balanced by external deuterium injection via the beams and recycling at the wall. Some remaining helium from previous discharges is present before the gas puff. If we assume that hydrogen pumping and feeding by the beam remains unchanged during the length of the gas puff, then the rise of the total number of electrons in the discharge can fully be attributed to the injected helium and the measured rise of the helium density should be half the electron density rise.

The D_{α} beam emission and the helium $n=4-3$ charge exchange spectra have been measured along the lines of sight of the toroidal CXRS diagnostic (see chap. 2 and 4). The light has been split by a dichroic beam splitter to allow simultaneous measurement of BES and CXRS along 8 lines of sight. The CXRS spectra have been analysed by the fitting codes which are briefly described in chapter 2. No external intensity calibration could be performed on this setup as this requires an opening of the machine, but the intensity of the Bremsstrahlung, which is observed as a continuum background on the spectra, has been used to perform a relative calibration between the two spectral bands. A high density ohmic discharge (#103366) was chosen to have a high brightness and to avoid contamination of the background on the beam emission spectra by D_{α} emission from fast ions. For #103366, the observed continuum behaves as expected, following the n_e^2 scaling of the Bremsstrahlung, unlike many discharges that show contamination of the 656nm band by black body radiation. A mechanical shutter was placed in front of the fibers to avoid smearing during read out of one of the cameras. An inaccurate synchronization with the other

¹The helium concentrations in [118] have been derived using the beam emission rates and excited beam population for the effective CX rates from Anderson et al. [88] instead of the updated rates from chapter 3

camera, used for beam emission, resulted in an approximately 15% modulation of the BES intensity which was corrected using the time stamps of the spectra, but a slight remaining modulation can still be seen on the BES data. Once the BES and CXRS intensities have been obtained and a relative calibration been performed, the helium concentration can be calculated using eq. 2.4 (chap. 2). Because the beam emission rate and the $n=2$ population, which is needed to construct the CX rate, depend on the impurity concentrations, the calculation is iterated till convergence.

The measured number of helium atoms in the plasma during the gas puff is shown in fig. 5.1 with the total number of electrons. The helium density profiles have been extended to the edge assuming a constant concentration from the last point onwards. Only taking into account the data within the area where we have measurements did not change the final results. The helium density has been integrated over the whole plasma volume to avoid possible profile effects linked to a difference in transport between He^{2+} and D^+ . Selective ion transport could locally violate the assumption that the deuterium density remains unchanged during the gas puff. The helium injection gives rise to an increase of the measured helium content by $4.03 \cdot 10^{19}$, while the expected increase based on the rise of the total electron content of the plasma is $3.33 \cdot 10^{19}$, giving an estimated error on the measured helium density of 17%. Note that we have not drawn error bars on the CXRS/BES helium density. This is because the statistical error bars from fitting the spectra are negligible compared to the possible systematic errors induced by the atomic data that we were after on the one hand and possible inaccuracies in the relative calibration due to non-Bremsstrahlung contribution to the continuum on the other hand.

The a priori uncertainty on the CXRS and BES rates is usually estimated at 20%. Although this is not more than an educated guess, it is consistent with our experiment, from which we conclude that the assumed accuracy of the beam emission and helium charge exchange rates is justified.

5.3 Fast ion density profiles from charge exchange spectroscopy

As mentioned before in chapter 4, a routine application of fast ion charge exchange spectroscopy to obtain fast ion density profiles from the high energy tail in the D_α CX spectrum on TEXTOR is mainly hampered by passive CX emission between fast ions and background neutrals. We have tried to mitigate this effect by subtracting the first frame after the neutral beam that is used as diagnostic beam (NBI1) is switched off, from the spectra just before the end of the NBI1 heating phase. The switch off of NBI1 changes the plasma parameters and hence also the passive CX intensity (20-30% of total fast ion intensity) during and after the NBI1 heating phase could change due to a change in the penetration length of neutrals from the wall.

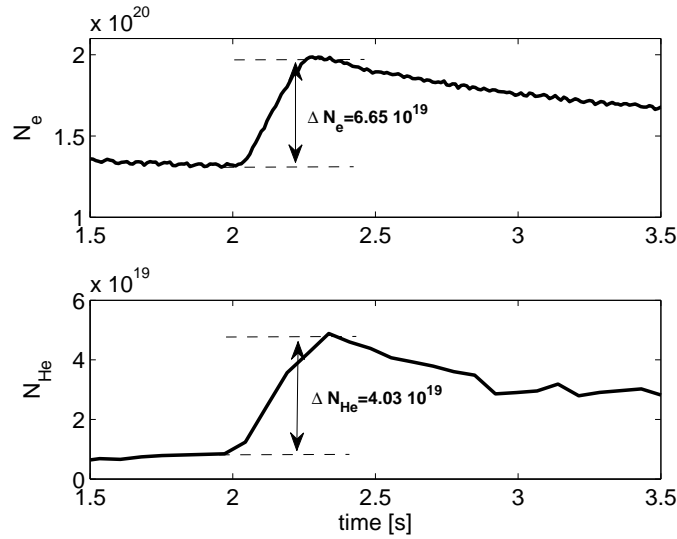
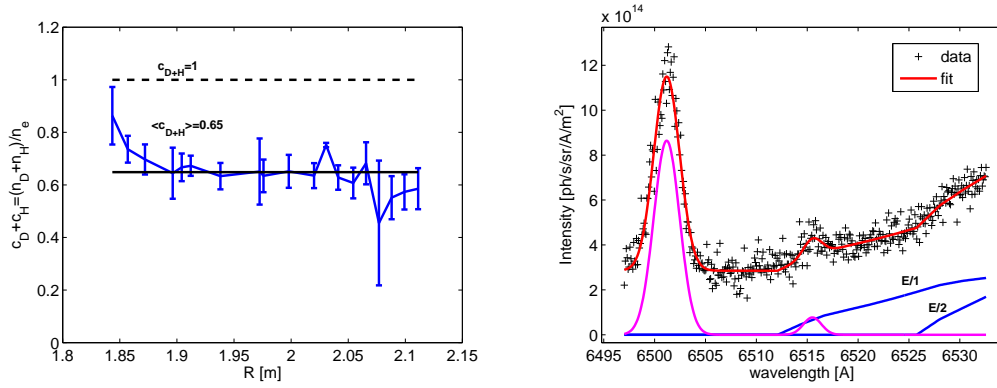


Figure 5.1: Rise of the integrated electron and helium density during an intense helium gas puff (TEXTOR #103357). The hydrogen gas valve is closed during the helium injection. If selective deuterium pumping is negligible during the length of the gas puff, the increase in the total electron density should be twice the increase of the helium density integrated over the plasma volume. The difference between the measured and expected helium density rise is about 20%.

However, we have neglected this for this specific time frame (TEXTOR #106743 at 2.4s) and applied the method outlined in sect. 4.2.3 to calculate the density profiles of the counter-current circulating fast ions from NBI2.

As a first step in the analysis, we have fitted the beam emission and thermal CX spectrum, neglecting the fast ion tail, and calculated the (uncalibrated) beam densities along the lines of sight. As a check on the use of beam emission and the D^+ and H^+ charge exchange rates, we have first calculated the thermal $H+D$ concentration, before applying the method to fast ions. The spectra have been fitted with BESFIT (see 2.4.2) using the ion temperature derived from C VI as initial estimate of the coupled D^+ and H^+ temperatures and leaving the $H/(H+D)$ -ratio as a free parameter. The $H/(H+D)$ -ratio cannot be reliably obtained from the data as it is very sensitive to distortions in the wings of the spectra such as cross section effects, motional Stark broadening and the presence of a, albeit small, fast ion tail and therefore only the sum of the H and D concentrations can be obtained from the fit. 3% carbon has been assumed in the calculation of the beam emission rates. The resulting c_{D+H} profile is shown in fig. 5.2(a). The dashed line represents a pure D/H plasma, while the average of the measured $H+D$ concentration profile is about 0.65. Assuming that carbon is the only impurity and the not accounted for beam ion population is 3% on average, a Z_{eff} of 2.5 would be required for charge neutrality. No reliable independent measurements of Z_{eff} from Bremsstrahlung were available, as the CXS plasma facing mirror was not absolutely calibrated, but a Z_{eff}

of 2.5 is reasonable for this type of high power discharge, giving confidence in the quantitative combination of D_α CXS and BES.



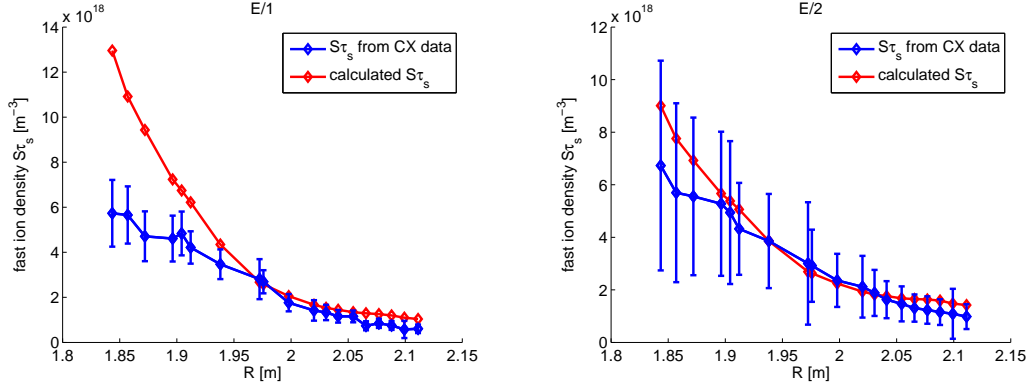
(a) Sum of the thermal D and H concentration from the thermal part of the D_α CX line and beam emission $c_{D+H} = \frac{I_{D+H}}{\sum_{i=E/1}^{E/3} I_{bes}^i Q_{cx}^i / Q_{bes}^i}$, as a check on the beam emission based analysis.

(b) Fit to the E/1 and E/2 component of the D_α fast ion tail from track 4 at 1.9m. Due to a decay of the electron density following the NBI1 switch off, some residual Bremsstrahlung and two impurity lines are still visible.

Figure 5.2: Thermal D+H concentration and fit to the fast ion part of the D_α spectrum for TEXTOR #106743 at 2.4s. Passive emission (the first frame after the switch off of NBI1) has been subtracted before the analysis.

As a second step in the analysis, the fast ion spectrum is fitted according to the procedure described in sect. 4.2.3. We calculate the expected velocity distribution function $g(v, \zeta)$ for fast beam ions (eq. 4.1) as derived by W.G.F. Core [116] in which we put the product of the fast ion source rate and the Spitzer slowing down time equal to one, $S\tau_s=1$. The intensity of the fast ion spectrum will then be used as a fitting parameter corresponding to $S\tau_s$, which we will here call the fast ion density. An assumption on the shape of the velocity distribution function is needed in order to take the CX cross section effect into account. Due to the fact that CXS only measures a projection in velocity space, details on the pitch angle distribution are largely washed out, therefore we have set our goal at obtaining information about the beam ion densities from the overall intensity. The velocity distribution $g_n(v, \zeta)$ is multiplied by the D_α CX rate [24] with beam ions and projected on a line of sight (see eq. 4.2), largely following the procedure described by von Hellermann et al. [31]. This calculation has been checked by inserting a Maxwellian instead of the beam ion distribution to yield a gaussian emission line, normalized to one if Q_{cx} is also set to one. The resulting fast ion spectra (for each energy component in NBI1 and NBI2) are multiplied by the NBI1 densities along a line of sight from beam emission and summed in order to produce a spectral shape for each energy component in NBI2 that can be used to fit the experimental data (eq. 4.3). The subtraction of the first frame after the switch off of NBI1 has not entirely removed the impurity

lines and Bremsstrahlung and hence they need to be taken into account in the fit. The result of such a fit is shown in fig. 5.2(b). The fit is restricted to the E/1 and E/2 components as the E/3 component starts to merge with the thermal part of the CX line. The fast ion densities to which the fitted intensities are directly related are shown in fig. 5.3. The error bars are the purely statistical error bars from the fit.



(a) Fast ion density profile for the E/1 component (50-25keV). (b) Fast ion density profile for the E/2 component (25-17keV).

Figure 5.3: Fast ion density ($S\tau_s$) profiles derived from charge exchange data cross calibrated with beam emission and from a model based on the absence of radial transport and averaging of the fast ions densities over flux surfaces.

In a third step, to provide an interpretation of the measured $S\tau_s$, these are compared with the expected values in the absence of radial transport. The deviation between the modelled and measured profiles is therefore expected to yield information on the fast ion radial transport which is classically assumed to be very low. We cannot distinguish between a change in the local fast ion density and a, considerable, change in the pitch angle distribution that alters the projection of $g(v, \zeta)$ on the l.o.s., but we assume a change in density more likely than the latter.

The source rate is calculated with a neutral beam stopping code based on the CHEAP code that we have adapted to TEXTOR. The NB attenuation is calculated on a grid around the beam and the derivative yields the fast ion deposition². This is then binned on ρ assuming quadratically shifted circular flux surfaces and divided by the plasma volume represented by each of the ρ bins. The volume averaging is motivated by the fact that the TEXTOR beams are tangential and the injected particles are all passing at birth. The deviation between the flux surfaces and the fast ion orbits is neglected here. The source rates are multiplied by the Spitzer slowing down time $\tau_s \propto T_e^{1.5}/n_e$. The modelled $S\tau_s$ is also shown in fig. 5.3. Because there is no electron temperature available for this shot, the assumption

²The NB power fractions [E:E/2:E/3] = [0.57:0.30:0.13] have been used, consistent with beam emission and with the results obtained on the NB testbed [66], if multiplied with [1: $\sqrt{2}$: $\sqrt{3}$] and normalized

$T_e=T_i$ has been used. A comparison between shots with high D beam power from other campaigns show usually a higher T_i than T_e . Therefore the assumed T_e could artificially enhance the modelled fast beam ion density, especially for $R>2.05\text{m}$ the gradient in the ion temperature profile was reduced, which is usually not observed on the electron temperature profiles from Thomson scattering.

Bearing all considerations given above in mind, the most prominent difference between the measured and modelled beam ion density profiles is the stronger peaking of the modelled versus the measured profile. The total modelled fast ion density might be overestimated by too high a T_e , while the measured fast ion density profile has an uncertainty from the involved atomic data and possibly incomplete subtraction of passive emission. Nonetheless, the trends associated with these uncertainties are unlikely to explain the observed flattening of the fast ion profile. The steady state diffusion of fast beam ions ($D_{neo-classical} \approx 0.01\text{m}^2\text{s}^{-1}$ for the full energy component on TEXTOR [112]) is not effective enough to cause the observed flattening of the profile. A possible explanation is given by the redistribution of fast ions by sawteeth crashes as recently observed by collective thomson scattering on TEXTOR [119]. For this discharge the sawtooth inversion radius is between 1.9 and 1.95m. The time resolution of the CXS data (80ms of which 40ms exposure) is too low to resolve the sawteeth ($t_{st} \approx 20\text{ms}$) and hence we measure an average over several sawteeth periods.

In conclusion, the subtraction of the passive emission by beam modulation seems a promising method to obtain fast ion density profiles on TEXTOR, as illustrated by the analysis of the frames at the end of the NBI1 heating phase. As the power of the beams is rather high, the modulation should be fast enough ($< 10\text{ms}$) to avoid changes in the passive emission caused by changes in the main plasma parameters. For the results obtained in this section, the electron density during the passive measurements (80ms later) was already lower than during the phase with both beams on, this induces an uncertainty on the PCX component which is about 30% of the total intensity. Nevertheless, the CXS data show a remarkable flattening of the fast ion density profile compared to the birth profile.

Prospects of thermal and fast helium CXS measurements on ITER

Contents

6.1	Introduction	89
6.2	Thermal He CXS/BES concentration measurements on ITER	90
6.3	Fast helium CXS measurements on ITER	95

6.1 Introduction

The main motivation for this thesis is the validation of the CXS/BES technique that will be used to measure helium densities on ITER. In addition we have investigated the possibility to measure suprathreshold ions with CXS on TEXTOR and JET. In this chapter we will specifically focus on ITER and, through modelling of the CXS and BES spectra, set the accuracy that could be obtained on the thermal (sect. 6.2) and fast (sect. 6.3) helium concentration profiles.

The modelling used in the following two sections is to a large extent based on a CXS, MSE and fast ion CXS simulation package [120], initiated and developed by M. von Hellermann, FOM institute Rijnhuizen, that accounts for the NB attenuation, neutral beam and line of sight geometry, CX and BES emission rates, Bremsstrahlung background emission and the design parameters of a virtual spectrometer. For the modelling of the fast ion features, the code also calculates the α source rate and slowing down and takes into account the energy dependence of the CX cross sections. For the beam stopping and CXS and BES emission rates, atomic data from ADAS [24] is used. Poisson noise is assumed to be the dominant source of noise on the spectra and this determines to a large extent the statistical accuracy that one will be able to obtain on the thermal and fast helium CXS concentration profiles. Reflections on the inner wall of the tokamak are neglected.

As an input to the simulation code, plasma, beam and spectrometer parameters have to be supplied. Table 6.1 lists the reference ITER plasma parameters that

have been assumed in the modelling in the next two sections, as well as the most relevant neutral beam parameters and the expected performance of the ITER core CXS spectrometer.

<u>plasma parameters</u>	
$n_e=10^{20} (1-\rho^2)^{0.1} \text{ m}^{-3}$	$c_{He^{2+}} = 4\%$
$T_i=21 (1-\rho^2)^{0.8} \text{ keV}$	$c_{Be^{4+}} = 2\%$
$T_e=25 (1-\rho^2)^{0.5} \text{ keV}$	$c_{C^{6+}} = 1\%$
$v_\phi=200 (1-\rho^2)^{0.5} \text{ km/s}$	
<u>diagnostic neutral beam parameters (no modulation assumed)</u>	
$V=100\text{keV/amu}$	$P=3.6\text{MW}$
width \perp l.o.s.=0.19m	divergence 10mrad
<u>heating neutral beam parameters</u>	
$V=500\text{keV/amu}$	$P=17\text{MW}$
width \perp l.o.s.=0.19m	divergence 10mrad
<u>ITER core CXS diagnostic parameters</u>	
etendue $\varepsilon=1\text{mm sr}^2$	dispersion $d=2.5\text{\AA}/\text{mm}$
transmission $T=5\%$	slitwidth=1mm
QE detector=90%	

Table 6.1: Common input to the CXS simulations of sections 6.2 and 6.3. The chosen values reflect the operating conditions of ITER.

6.2 Thermal He CXS/BES concentration measurements on ITER

The accumulation of thermalized helium ash in the core of a burning plasma can strongly degrade the power output due to dilution of the DT fuel. In order to study the helium transport and exhaust on ITER, the requirements for the helium concentration measurements on ITER have been set to an accuracy of 10% at a time resolution of 100ms and with a spatial resolution of $a/10$ [7]. Charge exchange spectroscopy is the only diagnostic that can provide this information and therefore it is particularly important to know to which extent these requirements can be satisfied.

Despite being a well-established diagnostic, CXS on ITER will face the difficulty of a very low beam penetration to the plasma core due to the large minor radius of the machine and the high electron density. This problem can be overcome by using a higher beam voltage, but the CX rates drop fast as a function of energy. The trade off between a high local beam density and a high CX rate results in an optimum

beam voltage of approximately 100keV/amu, which is chosen as the design value of a dedicated diagnostic neutral beam (DNB), which will be operated on hydrogen. The analysis in this section is performed for lines of sight looking from upper port 3 to the DNB of which the most relevant parameters are listed in table 6.1.

The uncertainty analysis for CXS helium ash measurements, according to equations 2.4-2.6 of chapter 2, splits into two parts: statistical uncertainties related to the analysis of the spectral data (I_{cx} and I_{bes}) and systematic uncertainties from the involved atomic data (Q_{cx} , Q_{bes} and excited beam populations) and calibration. For the statistical uncertainties we have to model the spectra and simulate the fit that would be applied. This will be treated first. For the systematic part of the errors, we have to make a distinction between calculating (see eq. 2.5, chapter 2) or measuring (see eq. 2.6, chapter 2) the neutral beam density. This will be discussed later.

In order to obtain statistical error estimates on the CX and BES intensities, we have used the simulation package described in the introduction with the input listed in table 6.1 to obtain helium CX and beam emission spectra as well as the Bremsstrahlung continuum background. Poisson noise, i.e. gaussian noise on the detector signal corresponding to the square root of the number of photo-electrons, is added to the spectra to obtain a simulated set of spectra that resembles to our best knowledge the true spectra. The simulated data is fitted and the covariance matrix is obtained from the Jacobian of χ^2 at the fitted solution, which gives us the statistical uncertainties that will be encountered on ITER when fitting CXS or BES data. We have assumed no prior knowledge of T_i and Ω_ϕ . We have also assumed no relevant impurity lines in the wings of the helium spectrum other than the active CX lines of beryllium and a BeII emission line from the edge of the plasma. A simulated spectrum, with the active lines indicated, is shown in fig. 6.1. The ion temperature and rotation of the HeII and BeIV lines is coupled. Note the high Bremsstrahlung intensity which is responsible for most of the photon noise on the spectrum.

We have plotted the statistical uncertainties that are to be expected from fitting the helium CX and BES spectra in fig. 6.2. The predicted uncertainty on the helium CX and beam emission intensity is well below 10% over the entire radial range. This is not surprising as the etendue of 1mm²sr was chosen to meet the 10% accuracy criterium, but there is not much room for e.g. degradation of the mirrors or fibers if sufficient accuracy is to be obtained close to $\rho=0$. The errors on the beam emission intensity are negligible compared to the errors on the CX intensity because of the high intensity of the beam emission components (beam emission is an increasing function of beam voltage).

Predicted S/N ratios on the spectrum and statistical error estimates¹ for the required parameters to be measured by the core CXS diagnostic have also been published in

¹In [120], the 95% confidence interval ($\approx 2\sigma$) is used, here we use 1σ uncertainties. The input for the modelling is slightly different.

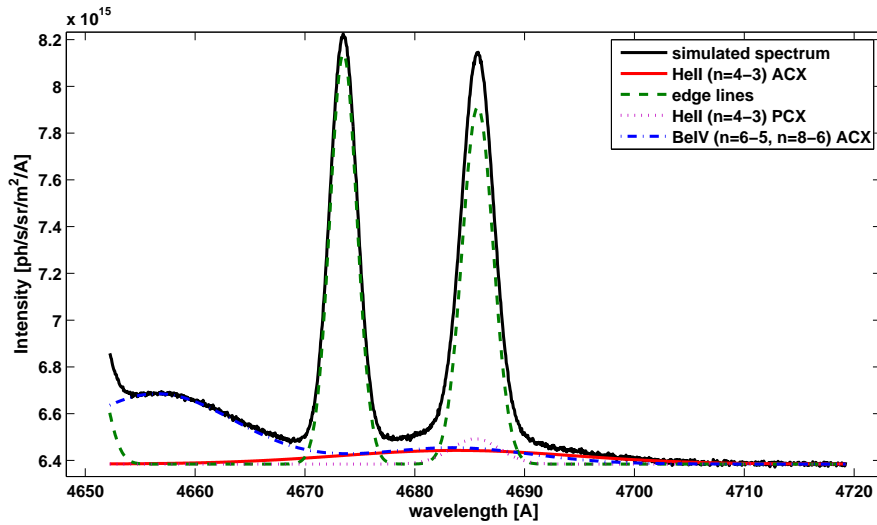


Figure 6.1: Simulated HeII/BeIV CX spectrum for ITER, looking from upper port 3 at the DNB at $\rho=0.3$. Plasma and beam parameters are listed in table 6.1.

[120] and are consistent with the results shown here.

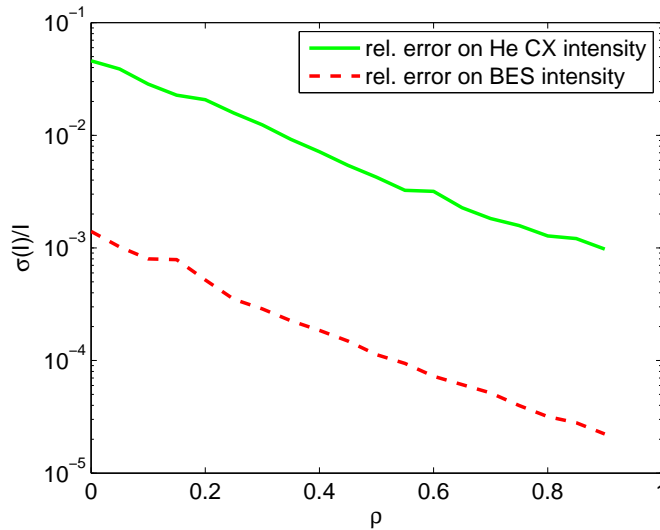


Figure 6.2: Predicted statistical 1σ -uncertainties of the He charge exchange and beam emission intensities as a function of normalized radius for the core CXS diagnostic on ITER at a helium concentration of 4%. This analysis has been performed without beam modulation, treating T_i and Ω_ϕ as free parameters and neglecting passive CX. The He CX intensity will be the critical parameter over the BES intensity. The statistical uncertainties stay well below 10%.

The most important caveat concerning the statistical error analysis is that we implicitly have assumed the spectral model to be correct. Any effect or feature in the real data that is not accounted for correctly in the spectral model could generate larger errors than the purely statistical ones shown here. The discussion on the He II 468nm spectral model is not closed. Most impurity lines in this wavelength region have been identified on current machines, but a correct spectral model for a machine with tungsten and beryllium as dominant impurities still needs to be demonstrated. Other nuisance could be caused by the plume effect (see chapter 2) and reflections in the tokamak vessel as the ITER first wall will be metallic, in contrast to current machines where graphite is the dominant wall material. Reflections could enhance the measured Bremsstrahlung background as well as polluting the core CXS channels with active CX light from the edge of the plasma as the latter has a 100-fold higher intensity.

The systematic uncertainties that enter the CX helium concentration analysis are hard to quantify. First, there is the systematic uncertainty on the CX emission rate, which has an estimated accuracy of about 20% (see chapter 5). Secondly, there is the combined error from the local beam density, intensity calibration and integration along the line of sight.

When the local beam density is calculated by means of a beam stopping code, the uncertainty increases if the beam penetrates further into the plasma. The actual uncertainty on the beam stopping cross section is not very well known, but it is not better than 10% (see sect. 3.3.3, chapter 3). In fig. 6.3, we have artificially increased the beam stopping cross section by 5%, 10% and 15% and calculated the error on the beam attenuation factor as a function of minor radius for the plasma parameters listed in table 6.1. As the attenuation of the beam reaches between 95-99% at $\rho=0$, the associated errors become as large as 30-50%.

Alternatively, one can use beam emission to measure the beam density, but the beam emission rates have an uncertainty in the order of 20% (see chapter 3). Despite this uncertainty being larger for the edge channels than the one based on beam stopping, it is approximately constant in time and radius as it is a slowly varying function of the local plasma parameters only. This is in contrast to the beam density from beam stopping which is strongly affected by changes in the whole electron density profile. As it is mainly the gradient of the helium concentration profile which is of interest for transport studies, the beam emission method is the best option for ITER. The beam stopping calculations can still be used as a consistency check if fully calibrated data is available. Note that the need for an external intensity calibration also adds a constant systematic uncertainty to the analysis based on the beam stopping method.

The various uncertainties entering the helium CXS concentration analysis are summarized in table 6.2.

In conclusion, the required 10% accuracy on the helium concentration can be reached as far as the statistical uncertainty originating from the noise on the spectra is concerned, assuming a 3.6MW and 100keV/amu NB and an etendue of $1\text{mm}^2\text{sr}$ per

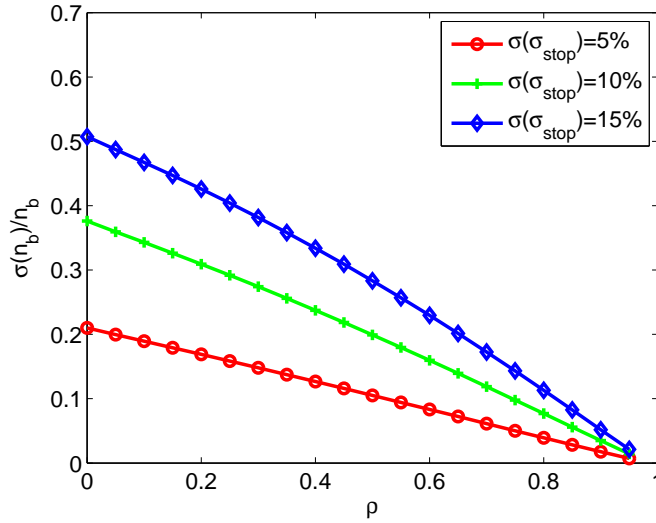


Figure 6.3: Systematic error in the local beam density as a function of normalized minor radius due to an error in the effective beam stopping cross section of 5%, 10% and 15%, for a typical ITER plasma. Applying beam attenuation, an additional systematic uncertainty entering the helium concentration analysis comes from the intensity calibration and the alignment with the beams. Alternatively, using beam emission, an approximately constant systematic uncertainty ($\approx 20\%$) due to the beam emission rates will be present. The intrinsic systematic uncertainty on the helium CX emission rate is also estimated to be in the order of 20%.

quantity	type	uncertainty
I_{CX}	statistical	up to 5%, see fig. 6.2
Q_{CX}	systematic	$\approx 20\%$
I_{BES}	statistical	$< 1\%$, see fig. 6.2
Q_{BES}	systematic	$\approx 20\%$
$n_b^{bms}(\rho)$	systematic, but function of time and ρ	up to 20-50%, see fig. 6.3
calibration/alignment	systematic	unknown

Table 6.2: Overview of sources of uncertainty entering the helium concentration analysis according to eq. 2.4-2.6.

radial channel. On the edge channels, a lower etendue could be used. Although one has to keep in mind that we have assumed a perfect spectral model with a low number of disturbing impurity lines.

As far as the absolute value of the derived helium concentration is concerned, the best option is to cross calibrate on beam emission. The combined systematic uncertainty from the beam emission and helium CX rates is estimated to be in the order of 20-30%. This seems rather high, but the ratio of the CX and BES rates only varies slowly with a change in plasma parameters, hence this systematic deviation is approximately constant over the whole radial profile and as a function of time.

A possible check on the systematic inaccuracy could be performed by a short DNB blip in a pure helium plasma during the early phase of the ITER experiments.

6.3 Fast helium CXS measurements on ITER

ITER is the first tokamak where the interaction between the main plasma and the fast α population will play an important role in the operation and control of the reactor. A large number of physics questions are expected to be answered by studying the fast ion population on ITER, such as whether fast ions will trigger instabilities and what determines radial transport of the fast ions. The feasibility of a commercial fusion reactor will depend, amongst others, on the fast ion physics knowledge gained on ITER. Therefore, the measurement requirements for the fast α population have been set to similar values as for the thermalized helium population. The energy distribution between 100keV and 3.5MeV needs to be measured with an accuracy of 20% at a time resolution of 100ms and with a spatial resolution of $a/10$ [7]. The diagnostic potential to monitor fast ions is limited. Indirect information can be gained from the neutron yield and spectrum and especially the collective Thomson scattering is capable of measuring the distribution function at high time resolution [121]. Quantitative profile densities however are difficult to obtain and CXS could contribute to this.

The main task of the ITER core CXS diagnostic is to measure the local concentration of the thermalized helium ash. In addition to measurements of the thermalized population, information on the fast α population can be obtained as well, as demonstrated on TFTR by McKee et al. [43, 122] (called α -CHERS). The diagnostic principle is conceptually very similar to the fast NB ion measurements of chapter 4, except for the much higher energy of the α -particles. Only helium ions with a collision velocity with the D or H beam neutrals close to the peak in the cross section around 35keV/amu can be detected. Because ITER will have a diagnostic beam (DNB) operated at 100keV/amu and a heating beam (HNB) operated at 500keV/amu, the expected CX spectra from both beams are very different and the expected feasibilities of fast helium CXS have to be calculated separately. The feasibility of such a diagnostic on ITER, compared to the α -CHERS diagnostic on TFTR, will be affected by a higher noise level on ITER due to a higher Bremsstrahlung (factor 5-10), and by the lower beam penetration (factor 10-10²) when using the diagnostic beam or the lower beam particle flux (factor 10) and directionally very selective cross sections when using the heating beams. These considerations result in a ratio of the active fast ion intensity over the Bremsstrahlung on ITER to be a factor of about 10² worse than on TFTR where the fast ion CX/Bremsstrahlung ratio was measured to be about 1% [122], despite the expected α density being a factor of about 30 higher on a full performance ITER.

These numbers give a first indication of the challenge measuring α 's on ITER with CXS, but as mentioned before the energy dependence of the cross sections play an

important role in the correct assessment of the feasibility as well as the effective optical throughput that could be obtained on the diagnostic.

The application of CXS to measure α 's on ITER was briefly discussed by Orsitto et al. [123], but they cite S/N ratios from calculations performed for the thermal CX line. De Angelis et al. [124] have published simulated fast α spectra and expected noise levels. However, a bug in their Bremsstrahlung calculations generated a continuum level a factor $10^{3/2}$ too low, giving a S/N ratio a factor $10^{3/4}=5.6$ too high. Furthermore, they assumed a very large etendue (25mm^2 sr per radial channel), which is not realistic as it cannot be achieved by the optics at the tokamak side. Therefore, they cite rather high S/N ratios (S/N=5 at 5ms resolution), probably obtained after summation over the full wavelength (energy) range. Given these considerations, we have repeated the spectral modelling to obtain a better understanding of the feasibility.

In order to make a quantitative study of the fast α CXS feasibility on ITER, the fast ion codes of M. von Hellermann's CX simulation package have been used to generate the expected fast helium CX spectra at 468nm. The input to the code is listed in table 6.1. In a first step, the α source rate is calculated and multiplied with the classical slowing down function to yield the fast helium velocity distribution function. In a second step, the velocity distribution is convolved with the CX rates and projected on the line of sight, according to [31]. The result is multiplied with the local NB density along a line of sight. In a last step the Bremsstrahlung is added and the photon noise on the detector is calculated according to the performance of a virtual CXS diagnostic. Similar as for the thermal helium simulation of the previous section, we neglect other emission lines in the spectrum.

First, we show the resulting CX line with the expected noise level based on a measurement on full spectral resolution and using the design parameters of the optics for the core CXRS diagnostic (see table 6.1) but at an increased exposure time $t_{exp}=1\text{s}$. Fig. 6.4(a) and 6.4(b) show the expected spectra for the HNB (looking from equatorial port 3 to HNB5) and the DNB (looking from upper port 3). It is clear that for the HNB, signal to noise is below unity over the entire energy (=Doppler shift) range, while for the DNB based diagnostic useful information can only be obtained below 200keV.

Secondly, because the signal to noise ratio depends partially on the characteristics of the diagnostic (optical throughput, energy and time resolution) we bin the signal in a few energy bins and see if we can obtain a better S/N at the cost of a lower energy resolution. For the DNB based diagnostics we take bins of 100keV, while for the HNB based system we take larger bins. We characterize the performance of the optics and spectrometer by an 'effective' optical throughput which we define as $\eta=\epsilon t_{exp} Q E T$. This is the part of the S/N ratio that is determined by the

diagnostic design, as illustrated by eq. 6.1.

$$\frac{S}{N} \approx \sqrt{\frac{\eta \Delta \lambda}{C}} < S >_{\Delta \lambda} \quad (6.1)$$

A higher η can be achieved by either lowering the time resolution or increasing the etendue and transmission of the optical system. $< S >_{\Delta \lambda}$ is the fast ion signal averaged over the wavelength range $\Delta \lambda$ and C is the spectral intensity of the continuum radiation. The fitting of the Bremsstrahlung is assumed to induce no errors, if beam modulation is used to subtract the passive emission, then eq. 6.1 should approximately be divided by $\sqrt{2}$ as the background intensity is much higher than the active signal and Poisson noise scales as the square root of the total signal.

The resulting S/N as a function of η is plotted in fig. 6.5(a)-6.5(b). The first dashed bar indicates the foreseen parameters of the core CXS diagnostic, but at 1s exposure time. The second dashed bar shows the most optimistic value of η at 1s time resolution. The maximum transmission is limited by the first mirror that will have a rather low reflectivity in ITER, the mirror labyrinth in the periscope and losses in the fiber connectors, filters or spectrometer. The 'optimistic' value in fig. 6.4 is taken to be 15%. It could be achieved by replacing the spectrometers by band pass filters. The upper limit of the etendue is set by the etendue of the optics on the tokamak side. Assuming a mirror diameter of 10cm and a spot size on the beam of 10cm at a distance of 4m and assuming that this etendue can be preserved along the optical path through the periscope, the upper limit for the etendue is approximately 3.8mm^2 sr.

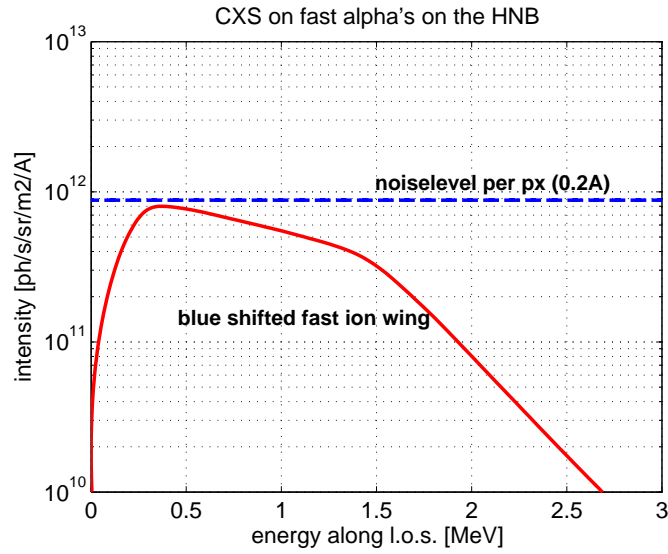
As conclusion, when combining the CXS data from both the HNB and DNB a 1σ -accuracy of 10% on the fast ion CX intensity could be obtained over a rather wide energy range (0.1-1MeV) when using coarse wavelength bins and an effective optical throughput $\eta=10^{-7}\text{m}^2$ sr s. This corresponds to 2s integration at the foreseen diagnostic performance or 200ms when using higher throughput instruments.

An important remark to the results shown here, is that we have assumed a rather coarse energy binning and a background emission consisting purely of Bremsstrahlung. On current tokamaks, many impurity lines are observed around 468nm, mainly from carbon but also from beryllium, apart from possible contamination with tungsten lines, which is still unclear. Especially on the blue shifted wing of the helium CX line, which is the preferred wing for detecting fast α 's because both equatorial and top port 3 are looking towards the beams (and CX cross sections are higher for fast ions moving along the beam), several high intensity C III and C VI lines appear, apart from the broad Be IV CX emission lines. This has not been taken into account in this analysis, but will further reduce the S/N ratio and limit the choice of the wavelength bins that could be applied to line free regions.

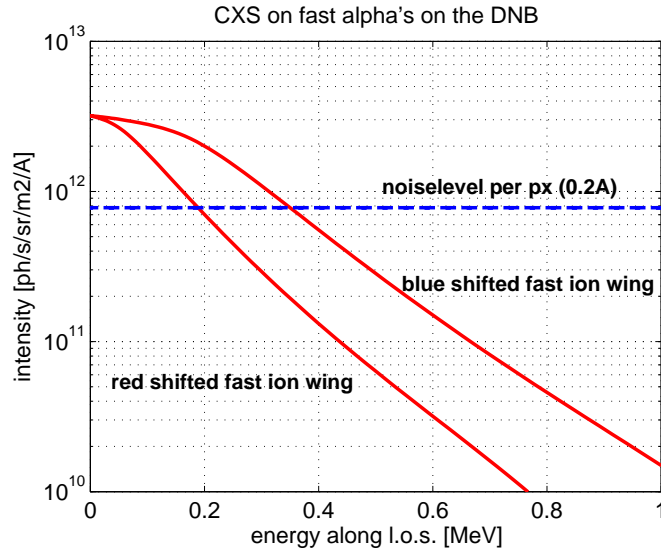
There are a few options to enhance the S/N ratio, but all with limited prospects. The conceptually most straightforward option is a better focussed neutral beam.

The signal to noise ratio scales as $S/N \propto \langle S \rangle_{\Delta\lambda} \propto 1/w_{\perp}$, with w_{\perp} the width of the beam perpendicular to the line of sight. Other options are to change the beam species or to look at different transitions. The analysis above was focussed on the $n=4-3$ transition in He^+ resulting from CX using neutral hydrogen beams. The $n=3-2$ or $n=2-1$ transitions have a higher intensity, but are in the UV and have a higher Bremsstrahlung background as well. The option to use helium or lithium beams (pure or mixed with hydrogen) has been proposed for α diagnostics. The CX cross sections from helium or lithium donors are higher than those from hydrogen at high energies by approximately one order of magnitude (see e.g. [125]). However, the use of helium comes at the cost of a lower beam luminosity as it is much more difficult to produce highly energetic helium beams due to the difficulties in applying negative ion beam technology to helium. Apart from single CX, there is also the option to look at the emission lines of neutral helium following double CX [126], but the cross sections are not scaling advantageously at high energies.

As final conclusion, prospects for fast helium measurements on ITER using either the HNB or DNB are limited. Only with a wavelength binning corresponding to several hundreds keV per bin and assuming a very low contamination with impurity lines, could a signal to noise ratio of 10 be obtained at a time resolution of 1s and an etendue of 2-3 mm^2sr . This is lower than the requested time and energy resolution, but CXS could still contribute to the study of the steady state fast ion density profiles.

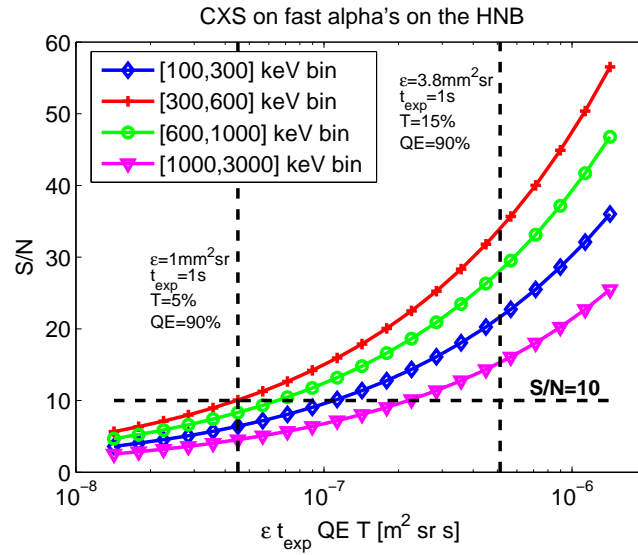


(a) Modelled slowing down spectrum for CX between fast α 's and the HNB. The noise level per pixel is calculated with an optical throughput $\varepsilon t_{exp} QE T = 0.045 \text{ mm}^2 \text{ sr s}$. The spectrum peaks at low collision velocities between the beam and the fast ion population.

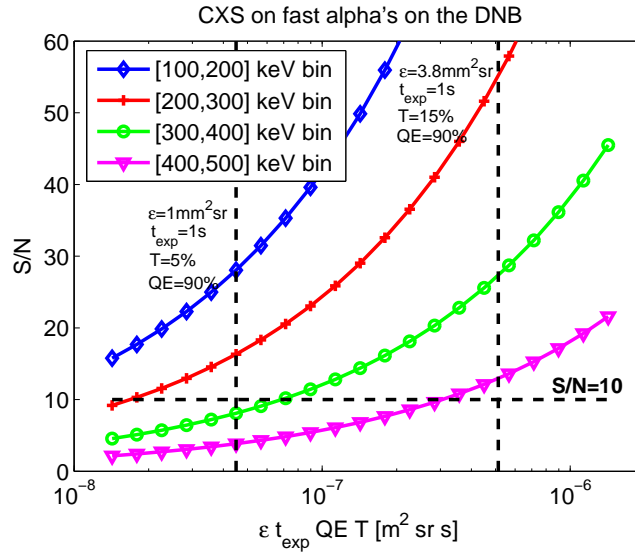


(b) Modelled slowing down spectrum for CX between fast α 's and the DNB. The noise level per pixel is calculated with an optical throughput $\varepsilon t_{exp} QE T = 0.045 \text{ mm}^2 \text{ sr s}$. Due to the lower energy of the beam, compared to the HNB, the DNB base CX diagnostic will mainly be sensitive to thermal ions.

Figure 6.4: Predicted ITER CX spectra on fast helium, looking from the equatorial MSE port to the HNBs (500keV/amu, 17MW) and looking from upper port 3 to the diagnostic beam (100keV/amu, 3.6MW). The modelled spectrum is shown with the expected noise level per pixel (assuming Poisson noise on the Bremsstrahlung) on full resolution, fig. 6.5 shows the signal to noise ratio when the signal is summed over a number of energy bins. All calculations are for $\rho = 0.5$, $n_e = 10^{20} (1 - \rho^2)^{0.1} \text{ m}^{-3}$, $T_i = 21 (1 - \rho^2)^{0.8} \text{ keV}$, $T_e = 25 (1 - \rho^2)^{0.5} \text{ keV}$, corresponding fusion power is $P_f = 615 \text{ MW}$. ε is the etendue, t_{exp} the exposure time, QE the quantum efficiency and T the optical transmission factor.



(a) S/N on the binned fast ion intensity as a function of the effective optical throughput for HNB based CXS on fast ions. The reference value for the core CXRS design (but at 1s time resolution) and a more optimistic value (assuming a 10cm diameter first mirror, a 10cm spot size on the beam at a distance of 4m and a 15% optical transmission) are indicated by dashed lines.



(b) S/N on the binned fast ion intensity as a function of the effective optical throughput for DNB based CXS on fast ions. Lower energy bins are used compared to the HNB results.

Figure 6.5: Predicted signal to noise ratios for charge exchange spectroscopy on fast helium when the spectra (shown in fig. 6.4) are summed over a number of energy bins. The Bremsstrahlung intensity is assumed to be known without error. When beam modulation is employed, the S/N should be divided by $\sqrt{2}$. The experimental conditions are the same as those listed in the caption of fig. 6.4.

Conclusions and outlook

In this thesis, the accuracy of quantitative hydrogen beam emission spectroscopy is investigated and applied to the measurements of fast ion and thermal helium density profiles.

In chapter 2, the physics of hydrogen beam driven spectroscopy is revisited and the diagnostic setup on TEXTOR is described. It is found that the most critical aspect of quantitative CXS is the characterisation of the neutral beam (attenuation, power fractions, excited population, active volumes).

The use of beam emission to characterise the beam is investigated in chapter 3. A comparison of several collisional-radiative (CR) models for the neutral beams revealed inconsistencies up to a factor of 2 that were solved by a reassessment of the cross section used as input to the models and corrections to one of the codes. This allowed us to achieve consistency among all published models. The CR models agree better on beam stopping, but recent progress in the calculation of the proton impact ionisation cross sections of ground state hydrogen results in an increase of the beam stopping cross section by up to 15%.

The calculated relative $n=3$ to $n=4$ population agrees within 10% to the measured ratio from JET using the H_α to H_β beam emission intensities. The radial profiles and time traces of the measured and modelled NB density agree well, but the overall intensity of the measured beam density is $\approx 30\%$ lower. The reason for this is uncertain. Apart from the involved atomic data, this could also be due to a combination of calibration, alignment and especially the characterization of the neutral beam path. These issues are currently the main motivation to use beam emission.

The power fractions of the JET beams were reevaluated with the new beam emission rates which lead to a correction in the interpretation of the spectroscopic data from the JET NB Test Bed and, finally, to good consistency between test stand, beam in plasma and beam in gas emission.

The Stark line intensities within the MSE multiplet are in good agreement with a sublevel resolved model. The measured σ/π intensity is disturbed by the polarization characteristics of the tokamak side optics and the $n=3$ subpopulation structure, the latter effect is consistent with the CR modelling.

The overall agreement found on JET between the modelled and expected beam emission intensities gives confidence in the proposed scheme combining charge exchange and beam emission that will be used to measure the helium ash on ITER. The agreement between the modelled and measured MSE spectra gives confidence

in the Stark resolved CR modelling and hence such a model could be used to correct the measured σ/π -ratio when used to constrain magnetic field reconstructions.

A setup combining CXS and BES has been used on TEXTOR to validate the helium concentration measurements during strong helium gas puffs against the increase in electron density (chapter 5, sect. 5.2). The increase in the helium density derived from the raise of the electron density was found to be 17% lower than the increase measured with CXS/BES. The a priori uncertainty on the CXRS and BES rates is usually estimated at 20%. Although this is not more than an educated guess, it is consistent with our experiment. Measurements of the thermal D+H concentration with CXS/BES (neglecting halo emission) were consistent with a Z_{eff} of 2.5 (chapter 5, sect. 5.3). These results give confidence that the CXS/BES method does not induce systematic errors larger than 20-30%.

Statistical uncertainties from fitting modelled BES and CXS spectra for ITER give confidence that the statistical errors will be below 10% over the entire radial range, using the current design parameters for the DNB and the optics (chapter 6, sect. 6.2).

Summarizing, the response to the first question raised in the introduction to this thesis, 'Is beam emission a validated technique to measure the beam density?', is yes, beam emission is a reliable technique but with a systematic uncertainty of about 20-30%.

The answer to the second question, 'Can charge exchange spectroscopy be used to measure fast (beam) ion profiles?', is also yes, but the success of the technique depends very much on the machine and experimental conditions.

We have measured CX spectra between beam neutrals and fast ions injected by the neutral beams on TEXTOR and JET (chapter 4). Variation of the beam voltage on TEXTOR makes the origin of the fast ion signal unambiguous. The spectral shape of the fast ion spectrum corresponds to the calculated shape based on an approximation of the fast ion slowing down function and a convolution with the charge exchange emission rates. However, the application of the method to study the fast ion transport and confinement is limited by the pollution of the signal by passive charge exchange between background neutrals and fast ions on TEXTOR and by the low signal to noise ratio on JET. A faster detector is proposed for the TEXTOR diagnostic, which would allow to use beam modulation in order subtract the fitted passive emission.

Despite these limitations, we have derived fast ion density profiles from the TEXTOR data by subtracting the first frame after the diagnostic beam switch off. The fast ion profiles are remarkably flatter in the core plasma than the modelled fast ion profiles. A possible explanation is given by fast ion redistribution due to sawtooth crashes, which was also observed by collective Thomson scattering.

Expected signal to noise ratios on the ITER fast helium CX spectra have been calculated and only with coarse wavelength binning (\propto several 100 keV), neglecting disturbing impurity lines in the spectrum and with a product of etendue, exposure

time and transmission of approx. 10^{-7} m² sr s, could the fast ion intensity profile be retrieved with a signal to noise ratio in the order of 10 (chapter 6, sect. 6.3). The best option to improve the signal to noise ratio is a neutral particle beam with higher luminosity.

On the way to ITER, the JET tokamak has now been equipped with an ITER-like beryllium/tungsten wall yielding an impurity mix in the plasma that will be similar as on ITER. The experience gained by analysing the JET helium CXS spectra will further help to determine the achievable accuracy on ITER. It also offers the opportunity to experimentally assess the effect of reflections on the inner metallic wall. If a new high power DT campaign will take place on JET, CXS could potentially be used to study the slowing down α 's.

Bibliography

- [1] BP Statistical Review of World Energy 2010. 1, 2
- [2] International Energy Agency, www.iea.org. 1, 2
- [3] IAEA Red Book 2010, www.iaea.org. 1, 2
- [4] from "The World of Andrei Sakharov: A Russian Physicist's Path to Freedom", G. Gorelik, Oxford University Press, original source of publication drawing unknown. 3
- [5] M. Keilhacker, A. Gibson, et al. *Nucl. Fusion*, 39(2):209–234, 1999. 3
- [6] R. J. Hawryluk et al. Fusion plasma experiments on TFTR: A 20 year retrospective. *Physics of Plasmas*, 5(5, Part 2):1577–1589, 1998. 3
- [7] A. J. H. Donné et al. Chapter 7: Diagnostics. *Nucl. Fusion*, 47(6):S337, 2007. 4, 5, 90, 95
- [8] RC Isler. *Physica Scripta*, 35(5):650–661, 1987. 10
- [9] RC Isler. *Plasma Phys. Control. Fusion*, 36(2):171–208, 1994. 10, 15
- [10] D. M. Thomas, G. R. McKee, K. H. Burrell, F. Levinton, E. L. Foley, and R. K. Fisher. *Fusion Science and Technology*, 53(2):487–527, 2008. 10
- [11] I. H. Hutchinson. *Principles of Plasma Diagnostics, second edition*. Cambridge University Press, 2002. 10, 13
- [12] R. C. Isler. *Phys. Rev. Lett.*, 38(23):1359–1362, 1977. 10
- [13] R. C. Isler, L. E. Murray, S. Kasai, J. L. Dunlap, S. C. Bates, P. H. Edmonds, E. A. Lazarus, and M. Murakami. *Phys. Rev. A*, 24(5):2701–2712, 1981. 10
- [14] R. J. Fonck, R. J. Goldston, R. Kaita, and D. E. Post. *Applied Physics Letters*, 42(3):239–241, 1983. 11
- [15] R. J. Fonck, D. S. Darrow, and K. P. Jaehnig. *Phys. Rev. A*, 29(6):3288–3309, 1984. 11, 19, 20, 21, 27, 28
- [16] R. P. Seraydarian, K. H. Burrell, N. H. Brooks, R. J. Groebner, and C. Kahn. *Rev. Sci. Instrum.*, 57(2):155–163, 1986. 11
- [17] M. G. von Hellermann et al. *Proc. 13th European Conf. Controlled Fusion and Plasma Physics*, 1986. 11
- [18] A. Boileau, M. Von Hellermann, L. D. Horton, J. Spence, and H. P. Summers. *Plasma Phys. Control. Fusion*, 31(5):779–804, 1989. 11, 19, 50, 54, 55, 57

- [19] R. B. Howell, R. J. Fonck, R. J. Knize, and K. P. Jaehnig. *Rev. Sci. Instrum.*, 59(8, Part 2):1521–1523, 1988. 11, 22
- [20] U. Gerstel, L. Horton, H. P. Summers, M. von Hellermann, and B. Wolle. *Plasma Phys. Control. Fusion*, 39(5):737–756, 1997. 12, 27, 29
- [21] M. Tunklev, P. Breger, K. Gunther, M. von Hellermann, R. Konig, M. O’Mullane, and K. D. Zastrow. *Plasma Phys. Control. Fusion*, 41(8):985–1004, 1999. 12
- [22] M. G. von Hellermann, G. Bertschinger, W. Biel, C. Giroud, R. Jaspers, C. Jupen, O. Marchuk, M. O’Mullane, H. P. Summers, A. Whiteford, and K. D. Zastrow. *Physica Scripta*, T120:19–29, 2005. 12
- [23] CXSFIT manual, available at www.adas.ac.uk. 12, 33, 46
- [24] H. P. Summers. *The ADAS User Manual, version 2.6*, <http://adas.phys.strath.ac.uk>. 2004. 14, 19, 20, 29, 53, 72, 85, 89
- [25] B. H. Bransden and McDowell M. R. C. *Charge Exchange and the Theory of Ion-Atom Collisions*. Clarendon Press, Oxford, 1992. 13, 55
- [26] H. P. Summers, W. J. Dickson, M. G. O’Mullane, N. R. Badnell, A. D. Whiteford, D. H. Brooks, J. Lang, S. D. Loch, and D. C. Griffin. *Plasma Phys. Control. Fusion*, 48(2):263–293, 2006. 17
- [27] D. H. Sampson. *J. Phys. B-At. Mol. Opt. Phys.*, 10(4):749–760, 1977. 18, 19
- [28] J. Spence and H. P. Summers. *J. Phys. B-At. Mol. Opt. Phys.*, 19(22):3749–3776, 1986. 19
- [29] W. Mandl. phd thesis: Development of active balmer-alpha spectroscopy at jet. 1991. 20, 21, 22, 26, 27, 33
- [30] A. Blom and C. Jupen. *Plasma Phys. Control. Fusion*, 44(7):1229–1241, 2002. 21, 22
- [31] M. G. von Hellermann, W. G. F. Core, J. Frieling, L. D. Horton, R. W. T. Koenig, W. Mandl, and H. P. Summers. *Plasma Phys. Control. Fusion*, 35:799–824, 1993. 22, 24, 29, 30, 72, 74, 75, 85, 96
- [32] M. von Hellermann, P. Breger, J. Frieling, R. Konig, W. Mandl, A. Maas, and H. P. Summers. *Plasma Phys. Control. Fusion*, 37(2):71–94, 1995. 23, 24, 29
- [33] W. M. Solomon, K. H. Burrell, R. Feder, A. Nagy, P. Gohil, and R. J. Groebner. *Rev. Sci. Instrum.*, 79(10), 2008. 23
- [34] J. E. Rice, E. S. Marmor, J. L. Terry, E. Kallne, and J. Kallne. *Phys. Rev. Lett.*, 56(1):50–53, 1986. 24

- [35] R. C. Isler and R. E. Olson. *Phys. Rev. A*, 37(9):3399–3402, 1988. 24
- [36] R. Hoekstra, H. Anderson, F. W. Blik, M. von Hellermann, C. F. Maggi, R. E. Olson, and H. P. Summers. *Plasma Phys. Control. Fusion*, 40(8):1541–1550, 1998. 24
- [37] C. F. Maggi et al., 30th EPS Conference on Contr. Fusion and Plasma Phys., St. Petersburg, 7-11 July 2003 ECA Vol. 27A, P-1.63. 25, 26
- [38] R. J. E. Jaspers, private communication. 25
- [39] I. O. Bespamyatnov, W. L. Rowan, R. S. Granetz, and D. F. Beals. *Rev. Sci. Instrum.*, 77(10), 2006. 25, 26
- [40] O. Marchuk, Yu Ralchenko, R. K. Janev, G. Bertschinger, and W. Biel. *J. Phys. B-At. Mol. Opt. Phys.*, 42(16), 2009. 27
- [41] R. E. Bell. *Rev. Sci. Instrum.*, 77(10):10E902, 2006. 28
- [42] W. W. Heidbrink, K. H. Burrell, Y. Luo, N. A. Pablant, and E. Ruskov. *Plasma Phys. Control. Fusion*, 46(12):1855–1875, 2004. 29, 30, 70
- [43] G. McKee, R. Fonck, et al. *Phys. Rev. Lett.*, 75:649–652, 1995. 30, 95
- [44] Y. Luo, W. W. Heidbrink, et al. *Rev. Sci. Instrum.*, 78:033505, 2007. 30
- [45] W. W. Heidbrink, Y. Luo, et al. *Plasma Phys. Control. Fusion*, 49:1457–1475, 2007. 30, 74
- [46] M. Podesta, W. W. Heidbrink, R. E. Bell, and R. Feder. *Rev. Sci. Instrum.*, 79(10):10E521, 2008. 30
- [47] M. Osakabe, S. Murakami, et al. *Rev. Sci. Instrum.*, 79(10):10E519, 2008. 30
- [48] W. W. Heidbrink, Y. Luo, C. M. Muscatello, Y. Zhu, and K. H. Burrell. *Rev. Sci. Instrum.*, 79(10):10E520, 2008. 30
- [49] M. A. Van Zeeland, W. W. Heidbrink, and J. H. Yu. *Plasma Phys. Control. Fusion*, 51(5):055001, 2009. 30
- [50] A. Boileau, M. von Hellermann, W. Mandl, H. P. Summers, H. Weisen, and A. Zinoviev. *J. Phys. B-At. Mol. Opt. Phys.*, 22:L145–L152, 1989. 31, 40
- [51] M. G. von Hellermann, R. J. E. Jaspers, H. P. Summers, and K.-D. Zastrow. *Advanced diagnostics for magnetic and inertial fusion*. edited by P Stott et al., Kluwer Academic, N.Y., 125-128, 2001. 32, 50
- [52] M. De Bock, K. Jakubowska, M. G. von Hellermann, R. J. E. Jaspers, A. J. H. Donné, and L. Shmaenok. *Rev. Sci. Instrum.*, 75:4155–4157, 2004. 32, 50

- [53] M. G. von Hellermann, E. Delabie, R. J. E. Jaspers, W. Biel, O. Marchuk, H. P. Summers, A. Whiteford, C. Giroud, N. C. Hawkes, and K. D. Zastrow. volume 988, pages 165–176, 2008. 32
- [54] R. J. E. Jaspers, M. G. von Hellermann, E. Delabie, W. Biel, O. Marchuk, and L. Yao. *Rev. Sci. Instrum.*, 79(10):10F526, 2008. 32, 40, 50, 81
- [55] W. Mandl, R. C. Wolf, M. G. von Hellermann, and H. P. Summers. *Plasma Phys. Control. Fusion*, 35:1373–1394, 1993. 32, 35, 39, 40, 50, 51, 54, 57, 60
- [56] W. L. Rowan, M. B. Sampson, and R. S. Granetz. *Rev. Sci. Instrum.*, 75:3487–3489, 2004. 32, 50
- [57] H. Euringer and Ph. Verplancke. *Rev. Sci. Instrum.*, 65:2996–2999, 1994. 32, 35, 50
- [58] C. Giroud, A. G. Meigs, C. R. Negus, K. D. Zastrow, T. M. Biewer, T. W. Versloot, and JET-EFDA Contributors. *Rev. Sci. Instrum.*, 79(10):10F525, 2008. 32, 35, 50, 56, 58, 59
- [59] R. C. Wolf, L.-G. Eriksson, M. Von Hellermann, R. Konig, W. Mandl, and F. Porcelli. *Nucl. Fusion*, 33(12):1835, 1993. 32, 39, 50
- [60] F. M. Levinton, R. J. Fonck, G. M. Gammel, R. Kaita, H. W. Kugel, E. T. Powell, and D. W. Roberts. *Phys. Rev. Lett.*, 63(19):2060–2063, 1989. 32, 41, 63
- [61] C. Markwardt, MPFIT package, available at www.physics.wisc.edu/~craigm/idl/idl.html. 33
- [62] M. De Bock, "Combined Charge Exchange - Beam Emission spectroscopy", private communication. 34
- [63] M. F. M. De Bock, N. J. Conway, M. J. Walsh, P. G. Carolan, and N. C. Hawkes. volume 79, page 10F524, 2008. 34
- [64] I. D. Williams, J. Geddes, and H. B. Gilbody. *J. Phys. B: At. Mol. Phys.*, 15:1377–1389, 1982. 36, 37, 61, 62
- [65] R. S. Hemsworth. *JET-DN-C(85)8*, 1985. 36, 61, 66
- [66] R. Uhlemann, R. S. Hemsworth, G. Wang, and H. Euringer. *Rev. Sci. Instrum.*, 64:974–982, 1993. 36, 61, 66, 86
- [67] E L Foley and F M Levinton. *J. Phys. B-At. Mol. Opt. Phys.*, 39(2):443–453, 2006. 38
- [68] M. F. Gu, C. T. Holcomb, R. J. Jayakuma, and S. L. Allen. *J. Phys. B-At. Mol. Opt. Phys.*, 41(9):095701, 2008. 38, 40, 42, 55, 57

- [69] E. L. Foley, F. M. Levinton, H. Y. Yuh, and L. E. Zakharov. *Rev. Sci. Instrum.*, 79(10):10F521, 2008. 39, 50
- [70] O Marchuk, Yu Ralchenko, R K Janev, W Biel, E Delabie, and A M Urnov. *J. Phys. B-At. Mol. Opt. Phys.*, 43(1):011002, 2010. 40, 42, 50, 55, 57, 63, 64, 65, 66
- [71] K. Jakubowska, M. De Bock, R. Jaspers, M. Von Hellermann, and L. Shmaenok. *Rev. Sci. Instrum.*, 75(10):3475–3477, 2004. 40, 50
- [72] N. A. Pablant, K. H. Burrell, R. J. Groebner, D. H. Kaplan, and C. T. Holcomb. *Rev. Sci. Instrum.*, 79(10):10F517, 2008. 40, 50
- [73] N. Pablant, phd thesis, "Development of the B-Stark motional Stark effect diagnostic for measurements of the internal magnetic field in the DIII-D tokamak", University of California at San Diego, 2010. 40
- [74] M. von Hellermann, M. de Bock, et al. *Rev. Sci. Instrum.*, 75(10):3458–3461, 2004. 41, 43
- [75] FM Levinton, GM Gammel, R Kaita, HW Kugel, and DW Roberts. *Rev. Sci. Instrum.*, 61(10, Part 2):2914–2919, 1990. 41
- [76] R. Jaspers, B. S. Q. Elzendoorn, A. J. H. Donné, and T. Soetens. *Rev. Sci. Instrum.*, 72(1, Part 2):1018–1022, 2001. 41, 43
- [77] Atsushi Iwamae, Atsushi Sakaue, Makoto Atake, Keiji Sawada, Motoshi Goto, and Sigeru Morita. *Plasma Phys. Control. Fusion*, 51(11):115004, 2009. 41
- [78] Howard Y. Yuh, F. M. Levinton, S. D. Scott, and J. Ko. *Rev. Sci. Instrum.*, 79(10), 2008. 42
- [79] R. Uhlemann and J. Ongena. *Fusion Technology*, 35(1):42–53, 1999. 42
- [80] J. W. Coenen, B. Schweer, M. Clever, S. Freutel, O. Schmitz, H. Stoschus, U. Samm, B. Unterberg, and TEXTOR Team. *J. Phys. B-At. Mol. Opt. Phys.*, 43(14), 2010. 43
- [81] M. De Bock, phd thesis, "Understanding and controlling plasma rotation in tokamaks", Technical University of Eindhoven, 2007. 43
- [82] T. Soetens, R. Jaspers, and E. Desoppere. *Rev. Sci. Instrum.*, 70(1, Part 2):890–893, 1999. 43
- [83] J. Howard. *Plasma Phys. Control. Fusion*, 50(12), 2008. 44
- [84] J. Howard, R. Jaspers, O. Lischtschenko, E. Delabie, and J. Chung. *Plasma Phys. Control. Fusion*, 52(12):125002, 2010. 44

- [85] Ralchenko, Yu., Kramida, A.E., Reader, J., and NIST ASD Team. NIST Atomic Spectra Database (ver. 4.0.1). Available: <http://physics.nist.gov/asd>. National Institute of Standards and Technology, Gaithersburg, MD, 2010. 45
- [86] J. G. Krom, M. Korten, H. R. Koslowski, A. Krämer-Flecken, G. Manduchi, B. U. Niderost, J. W. Oosterbeek, R. P. Schorn, F. Wijnoltz, B. Becks, W. Biel, M. P. Evrard, J. C. van Gorkom, and M. G. von Hellermann. *Fusion Engineering and Design*, 60(3):475–480, 2002. 46
- [87] W. Elmenhorst, M. von Hellermann, H. R. Koslowski, A. Kraemer-Flecken, and J. Krom. *Fusion Engineering and Design*, 81(15-17, Sp. Iss. SI):2025–2029, 2006. 46
- [88] H. Anderson, M. G. von Hellermann, R. Hoekstra, L. D. Horton, A. C. Howman, R. W. T. Konig, R. Martin, R. E. Olson, and H. P. Summers. *Plasma Phys. Control. Fusion*, 42:781–806, 2000. 49, 50, 51, 52, 53, 54, 64, 82
- [89] I H Hutchinson. *Plasma Phys. Control. Fusion*, 44(1):71–82, 2002. 49, 50, 51, 52, 53, 64
- [90] O. Marchuk, G. Bertschinger, W. Biel, E. Delabie, M. G. von Hellermann, R. Jaspers, and D. Reiter. *Rev. Sci. Instrum.*, 79(10):10F532, 2008. 49, 50, 51, 52, 53, 54, 55, 64
- [91] R. K. Janev, C. D. Boley, and D. E. Post. *Nucl. Fusion*, 29:2125–2140, 1989. 50, 51, 52, 53
- [92] S. Suzuki, T. Shirai, M. Nemoto, K. Tobita, H. Kubo, T. Sugie, A. Sakasai, and Y. Kusama. *Plasma Phys. Control. Fusion*, 40(12):2097–2111, 1998. 50, 53, 54
- [93] R. P. Seraydarian, K. H. Burrell, and R. J. Groebner. *Rev. Sci. Instrum.*, 59(8):1530–1532, 1988. 50, 51
- [94] C. D. Boley, R. K. Janev, and D. E. Post. *Phys. Rev. Lett.*, 52(7):534–537, 1984. 51
- [95] R. K. Janev and J. Smith. *Atomic Plasma Mater. Int. Data Fusion*, 1993. 51, 52, 53, 54, 55
- [96] P. D. Fainstein, V. H. Ponce, and R. D. Rivarola. *J. Phys. B-At. Mol. Opt. Phys.*, 23(9):1481–1489, 1990. 52
- [97] A. Igarashi and T. Shirai. *Phys. Rev. A*, 50(6, Part A):4945–4950, 1994. 52
- [98] M. McCartney and D. S. F. Crothers. *Zeitschrift fur Physik D-Atoms Molecules and Clusters*, 35(1):1–2, 1995. 52
- [99] G. H. Olivera, R. D. Rivarola, and P. D. Fainstein. *Phys. Rev. A*, 51(1):847–849, 1995. 52

- [100] ALADDIN database maintained by the IAEA. <http://www-amdis.iaea.org/aladdin>. 52, 54
- [101] M. O'Mullane. http://www.adas.ac.uk/notes/adas_c09-01.pdf. 52
- [102] Emil Y. Sidky and C. D. Lin. *Phys. Rev. A*, 65(1):012711, 2001. 54, 56
- [103] A. Kolakowska, M. S. Pindzola, and D. R. Schultz. *Phys. Rev. A*, 59(5):3588–3591, 1999. 54, 56
- [104] Nobuyuki Toshima. *Phys. Rev. A*, 59(3):1981–1987, 1999. 54, 56
- [105] Thomas G. Winter. *Phys. Rev. A*, 80(3):032701, 2009. 54, 56
- [106] M. B. Shah and H. B. Gilbody. *J. Phys. B-At. Mol. Opt. Phys.*, 14(14):2361–2377, 1981. 54
- [107] M. B. Shah, D. S. Elliott, and H. B. Gilbody. *J. Phys. B-At. Mol. Opt. Phys.*, 20(11):2481–2485, 1987. 54
- [108] Yu. Ralchenko and Y. Maron. *J. Quant. Spectrosc. Radiat. Transf.*, 71(2-6):609–621, 2001. 55
- [109] C. R. Negus, C. Giroud, A. G. Meigs, K. D. Zastrow, D. L. Hillis, and JET-EFDA Contributors. *Rev. Sci. Instrum.*, 77(10):10F102, 2006. 56
- [110] D. Ciric, J. J. Milnes, and E. Surrey. Misalignment on multi-aperture particle beam properties. *19th IEEE/NPSS Symposium on Fusion Engineering*, 2002. 59
- [111] W. W. Heidbrink and G. J. Sadler. *Nucl. Fusion*, 34(4):535–615, APR 1994. 67
- [112] ITER Physics Expert Group on Energetic Particles, Heating and Current Drive et al. Iter physics basis, chapter 5: Physics of energetic ions. *Nucl. Fusion*, 39:2471–2495, 1999. 67, 87
- [113] W. W. Heidbrink, J. M. Park, M. Murakami, C. C. Petty, C. Holcomb, and M. A. Van Zeeland. *Phys. Rev. Lett.*, 103(17), 2009. 67
- [114] R. J. E. Jaspers, M. G. von Hellermann, E. Delabie, J. E. Boom, A. J. H. Donné, W. Biel, N. C. Hawkes, O. Neubauer, M. Di Maio, S. Sadakov, F. Klinkhamer, B. Snijders, and A. Hogenbirk. *International Conference on Burning Plasma Diagnostics, Varenna, Italy, AIP Conference Proceedings*, 988:209–213, 2007. 68
- [115] J. G. Cordey and W. G. F. Core. *The Physics of Fluids*, 17:1626–1630, 1974. 72, 74
- [116] W. G. F. Core. *Nucl. Fusion*, 33(5):829–830, 1993. 72, 85

-
- [117] I. O. Bespamyatnov, W. L. Rowan, K. T. Liao, and R. S. Granetz. *Rev. Sci. Instrum.*, 81:10. 81
- [118] J. E. Boom, master thesis, "Helium transport and exhaust measurements with an ITER-relevant spectroscopic technique", Technical University of Eindhoven, 2007. 82
- [119] S. K. Nielsen, H. Bindslev, M. Salewski, A. Buerger, E. Delabie, V. Furtula, M. Kantor, S. B. Korsholm, F. Leipold, F. Meo, P. K. Michelsen, D. Moseev, J. W. Oosterbeek, M. Stejner, E. Westerhof, P. Woskov, and the TEXTOR team. *Plasma Phys. Control. Fusion*, 52(9):092001, 2010. 87
- [120] M. G. von Hellermann, R. Barnsley, W. Biel, E. Delabie, N. Hawkes, R. Jaspers, D. Johnson, F. Klinkhamer, O. Lischtschenko, O. Marchuk, B. Schunke, M. J. Singh, B. Snijders, H. P. Summers, D. Thomas, S. Tugarinov, and P. Vasu. *Nuclear instruments & methods in physics research section A-accelerators spectrometers detectors and associated equipment*, 623(2):720–725, 2010. 89, 91, 92
- [121] F. Meo, H. Bindslev, S. B. Korsholm, E. L. Tsakadze, C. I. Walker, P. Woskov, and G. Vayakis. *Rev. Sci. Instrum.*, 75(10, Part 2):3585–3588, 2004. 95
- [122] G. R. McKee, R. J. Fonck, B. C. Stratton, R. V. Budny, Z. Chang, and A. T. Ramsey. *Nucl. Fusion*, 37(4):501–516, 1997. 95
- [123] F. P. Orsitto, J. M. Noterdaeme, A. E. Costley, A. J. H. Donné, and ITPA TG Diagnostics. *Nucl. Fusion*, 47(9):1311–1317, 2007. 96
- [124] R. De Angelis, M. G. von Hellermann, F. P. Orsitto, and S. Tugarinov. *Rev. Sci. Instrum.*, 79(10):10E517, 2008. 96
- [125] D. E. Post, D. R. Mikkelsen, R. A. Hulse, L. D. Stewart, and J. C. Weisheit. *Journal of Fusion Energy*, 1(2):129–142, 1981. 98
- [126] K. D. Zastrow, M. O'Mullane, M. Brix, C. Giroud, A. G. Meigs, M. Proschek, and H. P. Summers. *Plasma Phys. Control. Fusion*, 45(9):1747–1756, 2003. 98

Summary: Neutral beam driven hydrogen spectroscopy in fusion plasmas

ITER, the next generation fusion reactor, is currently being constructed with the challenge of demonstrating the technical feasibility of a nuclear fusion driven power plant. In ITER, the generated fusion power will exceed the external heating by a factor 10, generating a large population of fusion-born helium in the plasma that needs to be measured and eventually controlled to prevent fuel dilution. The only method capable of measuring the local density of fully ionized helium in a fusion plasma is charge exchange spectroscopy (CXS), which relies on populating excited levels of plasma ions by charge transfer collisions with hydrogen atoms, injected by a powerful neutral hydrogen beam.

The work described in this thesis is focussed on 2 open questions: 'Can the emission by the neutral beam itself be reliably combined with CXS to obtain absolute helium concentrations?' and 'Can CXS be used to measure density profiles of non-thermal ions?'.

The quantitative interpretation of beam emission (BES), i.e. relating the observed excited population to the ground state density, has been the subject of investigation by several groups over the last 20 years, leading to different results. In this thesis, collisional-radiative models from different modellers have been compared and inconsistencies, both in the models and in the cross sections that were used, have been solved. The resulting emission rates have been used to compare expected beam densities with measured densities using Balmer- α and Balmer- β beam emission spectra from the JET tokamak. Excellent agreement between the Balmer- α and - β spectra, and reasonable agreement with the expected ground state density was found. The Stark line intensities within the beam emission multiplet have been compared with a newly developed sublevel resolved collisional-radiative model, showing good agreement, and providing an explanation to earlier failed experiments of using the line ratios to obtain information about the magnetic pitch angle. As a side result, beam emission spectroscopy has been used to correct and validate the determination of the fractional energy components in the neutral beams.

A setup combining CXS and BES, similar to the one on ITER, has been used on the TEXTOR tokamak to validate the helium concentration measurements during strong helium gas puffs against the increase in electron density. The TEXTOR helium concentration data as well as the beam densities obtained on JET give confidence that the proposed CXS analysis scheme on ITER combining beam emission and charge exchange data will not induce systematic uncertainties larger than 20-30%. Purely statistical errors from fitting the helium and MSE spectrum on ITER are obtained from modelling the spectra and are expected to be lower than 10% over the entire radial range.

Measuring fast ions in tokamak plasmas with CXS combines challenges on both

the hardware and analysis side to measure and interpret a faint, broad and anisotropic spectrum, polluted by parasitic emission and distorted by cross section effects. A high-resolution, high-throughput spectrometer has been commissioned on TEXTOR and the capability to detect the slowing down spectrum of beam injected ions has been demonstrated. The measured spectral shape agrees well with a slowing down model for the beam ions, but strong passive charge exchange emission was detected. Faster detectors and beam modulation is proposed for the TEXTOR diagnostic. Preliminary fast ion density profiles are obtained by subtracting the first frame after the NB switch off, showing a flattening of the core fast ion profile. Fast beam ion spectra have also been obtained on JET, but the signal to noise ratio is rather small due to the limited optical throughput of the diagnostic.

Fast helium CX spectra on ITER are modelled and the feasibility to extract the fast ion density profiles is discussed as a function of the optical throughput that could be achieved on the diagnostic. Prospects are limited. Only with coarse wavelength binning and very low contamination with impurity lines could a reasonable signal to noise ratio be obtained.

Curriculum Vitae

Ephrem Delabie was born on 24th of August 1983 in Kortrijk, Belgium. He studied Master of sciences and engineering in applied physics (Burgerlijk natuurkundig ingenieur) at University Ghent in Belgium. In 2006 he graduated with highest distinction. From September 2006 he started a PhD project at the FOM Institute for Plasma Physics Rijnhuizen at Nieuwegein, the Netherlands, of which the results are presented in this dissertation.

Acknowledgements

This phd thesis would not have been realized without the continuous support of many people.

Foremost, I want to thank my promotors, Niek Lopes Cardozo and Guido Van Oost, and my daily supervisor Roger Jaspers for making this thesis possible and to help me remaining focussed on my phd project.

I would like to express my special gratitude to Manfred von Hellermann, who first showed me the wonderful world of CX spectroscopy and who guided and encouraged me during my phd project.

Experimental physics on large devices is always a team effort. I would like to thank all members of the FOM Plasma Diagnostics Group, the TEXTOR team, the JET Core Spectroscopy Group and the Fusion Group at Eindhoven for the close and joyful collaboration.

Special thanks goes to several people who helped and shared their ideas on crucial moments during the last four years: Oleksandr Marchuk, Mathias Brix, Carine Giroud and Klaus-Dieter Zastrow.

Last but not least I want to thank my parents and my girlfriend for supporting me throughout, and my little daughter Syrah for urging me to finish this thesis.

